Titre: Title:	Carbon Nanotube Array Electrodes for Organic Thin Film Transistors
Auteur: Author:	Farzaneh Mahvash Mohammadi
Date:	2012
Type:	Mémoire ou thèse / Dissertation or Thesis
Référence: Citation:	Mahvash Mohammadi, F. (2012). Carbon Nanotube Array Electrodes for Organic Thin Film Transistors [Mémoire de maîtrise, École Polytechnique de Montréal]. PolyPublie. https://publications.polymtl.ca/791/

URL de PolyPublie: PolyPublie URL:	https://publications.polymtl.ca/791/
Directeurs de recherche: Advisors:	Clara Santato, & Fabio Cicoira
Programme: Program:	Génie physique

UNIVERSITÉ DE MONTRÉAL

CARBON NANOTUBE ARRAY ELECTRODES FOR ORGANIC THIN FILM TRANSISTORS

FARZANEH MAHVASH MOHAMMADI

DÉPARTEMENT DE GÉNIE PHYSIQUE
ÉCOLE POLYTECHNIQUE DE MONTRÉAL

MÉMOIRE PRÉSENTÉ EN VUE DE L'OBTENTION

DU DIPLÔME DE MAÎTRISE ÈS SCIENCES APPLIQUÉES
(GÉNIE PHYSIQUE)

AVRIL 2012

UNIVERSITÉ DE MONTRÉAL

ÉCOLE POLYTECHNIQUE DE MONTRÉAL

Ce mémoire intitulé

CARBON NANOTUBE ARRAY ELECTRODES FOR ORGANIC THIN FILM TRANSISTORS

présenté par : MAHVASH MOHAMMADI Farzaneh

en vue de l'obtention du diplôme de : Maîtrise ès sciences appliquées

a été dûment accepté par le jury d'examen constitué de :

M. MASUT Remo A., Ph. D., président

Mme SANTATO Clara, Ph. D., membre et directrice de recherche

M. CICOIRA Fabio, Ph. D., membre et codirecteur de recherche

M. MARTEL Richard, Ph. D., membre

DEDICATION

To my parents.

ACKNOWLEDGEMENTS

I would like to express my deepest gratitude to my advisor Prof. Clara Santato and co-advisor Prof. Fabio Cicoira, for the continuous support during my research, for their motivation, enthusiasm, and knowledge. Special thanks to Clara for accepting me in her group and introducing me into the research world. Sincere thanks to Fabio for his invaluable comments and trainings that made feasible the research herein described.

I would like to thank Prof. Richard Martel for giving me the opportunity to work in his laboratory.

I would like to express my gratitude to the members of my *jury d'examen*, Prof. Richard Martel and Prof. Remo A. Masut, not only for the time spent in reading this document, but also for their patience and their invaluable contribution to my scientific training. I benefited a lot from their constructive comments, questions, and suggestions.

I would also like to thank Joël Bouchard, Khalid Laaziri, Christophe Clément, Laurent Mouden, and Patricia Moraille at École Polytechnique de Montréal/Université de Montréal for their invaluable technical support.

Thanks to François Lapointe for assisting me in the deposition of the OTS layers.

Many thanks to Vangmayee Sharma, who helped me with the fabrication and characterization of the devices during the summer 2011.

RÉSUMÉ

Depuis environ une vingtaine d'années, les transistors organiques à base de couches minces (acronyme en anglais, OTFT) se sont développés de façon impressionnante, passant de l'échelle de recherche au laboratoire à l'échelle de commercialisation.

Les caractéristiques les plus intéressantes des OTFT sont leur compatibilité avec des substrats flexibles et leur méthode de fabrication, basée sur des techniques en solution.

Les performances des OTFT sont influencées très fortement par les caractéristiques de l'interface semiconducteur organique/électrode métallique.

L'interface semiconducteur organique/électrode métallique influence le processus d'injection de charge. En général, l'efficacité d'injection de charge dans les OTFT est limitée, parce que les niveaux électroniques du semiconducteur organique ne sont pas alignés avec le niveau de Fermi du métal de l'électrode.

Dans ce mémoire de maîtrise, nous avons focalisé l'attention sur le processus d'injection de charge dans les OTFT utilisant comme matériau d'électrode des rangées de nanotubes de carbone monoparois (acronyme en anglais, SWCNT).

Nous avons comparé les performances des OTFT basés sur des électrodes de type rangée de SWCNT avec les performances des OTFT utilisant des matériaux d'électrode plus conventionnels, tel que l'Au.

Les OTFTs ont été fabriqués sur une couche de SiO_2, obtenue par oxydation thermique d'une tranche de Si (100) fortement dopée (type n). La formation des rangées de SWCNT a été effectuée par la méthode de filtration sous vide des réseaux de SWCNT au-dessus de la surface de SiO_2. La géométrie concentrique d'électrode a été réalisée par photolithographie et par développement.

Nous avons observé des résultats très encourageants dans les cas de trois semiconducteurs organiques différents, tels que le poly-3 (hexyl) thiophène (P3HT), le dérivé du fullerène PCBM, et la ftalocyanine de tytanil (TiOPc).

Pour les TiOPc TFT, une meilleure efficacité d'injection, une mobilité de porteur de charge plus élevée, particulièrement dans le régime linéaire, et de plus hauts I_{ON}/I_{OFF} ont été observés dans les cas de SWCNT TFT comparé a leur référence, en l'occurrence les Au TFT.

L'efficacité d'injection des TiOPc TFT, faits avec des électrodes de type rangée de SWCNT, était deux fois plus grande que celle des TiOPc TFT faits avec des contacts d'Au. La conversion des TiOPc TFT initialement unipolaires en TFT ambipolaires suite au recuit thermique sous vide a été observée avec les électrodes de type rangée de SWCNT.

Les P3HT TFT utilisant les rangées d'électrodes de SWCNT ont fourni une mobilité plus élevée en comparaison avec les TFT de référence, faits avec des électrodes en Au. Le P3HT a été déposé sur SiO_2 et sur du SiO_2 traité avec des monocouches autoassemblées à partir du hexamethyldisilazane (HMDS) et de l'octadecylthrichlorosilane (OTS). Les P3HT TFT faits avec les rangées d'électrodes de SWCNT ont toujours montré une efficacité d'injection plus élevée que les P3HT TFT faits avec des électrodes d'Au.

Pour le mélange P3HT/PCBM, des caractéristiques de sortie quasi linéaires ont été observées dans les P3HT/PCBM TFT faits avec des électrodes de type rangée de SWCNT, pour les électrons et les trous, contrairement au comportement non linéaire détecté dans les P3HT/PCBM TFT utilisant des électrodes d'Au. L'efficacité d'injection d'électrons et de trous des P3HT/PCBM TFT faits avec les rangées d'électrodes de SWCNT était respectivement de trois ordres de grandeur et quatre fois plus élevée que celle des P3HT/PCBM TFT faits avec des électrodes d'Au.

Les résultats présentés dans ce mémoire confirment l'amélioration de l'efficacité d'injection dans les OTFT basé sur les rangées d'électrodes des SWCNT comparativement aux électrodes en Au, indépendamment du type de semiconducteur organique et du procédé de traitement utilisés.

ABSTRACT

Over the past two decades, organic thin film transistors (OTFTs) have developed from the research laboratory scale to the scale of commercially feasible technology.

The most attractive features of OTFTs are their low-cost manufacturing procedures and their compatibility with flexible substrates.

The characteristics of the organic semiconductor/metal electrode interface dramatically affect the performance of OTFTs. For instance, charge carrier injection efficiency can be limited by the offset between the HOMO and LUMO energy levels of the organic semiconductor and the Fermi level of the metal electrode, since this offset leads to the formation of an energy barrier for charge carrier injection.

This MSc work focuses on the use of single walled carbon nanotube (SWCNT) array electrodes, to improve the injection efficiency in OTFTs. A comparative approach has been adopted, based on the systematic comparison between SWCNT array electrode-based OTFTs with their, well investigated, Au electrode-based counterparts.

An improvement in the injection characteristics of OTFTs making use of SWCNT array electrodes has been previously demonstrated in OTFTs based on organic semiconductors such as (p-type) pentacene and copper phthalocyanine and (n-type) phenyl-C61-butyric acid methyl ester (PCBM). In these previous studies, it has been hypothesized that the improvement of the charge carrier injection characteristics is mainly due to the one dimensional (1D) structure of SWCNTs, which favors tunneling injection across the injection barrier.

To assess the general validity of this hypothesis, a large number of experiments need to be carried out with different organic semiconductors, belonging to different classes of materials (e.g., polymers and small molecules) and differently processed (e.g. solution processed and vacuum processed).

In this project, the performance of OTFTs making use of SWCNT array electrodes has been investigated for thin films of Titanyl-phthalocyanine (TiOPc), Poly-3 (hexylthiophene) (P3HT), and P3HT/PCBM blends. TiOPc belongs to metal phthalocyanines (MPcs), which, due to their low solubility in organic solvents, are typically deposited by vacuum-based techniques. P3HT is

a solution processable polythiophene. P3HT/PCBM blends, which are processed from solution, are benchmark materials in organic photovoltaics.

SWCNT array electrodes were patterned on a SiO_2 layer thermally grown on highly doped (n-type) Si (100) wafer. SWCNT array electrode fabrication started with the deposition of SWCNT networks by vacuum filtration. Subsequently, metallic (Ti) contacts were patterned on the SWCNT network by photholithography and lift-off. Finally, SWCNT array electrodes were obtained via a sonication in a stripper solution, which removes the SWCNTs not directly attached to the metal contacts and cuts the remaining SWCNTs to a length of a few hundred nm.

For TiOPc TFTs, SWCNT array electrodes led to improved injection efficiency, higher charge carrier mobility, especially in the linear regime, and higher I_{ON}/I_{OFF} compared with benchmark Au TiOPc TFTs. The injection efficiency of TiOPc TFTs with SWCNT array electrodes was two orders of magnitude higher than for TiOPc TFTs made with Au electrodes. Conversion of unipolar TiOPc TFTs to ambipolar TFTs upon thermal annealing under vacuum was also observed when using SWCNT array electrodes.

For P3HT TFTs, P3HT was deposited on bare SiO_2 and on SiO_2 treated with self assembled monolayers of hexamethyldisilazane (HMDS) and octadecylthrichlorosilane (OTS). In all cases, SWCNT array electrodes provided higher injection efficiency and mobility in comparison with benchmark Au OTFTs.

For P3HT/PCBM blends, quasi linear output characteristics in SWCNT P3HT/PCBM TFTs were observed for both electrons and holes, as opposed to the non linear behavior found in P3HT/PCBM TFTs making use of Au electrodes. Electron and hole injection efficiency of P3HT/PCBM TFTs made with SWCNT array electrodes could be as high as three orders of magnitude and four times higher than those of P3HT/PCBM TFTs made with Au electrodes, respectively.

The results presented in this MSc work are an important contribution to the demonstration of the possibility to improve the injection efficiency in OTFTs based on SWCNT array electrodes over Au electrodes, independently of the type of organic semiconductor and processing procedure employed.

TABLE OF CONTENTS

LIST OF TABLES

LIST OF FIGURES

LIST OF ACRONYMS AND ABREVIATIONS

μ	Charge carrier mobility
μ_e	Electron mobility
μ_h	Hole mobility
μ_{lin}	Charge carrier mobility in linear regime
μ_{sat}	Charge carrier mobility in saturation regime
1D	One dimensional
Alq_3	Tris (8-hydroxyquinoline) aluminum
Au HMDS P3HT TFT	P3HT TFT making use of HMDS SAMs treated SiO_2 and Au source and drain electrodes
Au HT TiOPc TFT	TiOPc TFT where TiOPc has been deposited at high temperature and making use of Au source and drain electrodes
Au OTS P3HT TFT	P3HT TFT making use of OTS SAMs treated SiO_2 and Au source and drain electrodes
Au P3HT TFT	P3HT TFT making use of Au source and drain electrodes
Au P3HT/PCBM (1:1) TFT	P3HT/PCBM blend TFT with weight ratio of (1:1) and Au source and drain electrodes
Au P3HT/PCBM (4:1) TFT	P3HT/PCBM blend TFT with weight ratio of (4:1) and Au source and drain electrodes
Au RT TiOPc TFT	TiOPc TFT where TiOPc has been deposited at room temperature and making use of Au source and drain electrodes
BCB	Benzocyclobutene
C_i	Capacitance per unit area of the gate dielectric

CNT	Carbon nanotube
CuPc	Copper phthalocyanine
CVD	Chemical vapor deposition
D	Drain
DCB	1, 2-dichlorobenzene
DNTT	Dinaphtho-[2, 3-b:2′,3′-f]thieno[3,2-b]thiophene
e	elementary charge
EA	Electron affinity of organic semiconductor
E_F (Au)	Fermi level of Au contacts
E_F (CNT)	Fermi level of SWCNT electrodes
E_F	Fermi level
E_G	Band-gap energy
E_V	Vacuum level
F8	poly (9,9 dicotylfluorene)
F8BT	Poly (9,9-di-n-octylfluorene-alt-benzothiadiazole)
FE-SEM	Field emission scanning electron microscopy
G	Gate
h	Planck constant
HMDS	Hexamethyldisilazane
HOMO	Highest occupied molecular orbital
I_D	Source-drain current
IMEM	Institute of the Materials for Electronics and Magnetism
I_{ON}/I_{OFF}	ON/OFF current ratio
IP	Ionization potential of organic semiconductor

IPA	Isopropyl alcohol
J_{BULK}	Bulk-limited current density
J_{FN}	Fowler-Nordheim current density
J_{INJ}	Injection-limited current density
J_{OHM}	Current density based on Ohm law
J_{RS}	Richardson-Schottky current density
k_B	Boltzmann constant
L	Inter-electrode distance
LEFET	Light-emitting field-effect transistor
LUMO	Lowest unoccupied molecular orbital
m*	Effective mass of the charge carrier in the semiconductor
MOSFET	Metal-oxide-semiconductor field effect transistor
MPc	Metal phthalocyanine
M_w	Molecular weight
MWCNT	Multi-walled carbon nanotube
N_0	Number of electrons per unit volume
NPD	N,N'-di(1-naphthyl)-N,N'-diphenyl-1,1'-diphenyl-1,4'-diamine
OFET	Organic field effect transistor
OLED	Organic light emitting diode
OLET	Organic light emitting transistor
OPV	Organic photovoltaic cell
OTFT	Organic thin film transistor
OTS	Octadecylthrichlorosilane
P3HT	Poly-3 (hexylthiophene)

PCBM	Phenyl-C61-butyric acid methyl ester
PF-9HK	Poly[(9,9-dioctyl-fluorenyl-2,7-diyl)-alt-co-(9-hexyl-3,6-carbazole)]
PMMA	Poly (methylmethacrylate)
R_c	Contact resistance
S	Source
SAM	Self assembled monolayer
SS	Subthreshold swing
SuMBE	Supersonic molecular beam epitaxy
SWCNT	Single-walled carbon nanotube
SWCNT HMDS P3HT TFT	P3HT TFT making use of HMDS SAMs treated SiO_2 and SWCNT array source and drain electrodes
SWCNT HT TiOPc TFT	TiOPc TFT where TiOPc has been deposited at high temperature and making use of SWCNT array source and drain electrodes
SWCNT OTS P3HT TFT	P3HT TFT making use of OTS SAMs treated SiO_2 and SWCNT array source and drain electrodes
SWCNT P3HT TFT	P3HT TFT making use of SWCNT array source and drain electrodes
SWCNT P3HT/PCBM (1:1) TFT	P3HT/PCBM blend TFT with weight ratio of (1:1) and SWCNT array source and drain electrodes
SWCNT P3HT/PCBM (4:1) TFT	P3HT/PCBM blend TFT with weight ratio of (4:1) and SWCNT array source and drain electrodes
SWCNT RT TiOPc TFT	TiOPc TFT where TiOPc has been deposited at room temperature and making use of SWCNT array source and drain electrodes
T	Temperature

TFB	Poly(9,9-dioctyl-fluorene-co-N-(4-butylphenyl)-diphenylamine)
TiOPc	Titanyl-phthalocyanine
TOF	Time of flight
UHV	Ultra-high-vacuum
V	Voltage applied to the semiconductor
V_D	Drain-Source voltage
V_G	Gate-source voltage
V_{ON}	Onset voltage
V_{TH}	Threshold voltage
W	Electrode width
Φ_{Au}	Workfunction of Au contact
Φ_B	Injection barrier
Φ_{CNT}	Workfunction of SWCNT
Φ_m	Metal workfunction

LIST OF APPENDICES

CHAPTER 1 INTRODUCTION

1.1 Overview

Organic electronics is the branch of electronics that deals with carbon-based, π-conjugated semiconductors, including polymers and small molecules. Applications related to organic electronics can be classified into three major areas, namely organic light emitting diodes (OLEDs), organic thin film transistors (OTFTs), and organic photovoltaic cells (OPVs) [1]. An important emerging field is organic bioelectronics.

The first OTFT was reported in 1988 by Tsumura *et al.* [2]. In 1987, Tang and Van Slyke (Eastman Kodak) fabricated the first OLED making use of thin films of small organic molecules [3]. Research efforts in the field of organic electroluminescence led to the fabrication of OLEDs based on polymers in 1990 [4]. OLEDs have already entered the market [5], [6]. In the area of OPVs, early research dates back to the 1980s [7]. Nowadays the power conversion efficiency of OPVs is about 10 % [8]. Figure 1.1 shows the increasing number of publications per year in the various fields of organic electronics (OLEDs, OTFTs, OPVs and bioelectronics) from the early nineties to 2008.

The success of organic electronics stems from: (i) tunability of electronic properties through chemical synthesis [9], (ii) low-cost manufacturing procedures such as solution processing, (iii) compatibility with flexible and inexpensive substrates such as thin plastic foils [10]. These properties open up the opportunity of creating flexible electronic circuits and consequently the development of foldable or rollable displays as well as conformable sensors [11], [12].

A number of challenges are still open in the field of organic electronics. As an example, the charge carrier mobility for organic semiconductors is still low compared to the mobility of their inorganic counterparts and the environmental stability of organic semiconductors, although significantly improved over the last years, is limited [13].

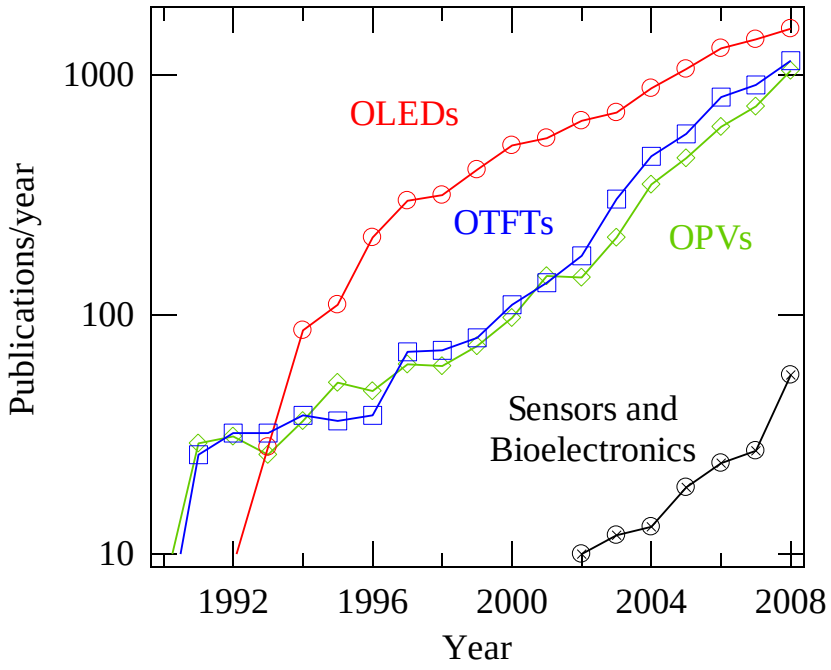

Figure 1.1: Number of publications on OLEDs, OTFTs, OPVs and organic bioelectronics per year from the early nineties to 2008 (log scale).

1.2 Organic semiconductors

Organic semiconducting molecules can be generally classified into small molecules (oligomers) (molecular weight < 1000 g/mol) and polymers (molecular weight > 1000 g/mol) [14].

Organic semiconductors are made of carbon-based small molecules and polymers with *conjugated* structures, where alternating single and double bonds are present. The double bonds consist of σ-bonds and π-bonds. C atoms of organic semiconductors are sp^2- hybridized and consequently each atom has 3 sp^2 orbitals and one p_z orbital (Figure 1.2). The σ-bonds are formed by the interaction of sp^2 orbitals of two C atoms whereas the π-bonds are formed by the interaction of p_z orbitals.

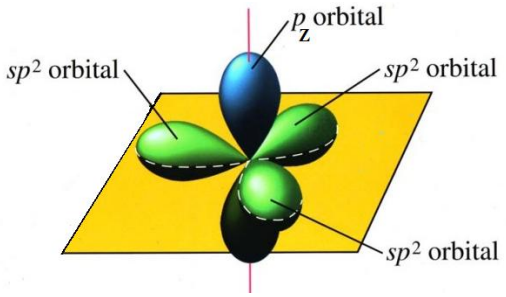

Figure 1.2: Representation of sp^2-hybridized C atom.

In the solid state, organic semiconducting molecules are kept together by weak Van der Waals intermolecular interactions (10^{-3}-10^{-2} eV) [15], [16].

There are analogies between the electronic structure of organic and inorganic semiconductors. The highest occupied molecular orbital (HOMO) and the lowest unoccupied molecular orbital (LUMO) energy levels of organic semiconductors can be considered as the valence band edge and the conduction band edge of the semiconductor, respectively [17]. The energy difference between the HOMO and the LUMO is the band gap energy (E_G) (Figure 1.3). Typical band gaps for organic semiconductors are between 1.5 and 3 eV.

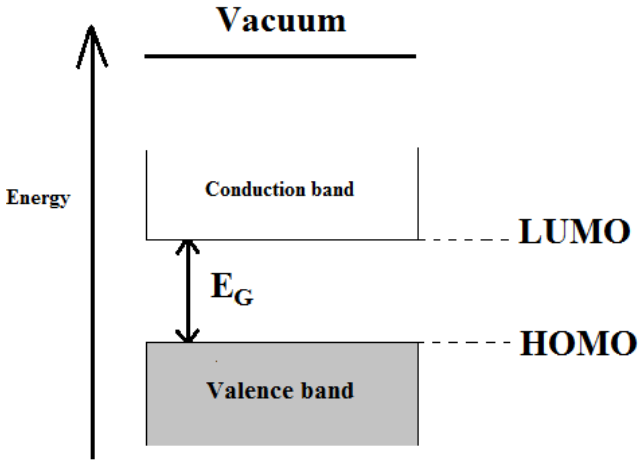

Figure 1.3: Scheme of the energy band diagram for organic semiconductors.

The *conjugation*, typical of organic semiconductors, causes the delocalization of the π electron of the sp^2-hybridized C atoms. In turn, the delocalization enables charge carrier transport within the organic semiconductor.

There are two main possible charge transport mechanisms in organic semiconductors, namely hopping and band-like [13]. In polycrystalline organic semiconductors, with a few exceptions, the mechanism of transport is based on thermally activated hopping of the charge carriers through a distribution of localized states. In these organic semiconductors charge carrier mobility typically increases with increasing temperature. On the other hand, in highly ordered molecular crystals (single crystals), transport is described by band-like mechanism. The charge carrier mobility of single crystals typically decreases with increasing temperature [15].

In principle, organic semiconductors can support either positive (holes) or negative (electrons) charge carriers as the majority carriers [16]. In some cases, transport of both charge carriers can be observed. In this latter case the organic semiconductors are known as ambipolar.

The majority of organic electronic devices are based on thin films. To obtain thin films, small molecules can be processed both via solution and vacuum-based deposition techniques whereas polymers can be exclusively processed from solution [18].

Film morphology and structure, determined by the film nucleation and growth, dramatically affect the film functional properties, in turn affecting device performance [19].

For vacuum-based techniques, a number of deposition parameters can be controlled, such as the rate of deposition and the substrate temperature. For solution-based techniques, the key parameters for the film formation process are the solvent volatility and the concentration of the organic semiconductor in solution. In addition, the wettability of the substrate used for film growth are crucial in establishing a certain structure and morphology [20].

In this project, we studied the organic semiconductors Titanyl-phthalocyanine (TiOPc), Poly-3 (hexylthiophene) (P3HT), and P3HT/ phenyl-C61-butyric acid methyl ester (PCBM) blends. The chemical structure of these organic semiconductors is shown in Figure 1.4.

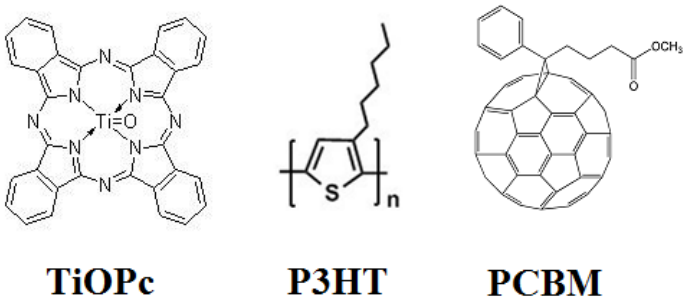

Figure 1.4: Chemical structures of TiOPc, P3HT, and PCBM.

TiOPc is a small molecule belonging to the metal phthalocyanine (MPc) family. Because of their volatility and high thermal stability (up to 400 ˚C [21]), metal phthalocyanines can be deposited by thermal evaporation [22]. The HOMO and LUMO level of TiOPc are about -5.7 and -3.9 eV (with respect to the vacuum level) respectively [23].

Most TiOPc OTFTs exhibit p-type behaviour. However, an n-type behaviour was reported under ultra high vacuum [24]. Li *et al.* achieved the highest μ_h of 3.31 $cm^2/V{\cdot}s$ in TiOPc OTFTs using SiO_2 substrates treated with a self assembled monolayer of octadecylthrichlorosilane (OTS) [25].

P3HT, which belongs to the family of polythiophenes, is a p-type solution-processable polymeric semiconductor soluble in a number of common organic solvents [26–29]. The HOMO and LUMO values of P3HT reported in the literature are around -4.9 and -3 eV (with respect to vacuum level), respectively [30], [31]. For OTFTs based on this polymer, the highest reported hole mobility (μ_h) is about 0.1 $cm^2/V{\cdot}s$ [26], [32].

The degree of P3HT regioregularity, the molecular weight (M_w), and the deposition conditions significantly affect the performance of P3HT OTFTs. Sirringhaus *et al*. found that upon deposition of P3HT on a flat substrate, ordered lamellar domains (fine sheets of material) were formed. The orientation of these domains is related to the degree of regioregularity, the molecular weight, and the deposition conditions [32].

PCBM, a fullerene derivative, is a solution processable n-type small molecule [33]. The LUMO level of PCBM is located at about -4.3 eV [34] and the HOMO level is at about -6 eV [35] (with respect to the vacuum level).

1.3 Organic thin film transistors (OTFTs)

An OTFT is made of a thin film of organic semiconductor in contact with source (S) and drain (D) electrodes separated from the gate (G) electrode by a gate dielectric layer [36] (Figure 1.5). The region of the organic semiconductor delimited by the S and D electrodes is the transistor channel. The characteristic dimensions of a transistor are the inter-electrode distance (L) and the electrode width (W).

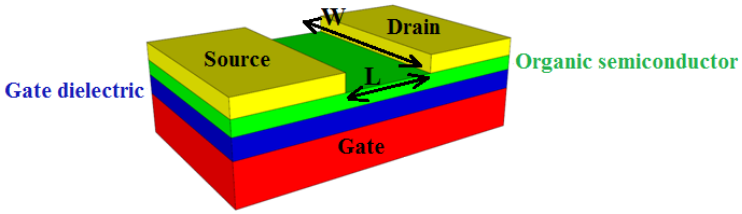

Figure 1.5: Schematic device structure of an OTFT. L and W are the length (L) and width (W) of the transistor channel.

The working principle of an OTFT can be described as follows: upon application of a gate voltage (V_G), a thin sheet of mobile charge carriers is formed in the organic semiconductor. After injection from the S and D electrodes, the charge carriers move within the transistor channel as a function of the applied drain-source voltage (V_D). The source-drain current (I_D) is modulated by V_G [13].

There are different possible architectures for OTFTs. The G electrode can be positioned either on top (top-gate) of the organic semiconductor or underneath it (bottom-gate). For each of these two cases, there are two different configurations of the S and D electrodes (bottom and top-contacts). Hence, four distinct OTFT architectures are possible, as illustrated in Figure 1.6. It should be noted that the specific architecture of electrodes affects the performance of OTFTs [13]. For example, different morphologies of the top and bottom surfaces of the organic semiconductor thin films [37] and the presence of trap states during electrode deposition on organic semiconductors for top-contact OTFTs [38], [39] can change the performance.

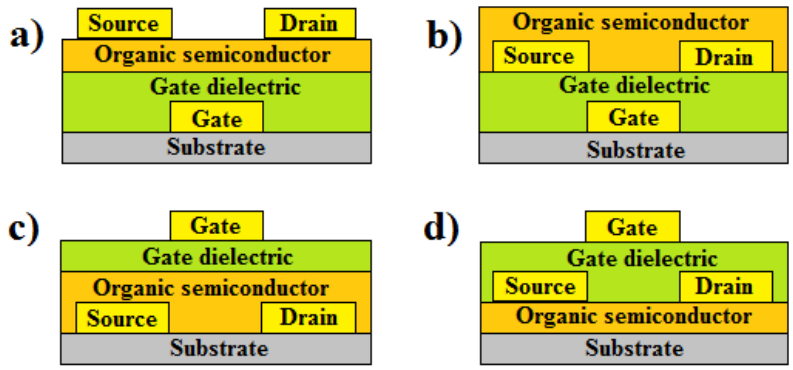

Figure 1.6: Four different OTFT architectures. (a) Bottom-gate top-contact OTFT (b) Bottom-gate bottom-contact OTFT (c) Top-gate bottom-contact OTFT (d) Top-gate top-contact OTFT.

The main figures of merit of an OTFT are the charge carrier mobility (μ), the ON/OFF current ratio (I_{ON}/I_{OFF}), the threshold voltage (V_{TH}), the onset voltage (V_{ON}) and the subthreshold swing (SS) [16]. The mobility [$cm^2/V{\cdot}s$] is the velocity of the charge carriers per unit of applied electric field. I_{ON}/I_{OFF} designates the switching performance of the device. It is defined as the ratio of source-drain current (I_D) in the ON and OFF states. The ON and OFF states are usually taken where I_D attains its maximum and minimum values, respectively, on the I_D versus V_G plot (typically reported on a logarithmic scale), recorded at a certain V_D. V_{ON} is the V_G at which I_D abruptly increases.V_{TH} indicates the minimum V_G required to attain a quadratic dependence of I_D on V_G (in the saturation regime, where the channel is *pinched off*) or the minimum V_G required to attain a linear dependence of I_D on V_G (in the linear regime, where the I_D increases linearly with V_D). The SS is defined as $dV_G/d\log_{10}I_D$ in the subthreshold region, where V_G is lower than V_{TH}.

The intense research activity carried out in the last twenty years on organic semiconductor synthesis and OTFT engineering has led to significant improvements of the performance of OTFTs [36], [40].

The performance of OTFTs is affected by a complex interplay of factors, among which are the morphology and structure of the organic film [19] and the quality of the dielectric/organic film [36] and metal electrode/organic film interfaces [41].

The metal electrode/organic semiconductor interface plays a crucial role in establishing the performance of OTFTs, since charge carriers need to be injected from S and D electrodes into the

organic semiconductor before being transported within the transistor channel [42]. The presence of charge injection barriers at the metal electrode/organic semiconductor interface can lead to poor injection efficiency of OTFTs. In this context, the main purpose of this MSc work is to give a contribution to improve the efficiency of the injection of electrons and holes in OTFTs.

1.4 Charge carrier injection in OTFTs

In this section we briefly recall a few fundamental concepts about charge injection in OTFTs. The metal workfunction (Φ_m) is defined as the energy required to remove an electron from the Fermi level of the metal to the vacuum. The ionization potential (IP) and electron affinity (EA) of an organic semiconductor are respectively the energy required to remove an electron from the HOMO level of the molecule to the vacuum, and the energy required to add an electron to the molecule (in the LUMO level) [43].

Because of the offset between the LUMO and HOMO levels of the organic semiconductor and the Fermi level of the metal, an energy barrier for charge carrier injection, the Schottky barrier, is present at the metal/organic interface [44],[45],[46]. It is possible to estimate the electron and hole injection barriers from the difference between the LUMO and HOMO levels of the organic semiconductor and the Fermi level of the metal, respectively. Therefore, the hole injection barrier ($\Phi_{B,h}$) is defined as:

$$\Phi_{B,h} = E_F(M) - E_{HOMO}(S) = IP - \Phi_m \qquad \text{Equation 1-1}$$

and the electron injection barrier ($\Phi_{B,e}$) is defined as:

$$\Phi_{B,e} = E_F(M) - E_{LUMO}(S) = \Phi_m - EA \qquad \text{Equation 1-2}$$

There are different charge carrier injection mechanisms possible for OTFTs (Figure 1.7) [42]. We will briefly illustrate them in what follows.

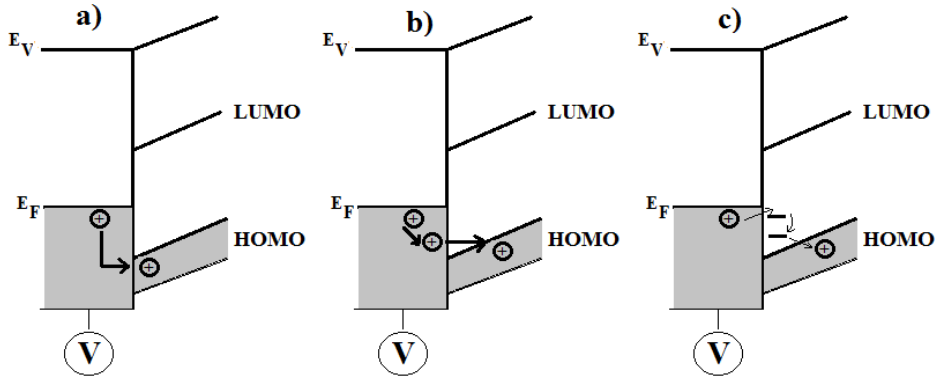

Figure 1.7: Different charge carrier injection mechanisms at a biased metal/organic semiconductor interface, in OTFTs. E_V: Vacuum level, E_F: Fermi level of the metal: (a) Thermionic emission, (b) Field emission (tunneling), (c) Defect-assisted injection.

In Richardson-Schottky injection or thermionic emission, the charge carriers surmount the injection barriers upon application of an electrical bias if the thermal energy of charge carriers is greater than the charge carrier injection barrier. This model is valid at high temperatures or low injection barriers. The injected current density can be described as [47]:

$$J_{RS} = \frac{4\pi e k_B^2 m^*}{h^3} T^2 \exp\left(-\frac{e\Phi_B}{k_B T}\right)\left[\exp\left(\frac{eV}{k_B T}\right) - 1\right} \qquad \text{Equation 1-3}$$

where e is the elementary charge, m^* the effective mass of the charge carrier in the semiconductor, V the voltage applied to the semiconductor, k_B the Boltzmann constant, h the Planck constant, T the temperature, and Φ_B is the charge carrier injection barrier in the absence of electric field.

In Fowler-Nordheim tunneling (field emission) mechanism, charge carriers tunnel through a thin energy barrier. This mechanism is found in the case of high injection barriers and it is enabled by high electric fields. The injected current density can be described as [48]:

$$J_{FN} = \frac{e^3}{8\pi h \Phi_B} E^2 \exp\left(-\frac{8\pi\sqrt{2m^*\Phi_B^3}}{3heE}\right) \qquad \text{Equation 1-4}$$

where E is the electric field at the interface (the meaning of the other symbols is the same as for the previous equation).

In the defect-assisted injection, charge carriers *circumvent* the barrier by hopping through midgap states.

In general, OTFTs show low injection efficiency [49], [50] due to the presence of Schottky barriers [36]. This is different from what is observed in Si MOSFET technology, where implantation of atoms forming n-regions and p-regions at the contacts prevents the formation of injection barriers. The low injection efficiency in OTFTs leads to a sigmoidal shape of the current-voltage output TFT curves. On the other hand, the linear behavior of current-voltage output TFT curves indicates an ohmic behavior of the contacts, and consequently high injection efficiency. Injection efficiency can be defined as the ratio of the injection-limited current density (J_{INJ}) versus the bulk-limited current density (J_{BULK}) [41].

If we assume that we have a trap-free semiconductor and we neglect the diffusion of the charge carriers, at low voltages the current density flowing in the transistor channel is described by the Ohm law such that [41].

$$J_{OHM} = J_{BULK} = eN_0\mu\frac{V}{L} \qquad \text{Equation 1-5}$$

where N_0 is the number of electrons per unit volume, V is the applied voltage, μ is the charge carrier mobility, and L is the length of transistor channel.

An ohmic contact is defined as a contact where the injection efficiency (J_{INJ}/J_{BULK}) is one. Only if the Fermi level of the metal is aligned to the LUMO or HOMO levels of organic semiconductor, an ohmic contact can be expected [41], [51], [52].

Other factors including the morphology and structure of the semiconductor at the metal/organic semiconductor interface can also dramatically affect the injection process. Interfacial charge carrier traps, dipoles (charge rearrangements upon interface formation) and chemical impurities, affecting the interfacial electronic structure, can also affect charge injection [52], [51]. Moreover, the presence of surface states (electronic states at the surface of materials where dangling bonds can be present) at the metal/organic semiconductor interface can produce a Fermi level pinning (a phenomenon where surface states stabilize the Fermi level of the semiconductor) making the estimation of Schottky barrier difficult [43].

In this MSc project we assume an ideal interface without traps and dipoles, with unpinned Fermi level, such that the Schottky barrier can be estimated by the difference between metal Fermi level and HOMO or LUMO level of organic semiconductors.

Different approaches have been investigated to improve charge carrier injection including (i) use of low workfunction metals for electron injection [53], (ii) doping the organic semiconductor in proximity of the metal contacts [54], (iii) blending salts to organic semiconductors [41], (iv) using self assembled monolayer (SAM) to modify the metal surface, prior to organic semiconductor deposition [55]. Each one of these approaches presents major limitations. Low workfunction metals suitable for e^- injection, such as Ca, are highly reactive in ambient conditions. Doping of organic semiconductors employed in OLEDs actually improved their performance but has to be selectively carried out in the vicinity of the contacts [54].

Blending of salts with organic semiconducting polymers has been investigated since almost twenty years in light emitting electrochemical cells, but can only be applied in solution processed organic semiconductors [56]. Moreover, this solution is not a viable one for OTFTs since it leads to a dramatic increase of the device OFF current and switch on times.

Modification of Au workfunction with SAMs of polar thiols such as perfluorodecanethiol on the metal surfaces prior to deposition of the organic semiconductor also leads to improved charge carrier injection [55]. However this approach is limited to Au electrode surfaces, where thiols can self-assemble [57–61].

There is then a need to explore novel approaches of general validity to improve charge carrier injection efficiency in organic semiconductor thin films of interest for OTFT applications. In this context, we propose in this MSc work the use of SWCNT array electrodes.

1.5 Charge carrier injection from CNT electrodes to organic semiconductor thin films

Carbon nanotubes (CNTs) are being investigated by several research groups as electrode materials in organic electronic devices to improve the device performance [62–71].

Before presenting a literature review on CNTs used as electrode materials in organic electronics, we would like to briefly recall in this section a few fundamental properties of CNTs.

CNTs can be either single-walled (SWCNTs) or multi-walled (MWCNTs). A graphene sheet rolled up into a cylinder can form a SWCNT. MWCNTs consist of a series of coaxial SWCNTs. The circumference of a SWCNT is defined by means of the chiral vector $\vec{C} = n\vec{a} + m\vec{b}$ where $\vec{a}$ and $\vec{b}$ are the unit vectors of the graphene sheet and n and m, the integer coefficients of the linear combination, are the chirality indices (Figure 1.8). A particular SWCNT is defined by n and m, usually denoted by (n, m) [72]. The electronic properties of CNTs depend on (n, m): if n-m=3j, where j is an integer, CNTs are metallic; otherwise, they are semiconducting [73].

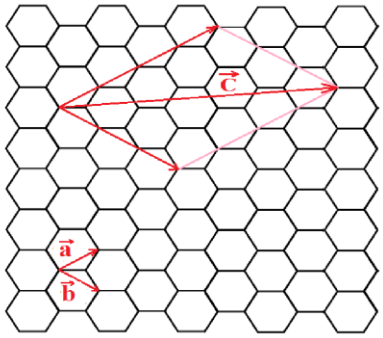

Figure 1.8: A graphene sheet with unit vectors indicated by $\vec{a}$ and $\vec{b}$. The vector $\vec{C} = n\vec{a} + m\vec{b}$ defines the circumference of the CNT.

CNTs can be considered as quasi one-dimensional (1D) nanostructures due to the high aspect ratio of length-to-diameter (typically they are several μm-long and have a diameter of 1-2 nm [74]).

CNTs have remarkable properties such as high electrical conductivity (about 10^6-10^7 S/m [75]), high thermal conductivity (up to 3500 W/m·K at room temperature [76]), chemical stability, and ease of processing [62], [77], [63].

We would like to mention some relevant examples of different applications of CNT electrodes in organic electronics in what follows.

As an example of CNT use in the field of OPV, we mention the work of Miller *et al.*, who demonstrated that MWCNTs uniformly distributed within the donor layer of bi-layer heterojunction OPV cells can behave as efficient hole-extracting electrodes. The OPV cells had fill factors of about 50% for MWCNTs concentrations of 1 wt %, to be compared to a value of 25% in absence of MWCNTs. [78]

OLEDs making use of CNTs have also been investigated. High performance OLEDs using transparent and conductive SWCNT sheets as anodes were achieved by Aguirre *et al.* [79]. They achieved a brightness of, 2800 cd/m^2 a luminance efficiency, of 1.4 cd/A, a value to be compared with 1.9 cd/A observed using as the anode a conventional indium tin oxide (ITO) electrode. The comparable efficiency together with the flexibility of CNTs, to be compared to brittle ITO, make CNT films potential candidates to replace ITO electrodes in OLEDs.

Solution processed sensitive photodetectors, active in the visible portion of the electromagnetic spectrum, operating at room temperature, were fabricated using copper phthalocyanine (CuPc) in the form of Langmuir Blodgett monolayers as the photosensitive material and SWCNTs as the point contacts [71]. The fabrication of the point contacts was carried out by the initial fabrication of SWCNT transistor structures followed by the definition of a 5 nm gap within the tube by e-beam lithography and oxygen plasma etching [80]. The mobility in linear regime for the CuPc trasnsistor/photodetector was 0.4 cm^2/V·s which is the highest among those obtained from organic ultrathin film transistors. I_{ON}/I_{OFF} of 10^4 and SS of about 450 mV/ decade were calculated. These photodetectors exhibited responsivities greater than 10^8A/W.

A few studies have addressed the use of CNTs as electrodes in OTFTs which are presented here.

Field-effect operation in organic transistors based on pentacene nanocrystals and metallic MWCNT S/D electrodes was reported [81]. The fabrication of the electrodes was such that initially MWCNTs, with diameter of about 10 nm and length of 5 μm, were synthesized by the arc-discharging method. Afterwards, two pads of Pt (10nm)/Au (40 nm) were defined on top of one MWCNT using electron-beam lithography, at a distance of 4 μm. The application of a high current (about 200 μA) at room temperature, in air, opened a gap shorter than 50 nm on the MWCNT [82]. Afterwards, pentacene was selectively grown on the electrode gap by vacuum sublimation through a poly (methylmethacrylate) (PMMA) 10 μm^2 window, defined by electron beam lithography.

It was also shown in [83] that metallic SWCNTs can be used as quasi-1D electrodes to build organic field effect transistors (OFETs) with molecular-scale width (~2 nm) and channel length (down to 1-3 nm). Pentacene (vapor deposited) and P3HT (solution processed) were used as the organic semiconductors. For comparison with SWCNT-contacted devices, short channel OFETs with conventional metal electrodes were also fabricated (Pd, with Ti adhesion layer). At $V_D \approx 0.3$ V, the SWCNT-contacted FET exhibited a SS of about 400 mV/decade, while SS was about 4 V/decade for the metal-contacted FET.

Cao *et al*. fabricated mechanically flexible OTFTs based on ultrathin films of pentacene and transparent electrodes of SWCNTs networks, formed by transfer printing of pristine CNTs grown by chemical vapor deposition (CVD) [84]. The SWCNT networks were used for all the three electrodes in the OTFTs (G, S, and D electrodes). Mobility values as high as 0.5 $cm^2/V{\cdot}s$ and I_{ON}/I_{OFF} larger than 10^5 were observed. Cao *et al.* also fabricated analogous devices using Au electrodes. The contact resistance (R_c) was significantly lower in SWCNT devices ($R_c \sim 2{\times}10^5$ $\Omega{\cdot}cm$) compared to Au devices ($R_c \sim 14{\times}10^5$ $\Omega{\cdot}cm$). The behavior of the SWCNT electrodes was ascribed to field focusing due to the high aspect ratio of the SWCNTs.

Decreasing of contact resistance in OTFTs based on pentacene by means of MWCNT electrodes was also reported in [85]. In this study, MWCNTs (with two different lengths: 400 nm and 1 μm) were deposited by thermal CVD, directly on the Fe/Ti S/D patterned electrodes playing a catalytic action towards the growth of the CNTs. The Fe/Ti catalytic layer was deposited through electron beam thermal evaporation and patterned using photolithography and lift-off. The lowest value of $R_c \sim 3{\times}10^4$ $\Omega{\cdot}cm$ were measured, together with μ of 0.14 $cm^2/V{\cdot}s$ and $I_{ON}/I_{OFF} > 10^6$.

Liu *et al.* proposed a new architecture of application for CNTs [86]. They fabricated vertical OTFTs and vertical organic light emitting transistors (OLETs) using a network of SWCNTs as S electrode. Their architecture paved the way for the use of low mobility organic semiconductors and provided sub-μm channel lengths without need of high-resolution patterning. The fabrication of vertical OTFTs starts with transfer of SWCNT networks on a 200 nm thermal SiO_2 heavily p-doped silicon substrate, which provided the bottom G. Afterwards, the active layer poly[(9,9-dioctyl-fluorenyl-2,7-diyl)-alt-co-(9-hexyl-3,6-carbazole)] (PF-9HK) or N,N'-di(1-naphthyl)-N,N'-diphenyl-1,1'-diphenyl-1,4'-diamine (NPD) was deposited over the entire substrate on top

of the SWCNT network. Finally, 20 nm of Au thermally evaporated onto the active layer as D electrode.

Vertical OLETs reproduced by the same group, the gate electrode is indium tin oxide on a transparent substrate with a 160 nm atomic-layer-deposited aluminum-titanium oxide gate dielectric on which the SWCNTs were deposited. PF-9HK as the gated, hole-injecting layer, NPD as the hole transport layer, and tris(8-hydroxyquinoline) aluminum (Alq_3) as the photoactive layer were deposited over the SWCNT network. The D electrode on top of the active layers was thermally evaporated LiF/Al. At a V_D of -30 V, the luminance (green color) was 540 cd/m^2, at a current density of 17.3 mA/cm^2, for a reasonable efficiency of 3.1 cd/A, which is comparable to typical indium tin oxide anode, NPD/Alq_3-based devices.

Southard *et al.* demonstrated pentacene and poly-3-hexylthiophene (P3HT) TFTs making use of transparent films of commercially-available SWCNTs produced by airbrushing from aqueous solutions as the S/D electrodes [87]. They obtained the μ of 0.093 cm^2/V·s and $I_{ON}/I_{OFF} > 10^6$ (V_D = -60 V, -60 V $\leq V_G \leq$ 60 V) for pentacene TFTs and the μ of 0.014 cm^2/V·s and $I_{ON}/I_{OFF} > 10^5$ (V_D = -60 V, -60 V $\leq V_G \leq$ 50 V) for P3HT TFTs.

OTFTs using SWCNTs arrays as the S/D electrodes, kept on the substrates by Ti pads, and pentacene as the semiconductor were reported in [70]. In the same study, OTFTs analogues, making use of Au electrodes and Ti pads, were also prepared. OTFTs based on CNT array electrodes showed output characteristics indicating efficient injection. Pentacene showed an effective linear mobility of 0.14, 0.09, and 0.001 cm^2/V·s for CNTs array-, Au-, and Ti-based electrode devices, respectively.

McCarthy *et al.* fabricated a vertical OFET using a network of SWCNTs as the S electrode and dinaphtho-[2,3-b:2′,3′-f]thieno[3,2-b]thiophene (DNTT) as the organic semiconductor [88]. DNTT was deposited by vacuum sublimation on a CNT network spread on the gate dielectric. Finally DNTT was covered by an Au top D electrode. The figures of merit for the device were $I_{ON}/I_{OFF} > 10^5$ for a V_G range of 4 V, with a current density output exceeding 50 mA/cm^2. In another study [89], the same group applied the same architecture using pentacene as the organic semiconductor. I_{ON}/I_{OFF} of around 10^5 was obtained while the transistor current density was about 50 mA/cm^2.

Liu *et al.*, used the same architecture of vertical FETs based on SWCNT networks as the S electrode to build high-performance non-volatile memory elements [90]. The SWCNT random network S electrode facilitates charge injection into the charge storage layer, which is a thin film of crosslinking polymer layer, benzocyclobutene (BCB), on top of the gate dielectric (a 200 nm thick thermal SiO_2). After deposition of BCB, poly (9,9-dioctyl-fluorene-co-N-(4-butylphenyl)-diphenylamine) (TFB) was used as the charge transport material. Au top D electrode was evaporated onto the active layer.

The same research group, recently demonstrated a vertical OLET using a SWCNT network S electrode that operates at low voltage (V_{ON} ~ -2.5 V) with low parasitic power dissipation (6.2 %) and the near-full aperture emission (~98%) in the three primary colors (red, blue, green) [91]. The vertical OLET can be described as an OLED inserted into a vertical OTFT making use of CNT S electrode. Transparent indium tin oxide glass was used as a bottom G electrode on top of which the gate dielectric Al_2O_3 and a thin hydrophobic layer of BCB were sequentially deposited. A diluted network of SWCNTs, optically and electrically transparent, was spread over the gate dielectric (made hydrophobic by the BCB layer) and served as the S electrode. The organic semiconductor DNTT was vacuum sublimed over the SWCNT network. Prior to deposition of the D electrode, the insertion of the OLED layers was done (on top of organic semiconductor). For emission of different colors, different emitter layers were used based on different iridium complexes.

Gwinner *et al.* demonstrated that the presence of small amounts of semiconducting SWCNTs dispersed in poly(9,9-di-n-octylfluorene-alt-benzothiadiazole) (F8BT) and poly(9,9 dicotylfluorene) (F8) increases both hole and electron injection in top gate/bottom contact ambipolar light-emitting field-effect transistors (LEFETs) based on these conjugated polymers [92]. The V_{TH} and V_{ON} for both holes and electrons were decreased with respect to devices without CNTs. Ambipolar currents and maximum light emission intensities were 1-2 orders of magnitude higher than in devices without CNTs.

In recent studies, the performance of CNT array electrodes in PCBM and CuPc TFTs revealed their superiority compared to conventional Au electrodes [93], [94]. Specifically, the linear behavior in the I_D-V_D characteristics of PCBM OTFTs based on CNT array electrodes at low V_D indicated good injection efficiency. Indeed, upon application of the same voltage, sublinear I_D-V_D

behavior was obtained in analogous PCBM OTFTs based on Au electrodes, indicating that charge injection was limited by the presence of an injection barrier. Higher μ for PCBM OTFTs based on CNT electrodes than those using Au electrodes was also observed (at V_G = 20 V, μ ~2×10^{-2} $cm^2/V\cdot s$ for CNT OTFTs and μ ~1×10^{-3} $cm^2/V\cdot s$ for Au OTFTs). The difference between extracted mobility in the saturation regime between CNT devices vs Au devices decreased with increasing V_G (at V_G = 40 V, μ ~1×10^{-2} $cm^2/V\cdot s$ for CNT OTFTs and μ ~ 6×10^{-3} $cm^2/V\cdot s$ for Au OTFTs). The linear mobility (at V_D = 2 V) of CNT OTFTs was about two orders of magnitude larger than linear mobility of Au OTFTs (μ ~1×10^{-2} $cm^2/V\cdot s$ for CNT OTFTs and μ ~1×10^{-4} $cm^2/V\cdot s$ for Au OTFTs at room temperature).

These results demonstrated a higher mobility of CNT OTFTs at low bias as well as a lower V_{TH} and a higher I_{ON}/I_{OFF} (at V_G= 20 V, V_{TH} ~ 6 V, I_{ON}/I_{OFF} = 10^6 for CNT OTFTs; V_{TH} ~ 10 V, I_{ON}/I_{OFF} = 10^5 for Au OTFTs). After vacuum annealing at about 130 ˚C for 16 h, PCBM OTFT with CNT electrodes showed an ambipolar behavior, with ohmic injection of electrons and holes. The mechanism behind this change from unipolar to ambipolar is still under investigation. A similar conversion of unipolar to ambipolar transport had been previously shown in transistors using CNT as semiconductors where was attributed to the desorption of O_2 and H_2O molecules from the surface of the SiO_2 [95].

In OTFTs with CNT array electrodes based on CuPc thin films (deposited by supersonic molecular beam epitaxy, SuMBE), an ohmic hole injection was obtained [94]. In CNT devices, high μ of 1.2×10^{-2} $cm^2/V\cdot s$ at V_G= -20 V and I_{ON}/I_{OFF} of about 10^6 at V_D= -1 V and V_G= -10 V were achieved while a μ of 5×10^{-3} $cm^2/V\cdot s$ and I_{ON}/I_{OFF} of 10^3 were obtained for similar devices using Au electrodes in the same conditions. Conversion of p-type to ambipolar OTFTs by vacuum annealing was also achieved.

High performance short channel pentacene OTFTs using aligned arrays SWCNT S/D electrodes was demonstrated by Sarker and co-workers. The mobility of 0.65 $cm^2/V\cdot s$ and I_{ON}/I_{OFF} of 1.7×10^6 were achieved, higher than those observed in other short channel devices [96].

To deeply understand the charge injection mechanism from CNT electrodes to organic semiconductors, a detailed knowledge of the CNT/organic semiconductor interface is required. However this interface has not been carefully characterized yet. The hypothesis to explain the

improvement of charge carrier injection in OTFTs using CNT electrodes is that, because of 1D structure of CNTs, the electric field at CNT/organic semiconductor interface is considerably enhanced in comparison with the interface between a metal electrode/organic semiconductor. This enhancement can originate sharper band bending in the CNTs/organic semiconductor interface and consequently improve charge injection.

It is worth noting that in transistors using semiconducting CNTs as semiconductor and Ti electrodes, the enhancement of electric field at the CNT/metal interface due to 1D structure was clearly identified [97], [98]. It was also mentioned that this enhancement can produce sharp band bending at the interface and consequently promote tunneling across the Schottky barrier.

A further hypothesis for improvement of charge injection in OTFTs based on CNT electrodes is that because of the conjugated structure of both CNTs and organic semiconductors, the CNTs can provide better contacts for organic semiconductors compared to metal electrodes.

1.6 Objectives of this work

The long-term objective of this work is to exploit SWCNT array electrodes to improve the charge injection in bottom-gate bottom-contact OTFTs [99], [100].

The approach is comparative i.e. it consists in comparing *conventional* metal electrodes (Au) and *novel* SWCNT array electrodes. The hypotheses underlying the adopted approach are the following:

- The 1D structure of CNTs facilitate charge carrier injection by field emission;
- The conjugated structure that CNTs and organic semiconductors have in common provides a favorable electrode/organic semiconductor interface, with low density of charge carrier traps.

SWCNT array electrodes have been already successfully applied to pentacene, PCBM, and CuPc TFTs [70], [93], [94].

However, to assess the general validity of the SWCNT array electrodes/organic semiconductor contact scheme to promote charge injection in OTFTs, a large number of experiments need to be carried out with different classes of organic semiconductors (e.g., polymers and small molecules) and different processing techniques (e.g., solution processing and vacuum sublimation).

The specific objective of this MSc is then to characterize the charge injection performance of OTFTs making use of SWCNT array electrodes and, as the organic semiconductor, solution processable P3HT polymer and P3HT/PCBM blends, and, the vacuum processable (supersonic molecular beam epitaxy [SuMBE]) Titanyl-phthalocyanine (TiOPc) molecule. These organic semiconductors were selected to confirm and extend the results previously observed [70], [93], [94] (Figure 1.9).

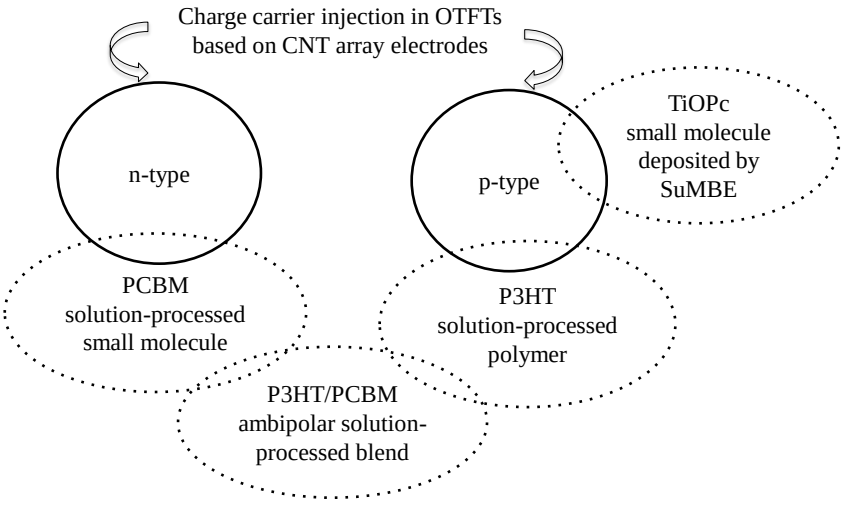

Figure 1.9: Scheme of the different organic semiconductors considered in this MSc work to investigate the behavior of SWCNT array electrodes in OTFTs.

We investigated vacuum deposited films of an organic semiconductor belonging to the metal phthalocyanine family, TiOPc, to extend the results previously observed with CuPc (p-type) [94]. Specifically, TiOPc films were deposited using the SuMBE technique.

P3HT was selected since this is a well-investigated polymer semiconductor, considered as a model polymer for fundamental studies in organic electronics. To date there are no studies related to the combination of organic semiconducting polymers and SWCNT array electrodes in OTFTs.

P3HT/PCBM blends are an important example of bulk-heterojunction systems [101], i.e. systems where two (p- and n-type) organic semiconductors are mixed at the molecular/nanometric level. P3HT/PCBM ambipolar blends represent an interesting case of study since they enable the investigation of both electron and hole charge injection and transport in the same TFT. The study of blends opens the possibility to use CNT array electrodes in ambipolar devices such as OLETs.

CHAPTER 2 EXPERIMENTAL APPARATUS AND PROCEDURES

2.1 Electrode fabrication

Source (S) and drain (D) electrodes with concentric geometry were patterned on thermally grown SiO_2-on-doped Si substrate (vide infra) to obtain bottom-gate bottom-contact OTFTs. The concentric electrode geometry is the most suitable to evaluate the performance of common gate OTFTs, since it permits to circumvent parasitic currents [102]. The device structure used in this project is illustrated in Figure 2.1.

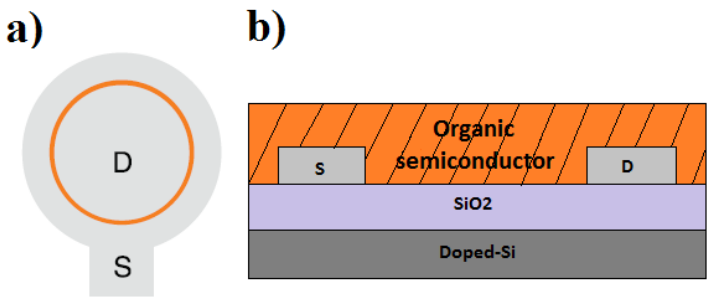

Figure 2.1: Structure of bottom-gate bottom-contact OTFTs used in this work: top view (a) and cross section (b). Doped Si served as substrate and G electrode.

The employed substrates were highly doped (n-type) Si (100) wafers (resistivity of 0.002-0.003 Ω·cm) covered with either 100 nm or 200 nm-thick thermally grown SiO_2 dielectric (100 nm: 34.5 nF/cm^2 capacitance, 200 nm: 17.26 nF/cm^2 capacitance), where Si acted as substrate and G electrode in OTFTs.

The first step to fabricate SWCNT array electrodes was vacuum filtration of the SWCNT solution using cellulose filters [103]. For this purpose, 2% sodium cholate aqueous dispersion of SWCNTs (1×10^{-4} mg/mL), a vacuum filtration apparatus, and a Millipore membrane filter with pore size of 0.22 μm were used. The vacuum filtration apparatus (Figure 2.2) includes a funnel that hosts the cellulose filters, a flask, and tubing connected to house vacuum (about 1 mTorr).

Figure 2.2: Vacuum filtration apparatus used in this work.

Typically, 4 mL of SWCNTs sodium cholate solution were diluted in 50 mL water. The density of the SWCNT network deposited on SiO_2 depends on the concentration of the SWCNT solution. Before filtering the SWCNT solution, the filter was wet with 50 mL of water to ensure adhesion of filter on funnel. The addition of SWCNT solution started when a small amount of water was still present in the funnel. After filtration, the cellulose filter containing the SWCNTs was dried for one day in ambient conditions.

The SiO_2/n-Si substrates were cut into small pieces (2 cm × 2 cm) and cleaned by sonication (using an Eumax ultrasonic cleaner UD100SH-4L) in isopropyl alcohol (IPA), acetone and again IPA for 5 mins, 10 mins, and 5 mins, respectively (IPA and acetone were obtained from J.T.Baker company). The SiO_2 surface was then treated with 1,1,1,3,3,3-hexamethyldisilazane (HMDS, Gelest, 99%) to improve adhesion of SWCNTs. HMDS was applied by spin coating (1000 rpm, for 1 min). Deposition of SWCNT networks on the SiO_2 surface of the substrates was achieved with the following procedure:

1. To transfer the SWCNTs from the cellulose filters to the SiO_2 surface, the filters were dipped in 1, 2-dichlorobenzene (DCB) for about 1 min.
2. The filter containing SWCNTs was placed on the SiO_2 surface treated with HMDS.
3. The substrate was gently rinsed with acetone to dissolve the cellulose filter.
4. When the filter on the substrate started to dissolve, the substrate was transferred into a beaker containing acetone for about 30 mins.

5. After dipping the SWCNT-coated substrate sequentially in acetone and IPA, 1 min for each dipping, the substrate was kept in acetone for 10 mins to ensure complete removal of the cellulose filter.
6. The procedure of SWCNT deposition was completed by rinsing the substrates with acetone, IPA and water, followed by gently drying with N_2 flow.

The SWCNT networks were then inspected with a field emission scanning electron microscopy (FE-SEM, Hitachi S-4700). The SEM images were acquired in the secondary electron imaging mode using the upper detector (Everhart-Thornley detector), at 1 keV accelerating voltage, and 1 μA emission current and 5 mm working distance. SWCNTs appear bright on an insulating substrate, when imaged under low accelerating voltage operation (Figure 2.3) [104].

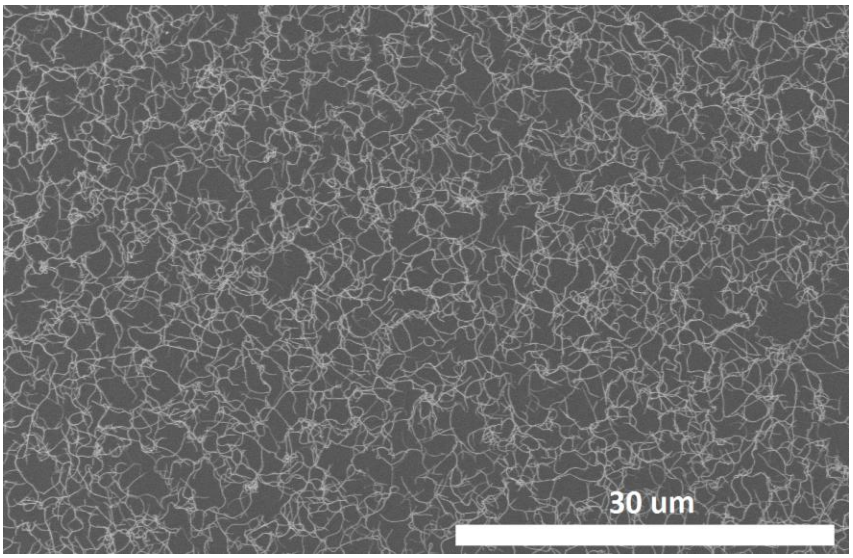

Figure 2.3: SEM image (1 keV, 7 μA) of a SWCNT network deposited on SiO_2.

The patterning of S and D electrodes was achieved by photolithography and lift-off in the LMF clean room (class 1000). The SWCNT-coated substrates were first kept on a hot plate at 190 ˚C for about 20 mins to remove adsorbed water. Then, the lift-off resist LOR 1A (Microchem) was spun onto the SWCNT-coated substrate at 2000 rpm for 1 min. After soft baking (at 190 ˚C for 3 mins), the positive tone photoresist S1805 (Shipley) was spun on LOR 1A and baked at 115 ˚C for 1 min. The sample was then exposed to UV light through a photo mask in a Karl Suss mask

aligner (MA-4). Hard contact in constant power mode was used for exposure. Two different photo masks were used to pattern concentric S and D electrodes with different W and L values (Figure 2.4).

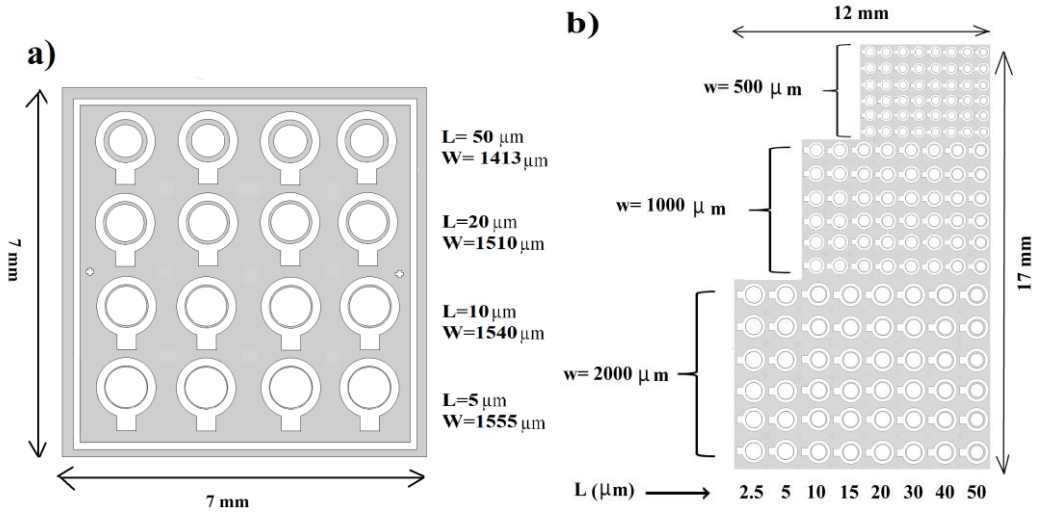

Figure 2.4: Two different photo masks for patterning circular S and D electrodes, used in this work. Each photo mask consists of several patterns of either (a) or (b).

The photoresist was then developed in MF319 (Microchem) developer for 75 seconds. The exposed regions of S1805 photoresist were dissolved in the developer leading at the same time to dissolution of the underlying LOR 1A layer from the opened windows. This procedure reproduces the patterns of the photo mask on photoresist. Finally, the photoresist-SWCNT-coated substrate was immersed in a beaker containing deionized water for 1 min, rinsed several times with deionized water in order to completely remove the residual developer, and dried with the N_2 jet.

Before deposition of the metal pads, the samples were inspected with SEM (Figure 2.5).

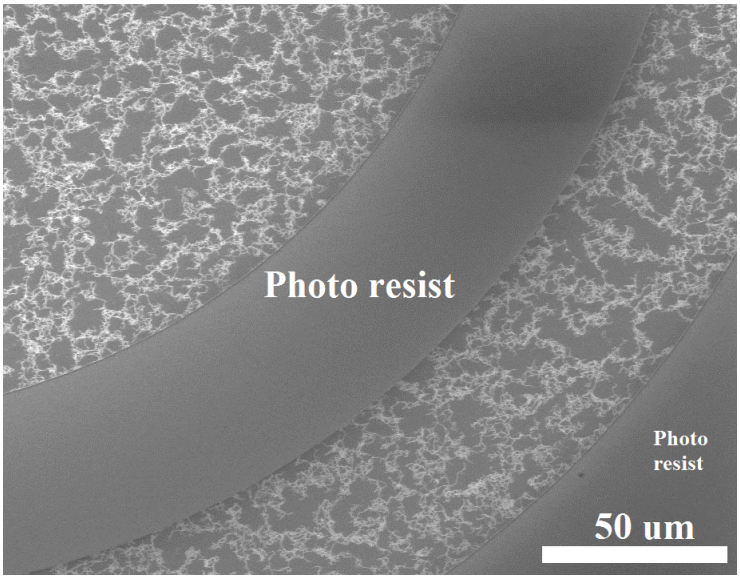

Figure 2.5: SEM image (1 keV, 7 µA) of the photoresist-SWCNT-coated substrate, after patterning the photoresist.

In order to make contact pads to SWCNT electrodes, a 20 nm-thick Ti film was deposited at a deposition rate of 0.1 nm/s using a Edwards Auto 306 electron beam evaporator in vacuum (10^{-6}-10^{-7} mbar) and patterned by a lift off process, which was achieved by immersing the sample in Remover PG (Microchem) at 70 ˚C for half an hour. This step was followed by rinsing the sample at room temperature with the remover PG and subsequently with IPA. Washing with deionized water and drying with N_2 were the last steps of the lift-off procedure. During lift-off, a Ti pattern, complementary to the photoresist pattern, was obtained (Figure 2.6).

The following step to complete the fabrication of SWCNT array electrodes was a sonication of the samples for a few minutes while immersed in AZ Stripper (AZ Electronic Materials). The sonication removes the SWCNTs not directly attached to the Ti pads and cuts the SWCNTs directly attached to the Ti pads such that only SWCNTs few hundreds of nanometers-long remain on the substrate. After sonication in AZ Stripper, the samples were immersed in IPA followed by washing in deionized water. The sonication time depends on the amount of SWCNT solution used in vacuum filtration; therefore it needs to be optimized for each sample. Figure 2.7 shows a SEM image of the sample with bright SWCNT arrays connected to metallic (Ti) pads.

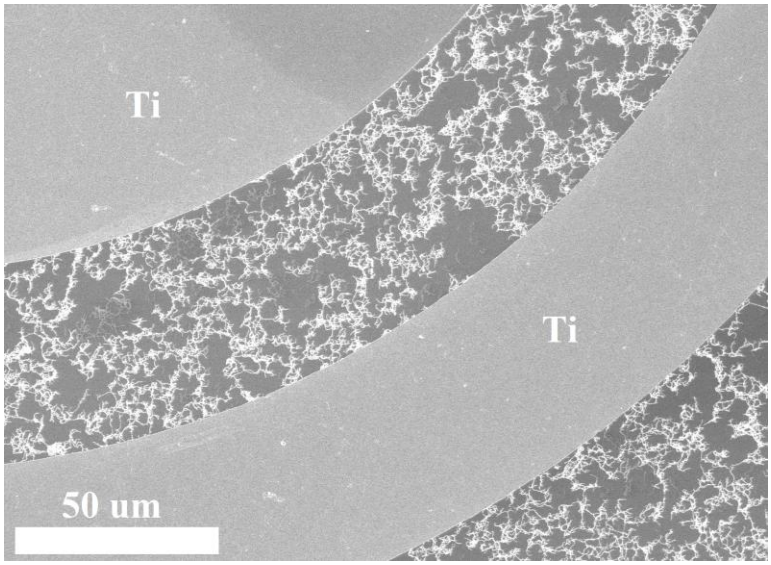

Figure 2.6: SEM image (1 keV, 7 µA) after patterning Ti pads on SWCNT-coated SiO_2/Si substrate.

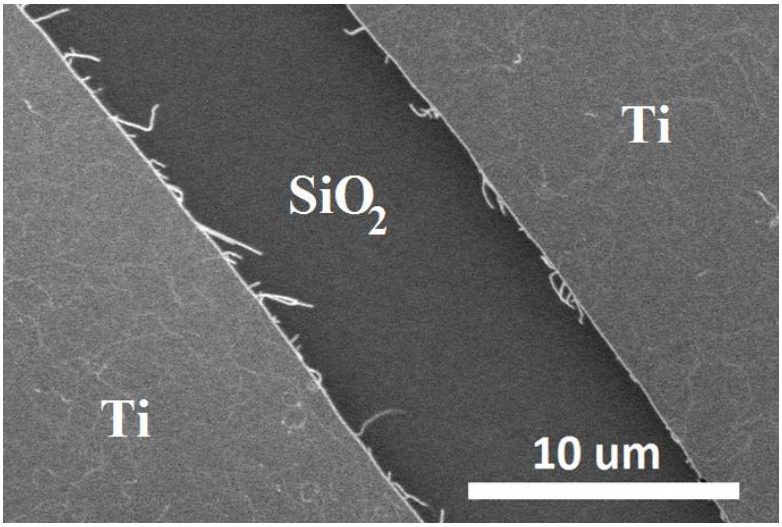

Figure 2.7: SEM image (1 keV, 7 µA) of SWCNT array electrodes after 4 mins-long sonication.

The last step of SWCNT array electrodes fabrication was the vacuum annealing of the Ti-SWCNT coated substrates in a vacuum oven (a Lindberg tube Furnace made of a quartz tube 61 cm long and 3.2 cm large in diameter, at a pressure of 10^{-6}-10^{-7} mbar) for one hour at 500 ˚C, to decreases the contact resistance between SWCNTs and metal electrodes [105]. Based on

literature data, we presume that this treatment desorbs HMDS deposited at the beginning of the procedure, leaving a bare SiO_2 surface[1] [106].

To benchmark our SWCNT array electrodes, OTFTs with Au S/D electrodes were also fabricated. Au electrodes were selected because they are used in most OTFTs. Au electrodes were fabricated using a photolithography process analogous to that one used for SWCNT electrodes, where the metallization step consisted of the deposition of a 3 nm thick Ti adhesion layer followed by 40 nm thick Au film. To facilitate the comparison with SWCNT electrodes, the samples were also annealed in vacuum at 500 ˚C for 1 h after lift-off.

Prior to organic semiconductor deposition, samples with SWCNT electrodes were cleaned by subsequent low power sonication in acetone and IPA for a few mins, finally rinsing with IPA and drying with N_2 flow. Substrates patterned with Au electrodes were cleaned by sonication in IPA, acetone, and IPA for 5 mins, 10 mins, and 5 mins, respectively, and dried with N_2 flows.

In this MSc work, we investigated the performance of three different organic semiconductors: TiOPc, P3HT, and P3HT/PCBM blends. Although, we mainly focused on a bare SiO_2 dielectric, we also performed a few preliminary experiments where SiO_2 was pre-treated with SAMs of HMDS and OTS. The SAM treatment of the SiO_2 surface is known to improve the performance of OTFTs by improving the wettability of the substrate surface where the organic films are deposited [107], [108]. The effect of SAMs has been demonstrated for OTFTs with conventional metallic electrodes: so far, there are no reports on the effect of SAMs on the performance of OTFTs with SWCNT electrodes.

2.2 Deposition of self assembled monolayers (SAMs)

SAMs treatment of SiO_2 is often used to improve the performance of OTFTs [109]. Two widely used materials for treatment of SiO_2 are hexamethyldisilazane (HMDS) and octadecylthrichlorosilane (OTS). The SAM is obtained by gas or solution methods.

[1] The characterization of the SiO_2 surface has not yet been performed.

In this work, HMDS (Gelest) was deposited by spin coating of HMDS, followed by annealing at 100 °C for 1 h on a hot plate. All the process was carried out in a N_2 glove box. Deposition of OTS was carried out in gas phase using a silanization oven constituted of: a sample holder covered with a bell jar, three valves, a Florence flask containing the OTS, and a mechanical pump. The three valves include: a nitrogen valve introducing N_2 into the bell jar; a vacuum valve to connect the bell jar to the mechanical pump; and a silanization valve to make a connection between the silane Florence flask and the bell jar. Before placing the substrates to be silanized in the silanization oven, the oven is heated at about 140 ˚C, in vacuum, for 2 hours. After cooling, the Florence flask is filled with liquid OTS and connected to the system. In order to purify OTS, several freeze-pump-thaw cycles were performed, keeping the Florence flask in a cup of liquid N_2 for a few mins. After freezing, OTS melted at room temperature. During the melting, the silanization and vacuum valves were opened to evacuate contaminant gases more volatile than OTS. This procedure was done for several times until no bubbling of contaminant gases from the OTS liquid was observed. After OTS purification, the temperature of the oven was set to 110 °C, and the temperature was monitored by means of a thermocouple connected to the sample holder. When the temperature was stabilized at 110 °C, OTS vapor was injected into the bell jar by closing the vacuum valve and opening the silanization valve. After three hours, the flow of OTS was stopped by closing the silanization valve. The silanized substrates were finally annealed at 120 °C for 30 mins in vacuum. This step allowed for the removal of OTS physisorbed on the SiO_2 surface. Before being characterized, the samples were rinsed in IPA, in an ultrasonic bath.

To characterize the quality of the SAM layer, the water contact angle technique was employed. Contact angle is generally used to measure the effects of surface treatments, and to explore the hydrophobic/hydrophilic behavior of dielectric surfaces. A low contact angle between the dielectric surface and the water drop indicates that the surface is hydrophilic. In general, the surface free energy can be deduced from contact angle measurements [110]. Water contact angle measurements (Rame-Hart NRL-100 contact angle goniometer) were performed on three different surfaces: SiO_2; SiO_2 treated with HMDS; and SiO_2 treated with OTS.

2.3 Deposition of organic semiconductors

Vacuum- and solution-based techniques were employed to deposit thin films of the organic semiconductors investigated in this project. TiOPc, P3HT, and P3HT/PCBM blends were the organic semiconductors selected for the fabrication of OTFTs. The procedures for the deposition of the organic semiconductors are illustrated in the following sections.

2.3.1 Vacuum-deposited organic semiconductors: the case of TiOPc

The deposition of TiOPc was carried out at the Institute of Materials for Electronics and Magnetism (IMEM) part of the Italian National Research Council (Trento). Thin films of TiOPc were deposited using supersonic molecular beam epitaxy (SuMBE), a technique exploiting the kinetic properties of an expanded neutral gas, seeded with TiOPc molecules, forced to expand in an UHV (ultra-high-vacuum) chamber. After the supersonic expansion, a highly focused beam of TiOPc molecules with high kinetic energy (15 eV, to be compared with 0.2-0.5 eV in thermal evaporation) and narrow velocity distribution is obtained. The continuous free jet generated by the high-pressure seeded gas flows from a narrow nozzle into a vacuum chamber environment (Figure 2.8).

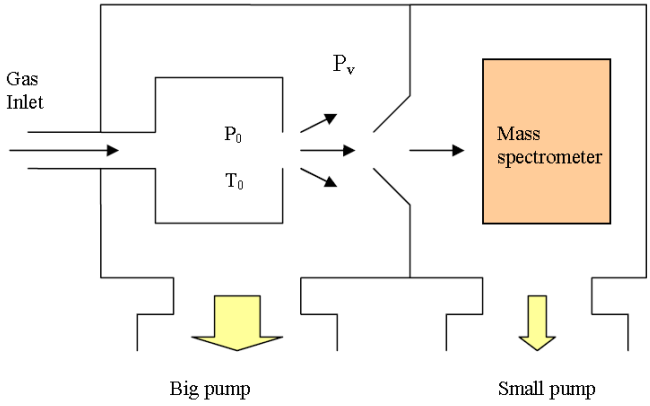

Figure 2.8: Basic scheme of a SuMBE apparatus with an inlet gas at a defined pressure

By accelerating the seeded molecules through mechanical hits and by controlling the degree of seeding of the molecules in the gas, it is possible to finely tune their kinetic energy in the beam [111], [112]. Therefore, skimming the supersonic beam and focusing on a substrate, it is possible to deposit thin films under UHV conditions [113]. The SuMBE technique provides for an

increased structural and morphological order of the deposited material. The high kinetic energy of the molecular beam, leading to an increase in molecular mobility on the surface, allows the formation of relatively large crystalline grains, with low density of grain boundaries [114].

The SuMBE system basically consists of a differentially pumped supersonic beam, a time of flight (TOF) mass spectrometer, and a deposition chamber. The supersonic beam source (Figure 2.9), placed in a high vacuum chamber, is made of a quartz tube equipped with a micrometric nozzle at the front end (typically 50 - 130 μm in diameter). An inert carrier gas (helium) is injected in the quartz tube at a controlled pressure (2 -3 bar). Inside the tube, TiOPc sublimed in a vessel by Joule heating is dispersed at very low concentrations into the carrier gas. Finally, the carrier gas containing seeded TiOPc expands through the source nozzle into the deposition chamber. A conical skimmer selects the central part of the beam, which proceeds to the sample in an UHV chamber. Film growth takes place under UHV conditions. The growth chamber hosts a TOF mass spectrometer to control the properties of the supersonic beam (kinetic energy, etc.), a microbalance to control the film nominal thickness, and sample manipulator.

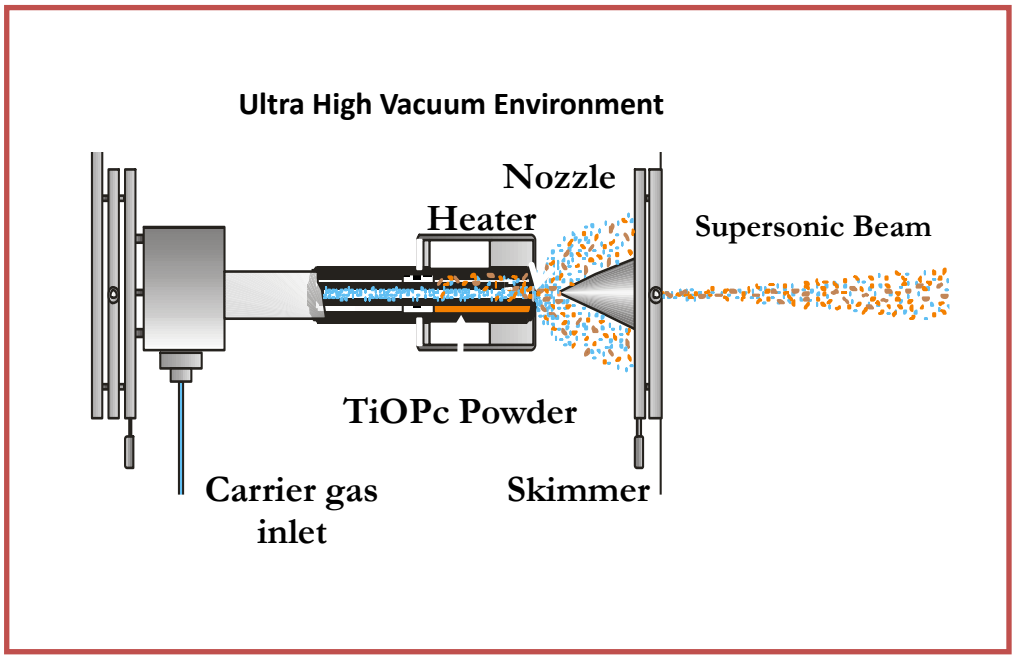

Figure 2.9: Scheme of the SuMBE system. Organic molecules (carrier gas) represented with orange (blue) color.

The deposition of TiOPc thin films was carried out using a kinetic energy of 15 eV and two different substrate temperatures: room temperature and 230 ˚C.

2.3.2 Poly-3 (hexylthiophene) (P3HT)

The preparation of the P3HT solution, the deposition of the thin films, and the film thermal treatment were carried out in a N_2 glove box (O_2 and H_2O concentration below 3 ppm). A Laurell spin coater (WS-400-6NPP), and a hot plate in the glove box were used for deposition and treatment of the films. Four different procedures were considered for P3HT thin film deposition. The procedures were the following ones:

Procedure 1): P3HT (Rieke Metals, molecular weight (M_w) ~ 50 kg/mol) solutions with a concentration of 5 mg/mL were prepared using chlorobenzene (anhydrous, Sigma Aldrich, boiling point: 131 ˚C) as the solvent. Thin films were prepared by spin coating from P3HT solutions at 2000 rpm onto cleaned substrates patterned with SWCNT array and Au electrodes [26].

Procedure 2): P3HT (Rieke Metals, M_w ~ 50 kg/ mol) solutions (3 mg/mL) in chloroform (Sigma Aldrich, boiling point: 61.2 ˚C) were spin coated onto cleaned Au and SWCNT array electrodes patterned substrates at 1000 rpm, followed by annealing at 100 °C for 1 hour [27]. Four substrates making use of 200 nm-thick SiO_2 were used. Two out of these four samples (one with Au and another one with SWCNT array electrodes) were treated with HMDS, followed by annealing at 100 ˚C in the glove box.

Procedure 3): The only difference compared to Procedure 2) was the use of 1,2-dichlorobenzene (DCB, Sigma Aldrich, boiling point: 180.5 ˚C) as the solvent, instead of chloroform.

Procedure 4): P3HT (SolarisChem, M_w ~ 80 kg/mol) was dissolved in DCB, at 3 mg/mL. Surface treatments with OTS and HMDS were performed on the SiO_2 surface. [28]. The thin films were spin coated at 1000 rpm for 1 min and annealed at 160 °C for 30 minutes. [115]

2.3.3 P3HT/ Phenyl-C61-butyric acid methyl ester (PCBM) blends

The procedures for the deposition of P3HT/PCBM blends are described below.

Procedure 1): Mixtures of P3HT (Rieke Metal, M_w ~ 50 kg/mol) and PCBM (KinTec) with weight ratio 1:4 were dissolved in chlorobenzene (5 mg/mL). Then the solutions were deposited

by spin coating in the N_2 glove box at 2000 rpm, 45 s, followed by annealing in N_2 at 100 °C for 1 h to remove solvent traces.

Procedure 2): P3HT/PCBM blends with weight ratio 1:1 were deposited via spin coating in the N_2 glove box (1000 rpm, 1 minute). The concentration of the chlorobenzene solutions was 10 mg/mL. P3HT (M_w ~ 80 kg/mol) was purchased from SolarisChem. PCBM was obtained from KinTec. The samples were then annealed at temperature of 100 ˚C for 30 mins [116].

Procedure 3): P3 HT/PCBM blends with weight ratio of 4:1 were deposited via spin coating in the N_2 glove box (1000 rpm, 1 minute at 10 mg/ml in chlorobenzene). P3HT (M_w ~ 80 kg/mol) was purchased from Solaris Chem. PCBM was obtained from KinTec. The samples were then annealed at temperature of 100 ˚C for 30 mins.

2.4 Charge transport characterization

The characterization of the OTFTs was performed under vacuum (10^{-5} Torr) in a Lake Shore Desert cryogenic electrical probe station connected to a semiconductor parameter analyzer (SPA, Agilent B1500A). Beryllium-Copper alloy (10 μm diameter) tips from Metal Specialty Co. were used. For each device, the output (I_D versus V_D at various V_G) and the transfer characteristics (I_D versus V_G at constant V_D) were measured. The voltage steps for V_D (V_G) were relatively low, i.e. either 500 or 100 mV, to properly analyze the OTFT characteristics in the linear regime, where the information on charge carrier injection can be extracted.

From the transfer characteristics recorded in the linear region, it is possible to extract the mobility in linear regime using the following equation [36]:

$$I_D = \frac{W}{L}\,\mu_{lin}\,C_i(V_G - V_{TH})V_D \qquad \text{Equation 2-1}$$

where *W* and *L* are the width and length of channel of the device, respectively, μ_{lin} the charge carrier mobility in linear regime and C_i is the capacitance per unit area of the gate dielectric.

The mobility in saturation regime and V_{TH} were extracted from the transfer curves in saturation, using the following equation:

$$I_D = \frac{W}{2L}\,\mu_{sat}\,C_i(V_G - V_{TH})^2 \qquad \text{Equation 2-2}$$

where μ_{sat} is the charge carrier mobility in saturation.

The subthreshold swing (SS) is defined as $dV_G/d\log_{10}I_D$ in the subthreshold region (where the V_G is lower than V_{TH}).

CHAPTER 3 RESULTS AND DISCUSSION

3.1 Characterization of OTFTs using SWCNT array and Au electrodes

The study of OTFTs using SWCNT array electrodes is at its early stages such that their electrical characterization has been systematically carried out, in this MSc work, by comparing the performance of SWCNT array OTFTs with those of OTFTs making use of benchmark Au electrodes. This *comparative* approach is meant to ensure the "disentanglement" of the effect of SWCNT array electrodes on the OTFT characteristics from other effects related to e.g. organic semiconductor chemical quality and processing. Au has been chosen as benchmark material since it is used as electrode material in most OTFTs.

We could have performed a comparison between OTFTs making use of SWCNT array electrodes with Ti pads and OTFTs making use of bare Ti electrodes. This kind of comparison has already been carried out and reported in the literature [70], [93]. The results showed that OTFTs making use of bare Ti electrodes provide an extremely poor device performance because of the presence of thin insulating TiO_2 layer.

In this project, we sought to investigate the effect of SWCNT array electrodes on OTFTs based on different families of organic semiconductors including phthalocyanines, polythiophenes, and fullerene derivatives. These semiconductors were processed using vacuum- and solution-based approaches, namely supersonic molecular beam epitaxy (SuMBE) and spin coating.

3.1.1 Charge transport characteristics of TiOPc-TFTs

Phthalocyanine compounds including TiOPc and CuPc are interesting because of their chemical and thermal stability (they are stable up to 400 ˚C [21]), non-toxicity, and relatively high mobility (about 10 $cm^2/V \cdot s$) [25], [117], [118], [22].

Single crystals of TiOPc generally exhibit p-type semiconducting behaviour when incorporated into TFT structures. On the other hand n-type behaviour was reported for single crystals TiOPc TFTs investigated under ultra high vacuum conditions [24].

In this MSc work, we investigated the characteristics of TFTs based on TiOPc thin films deposited by supersonic molecular beam epitaxy (SuMBE) and making use of SWCNT array electrodes.

Two different thin films of TiOPc were investigated, deposited at two different temperatures: room temperature and about 230 ˚C. For TFTs making use of room temperature (RT)-deposited TiOPc and Au S/D electrodes (hereafter referred to Au RT TiOPc TFTs), 16 devices out of 16 fabricated devices showed transistor behavior. For RT-deposited TiOPc, TFTs made with SWCNT array S/D electrodes (hereafter referred to SWCNT RT TiOPc TFTs), 6 devices out of 16 showed transistor behavior. Indeed, in the latter case, 10 out of 16 devices showed source-drain current in the range of mA, probably due to insufficient sonication time during fabrication of SWCNT array electrodes. After these series of results, we decided to improve our fabrication protocol, adopting a more strict one that included the measurement of the source-drain current right after electrode fabrication (before the deposition of the organic semiconducting films).

The output characteristics of SWCNT RT TiOPc TFTs and Au RT TiOPc TFTs (Figure 3.1) exhibit unipolar p-type behavior. To study the injection performance, the low voltage characteristics were investigated (Figures 3.1 c-d): for SWCNT RT TiOPc TFTs, at 0 V $\leq V_D \leq$ -5 V, the output curves showed a quasi linear (ohmic) behavior whereas a sublinear behavior was shown by Au RT TiOPc TFTs.

At V_D= -1 V and V_G= -60 V, I_D was ~ -0.4×10^{-7} A in SWCNT RT TiOPc TFTs and I_D was ~ -0.1×10^{-8} A in Au RT TiOPc TFTs. As a consequence we can say that the injection efficiency of SWCNT RT TiOPc TFTs is 40 times higher than that of Au RT TiOPc TFTs.

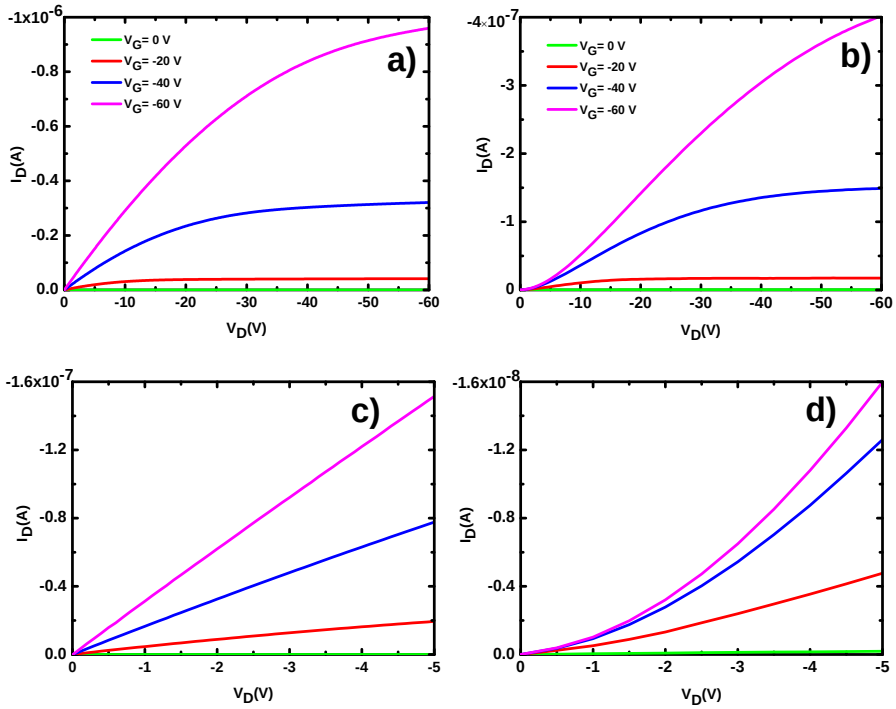

Figure 3.1: Output characteristics of: a) SWCNT RT TiOPc TFTs, and b) Au RT TiOPc TFTs. Output characteristics of : c) SWCNT RT TiOPc TFTs, and d) Au RT TiOPc TFTs, for 0 V ≤ V_D ≤ -5 V. V_D changes by 100 mV steps (W/L = 1540 µm/ 10 µm, 200 nm thick SiO_2).

Figure 3.2 shows the transfer characteristics of SWCNT RT TiOPc TFTs and Au RT TiOPc TFTs in both saturation and linear regimes. In saturation regime (V_D = -50 V), for -30 V < V_G < -60 V the square root of I_D is linearly dependent on V_G. Thus, based on Equation 2-2, the hole mobility can be extracted from the slope of the linear fit of the square root of I_D in that region. The V_{TH} is also found by extrapolating the linear fit to zero.

Figures 3.2 c) and d) show that I_D is linearly proportional to V_G at -30 V < V_G < -60 V, for V_D = -5 V. At present, we are trying to gain insight on the absence of linearity in the region V_G < -30 V. The hole mobility in the linear regime can be extracted by the slope of the linear fit of I_D.

Another important parameter extracted from the transfer curves, the I_{ON}/I_{OFF}, was 10^4-10^5 and 10^3-10^4 for V_D= -50 V and 0 V ≤ V_G ≤ -60 V for SWCNT RT TiOPc TFTs and Au RT TiOPc TFTs, respectively (Figure 3.2).

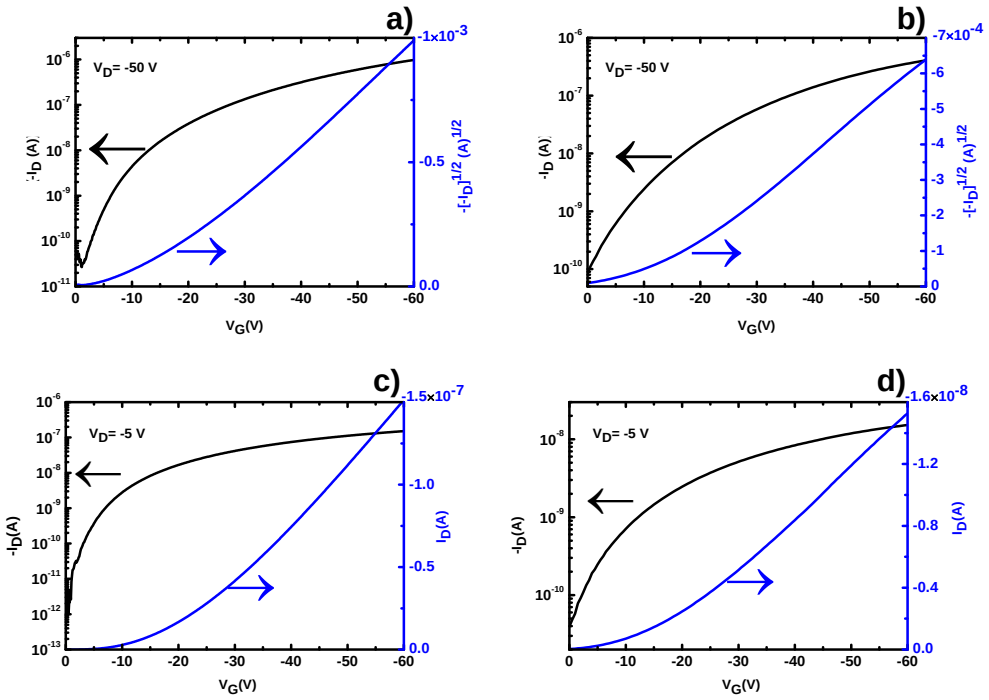

Figure 3.2: Transfer characteristics of: a) SWCNT RT TiOPc TFTs, and b) Au RT TiOPc TFTs at V_D = -50 V. Transfer characteristics of: c) SWCNT RT TiOPc TFTs, and d) Au RT TiOPc TFTs at V_D= -5 V. V_G changes by 100 mV steps (W/L = 1540 µm/ 10 µm, 200 nm thick SiO_2).

Hole mobility (μ_h) and threshold voltage (V_{TH}) of SWCNT RT TiOPc TFTs and Au RT TiOPc TFTs are illustrated in Figure 3.3. In the x-axis, Sat-CNT means that the figures of merit (i.e. μ_h and V_{TH}) have been calculated for SWCNT RT TiOPc TFTs at saturation. Sat-Au corresponds to the μ_h and V_{TH} calculated in the saturation regime for Au RT TiOPc TFTs. Lin-CNT and Lin-Au indicate the μ_h calculated at V_D= -5 V in SWCNT RT TiOPc TFTs and Au RT TiOPc TFTs, respectively. We included the calculated values, the average values, and the standard deviation in Figure 3.3.

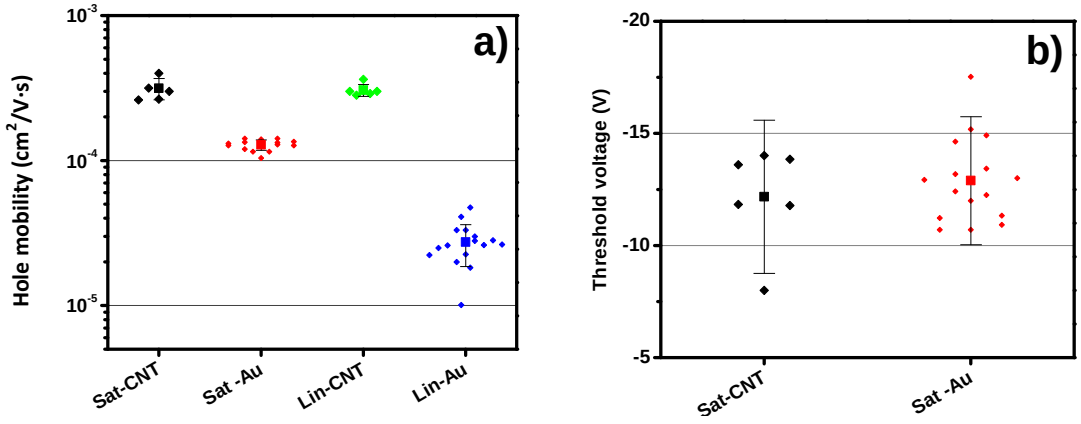

Figure 3.3: Hole mobility extracted in the saturation and linear regime a) and threshold voltage extracted in the saturation regime b), for SWCNT RT TiOPc TFTs and Au RT TiOPc TFTs. Error bars denote the standard deviation. L/W= 5/1555 µm/µm, L/W = 10/1540 µm/µm, L/W= 20/1510 µm/µm, L/W= 50/1413 µm/µm.

SWCNT RT TiOPc TFTs present higher μ_h than Au RT TiOPc TFTs, both in the saturation and the linear regimes. The average value of μ_h of 3.2×10^{-4} $cm^2/V\cdot s$ for SWCNT RT TiOPc TFTs and 1.3×10^{-4} $cm^2/V\cdot s$ for Au RT TiOPc TFTs were extracted at V_D= -50 V. The differences are more pronounced in linear regime (μ_h= 3.1×10^{-4} $cm^2/V\cdot s$ for SWCNT RT TiOPc TFTs, μ_h= 2.74×10^{-5} $cm^2/V\cdot s$ for Au RT TiOPc TFTs at V_D= -5 V), indicating the better performance of SWCNT array electrodes in comparison with Au electrodes at relatively low bias. The average value of V_{TH} for SWCNT RT TiOPc TFTs and Au RT TiOPc TFTs at V_D = -50 V were -12.2 V and -12.9 V, respectively.

The output characteristics of TFTs based on films of TiOPc deposited at 230 ˚C, making use of SWCNT array S/D electrodes (hereafter referred to SWCNT HT TiOPc TFTs) and Au S/D electrodes (hereafter referred to Au HT TiOPc TFTs) are illustrated in Figure 3.4.

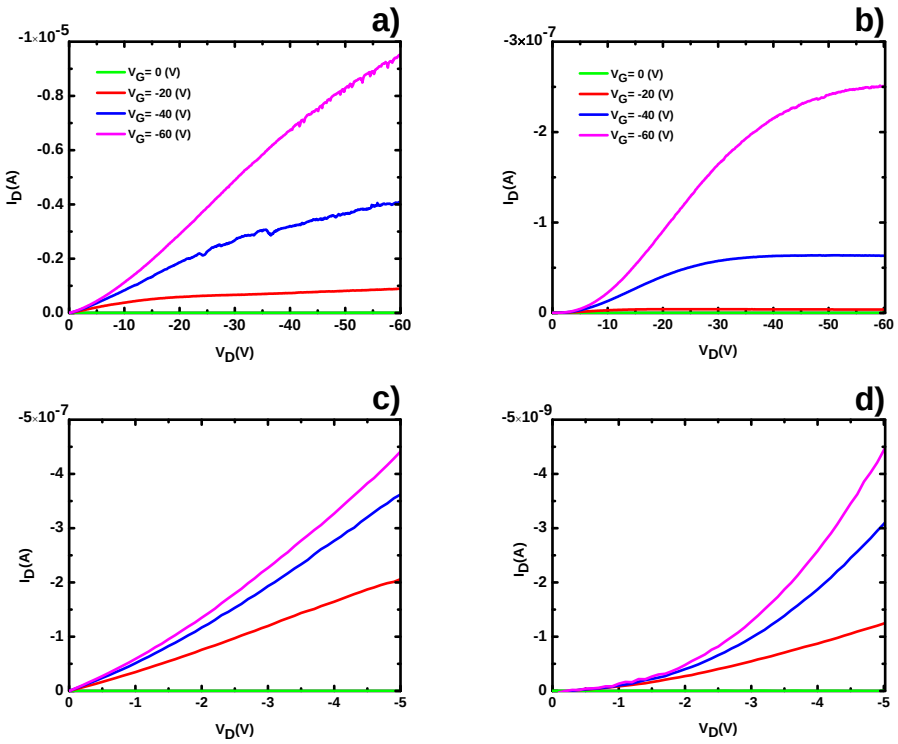

Figure 3.4: Output characteristics of: a) SWCNT HT TiOPc TFTs, and b) Au HT TiOPc TFTs. Output characteristics of: c) SWCNT HT TiOPc TFTs, and d) Au HT TiOPc TFTs, for 0 V ≤ V_D ≤ -5 V. V_D changes by 100 mV steps (W/L = 1540 µm/10 µm, 200 nm thick SiO_2).

At 0 V ≤ V_D ≤ -5 V, the output curves of SWCNT HT TiOPc TFTs show a quasi linear behavior whereas a clearly sublinear behavior is shown by Au HT TiOPc TFTs. The injection efficiency of SWCNT HT TiOPc TFTs is two orders of magnitude higher than Au RT TiOPc TFTs (as deduced by $I_D \sim -0.6\times10^{-7}$ A versus $I_D \sim -0.2\times10^{-9}$ A at V_D= -1 V, and V_G= -60 V for the two types of electrodes). As shown in Figure 3.4, at high V_D the curves are affected by a certain degree of noise. At present, the reasons for such noise are still under investigation. Possibly, this noise is correlated with the lack of a clear saturation *plateau*, observable in the same curves.

Figure 3.5 shows the transfer characteristics of SWCNT HT TiOPc TFTs and Au HT TiOPc TFTs in both saturation and linear regimes. A higher value of V_{ON} was observed in Au HT TiOPc TFTs. At V_D= -5 V, V_{ON} was -3 V in SWCNT HT TiOPc TFTs and -11 V for Au HT TiOPc TFTs.

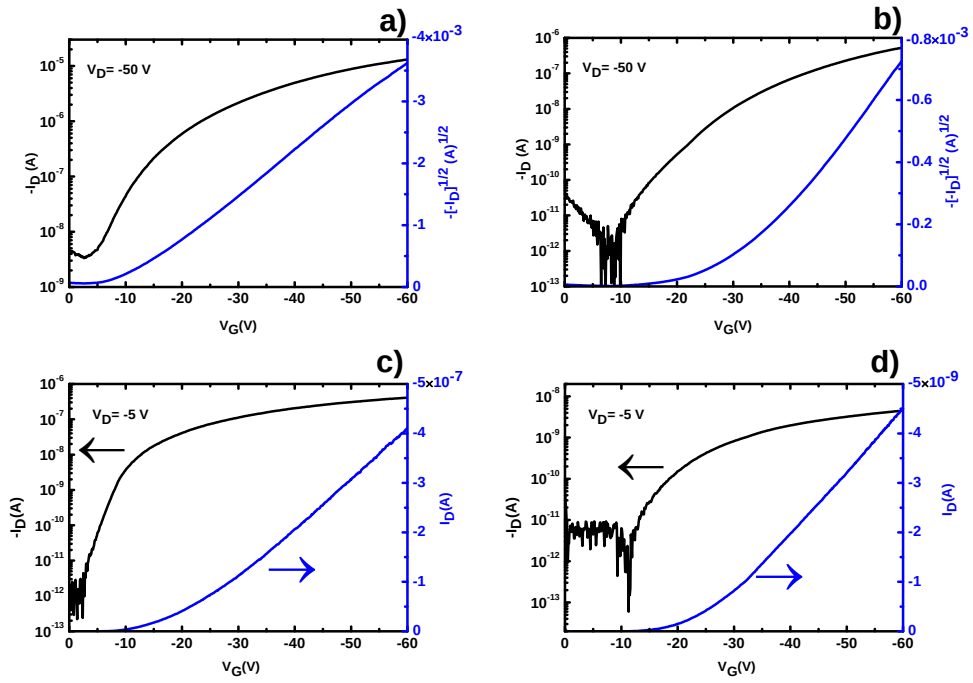

Figure 3.5: Transfer characteristics of: a) SWCNT HT TiOPc TFT, and b) Au HT TiOPc TFT at V_D = -50 V. Transfer characteristics of: c) SWCNT HT TiOPc TFT, and d) Au HT TiOPc TFT at V_D = -5 V. V_G changes by 100 mV steps (W/L = 1540 µm/ 10 µm, 200 nm thick SiO_2).

I_{ON}/I_{OFF} extracted from the transfer curves at V_D= -50 V and 0 V ≤ V_G ≤ -60 V was 10^4-10^5 and 10^3-10^4 for SWCNT HT TiOPc TFTs and Au HT TiOPc TFTs, respectively.

Figure 3.6 shows the hole mobility (μ_h) and threshold voltage (V_{TH}) of SWCNT HT TiOPc TFTs and Au HT TiOPc TFTs. The average values of μ_h were 1.2×10^{-3} $cm^2/V\cdot s$ and V_{TH} = -14.3 V for SWCNT HT TiOPc TFTs, obtained in the saturation regime (V_D = -50 V). These values compare with μ_h= 1.4×10^{-4} $cm^2/V\cdot s$ and V_{TH} = -32.6 for Au HT TiOPc TFTs. In the linear regime, μ_h= 3.3×10^{-4} $cm^2/V\cdot s$ and μ_h= 1.4×10^{-5} $cm^2/V\cdot s$ were extracted for SWCNT HT TiOPc TFTs and Au HT TiOPc TFTs, respectively.

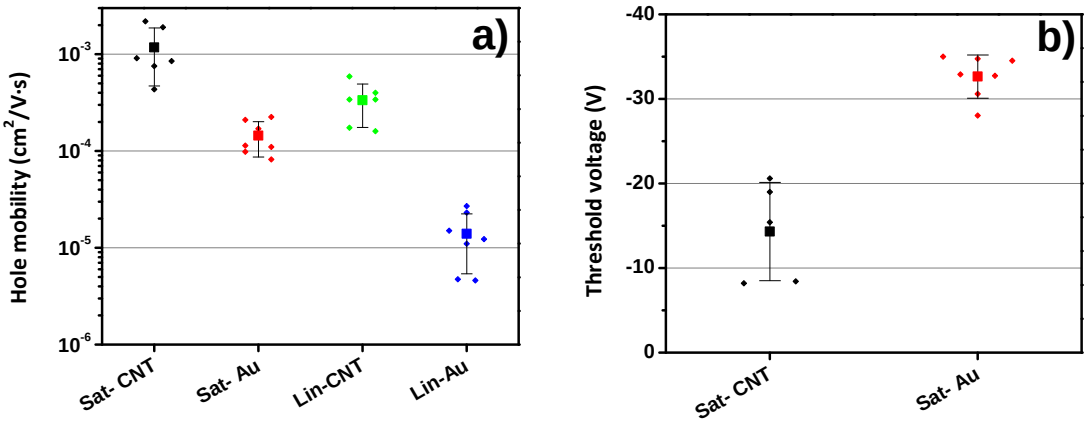

Figure 3.6: Hole mobility a) extracted in the saturation (V_D = -50 V) and the linear (V_D = -5 V) regimes, and threshold voltage b) extracted in the saturation regime (V_D = -50 V) of SWCNT HT TiOPc TFTs and Au HT TiOPc TFTs. Error bars denote the standard deviation. L/W= 5/1555 µm/µm, L/W = 10/1540 µm/µm, L/W= 20/1510 µm/µm, L/W= 50/1413 µm/µm.

It is worth noting that the unipolar p-type behavior of SWCNT HT TiOPc TFTs was converted to an ambipolar one by a vacuum annealing treatment 48 h-long (at 110 ˚C) [93], [94]. Figure 3.7 shows the output curves of SWCNT HT TiOPc TFTs in both hole and electron enhancement modes. Unluckily, the vacuum annealing treatment for Au HT TiOPc TFTs was not performed such that the comparison between the ambipolar behavior of SWCNT HT TiOPc TFTs against their Au counterparts was not possible.

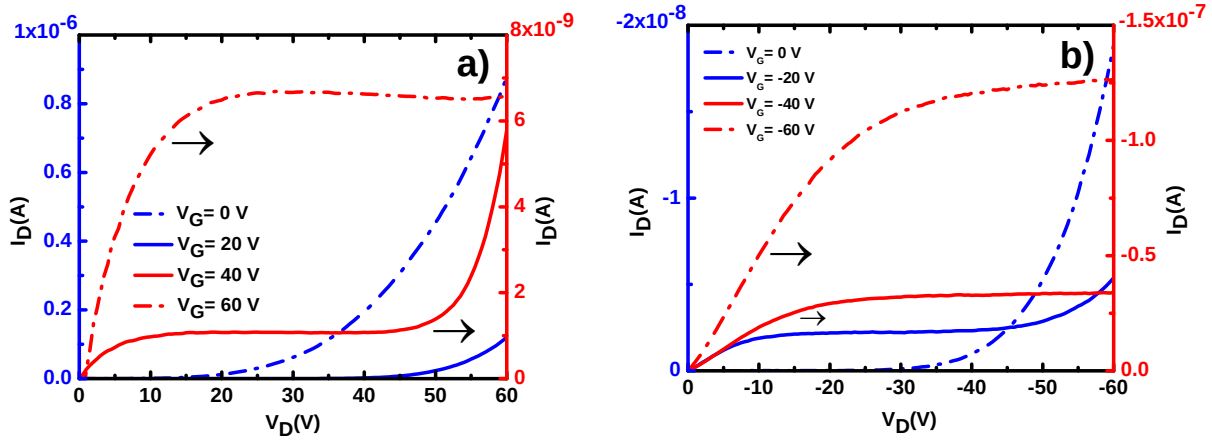

Figure 3.7: Output curves of SWCNT HT TiOPc TFTs for n-type a) and p-type operation b) after 48 h vacuum annealing treatment. The curves at V_G = 40 V and V_G = 60 V in panel a) and V_G= -40 V and V_G= -60 V in panel b) are referred to the right y scales. V_D changes by 500 mV steps (W/L = 1540 µm/10 µm, 200 nm thick SiO_2).

In conclusion, a more efficient injection was observed for both SWCNT RT TiOPc TFTs and SWCNT HT TiOPc TFTs. The injection efficiency in SWCNT RT TiOPc TFTs is 40 times higher than that in Au RT TiOPc TFTs. A two orders of magnitude higher injection efficiency was observed for SWCNT HT TiOPc TFTs in comparison with Au HT TiOPc TFTs.

To investigate the charge injection properties of SWCNT electrodes, the height of Schottky barriers at TiOPc/electrodes interface has to be considered. The energy band diagram of TiOPc HOMO-LUMO levels and SWCNT array and Au electrodes workfunctions is illustrated in Figure 3.8. From this diagram, a rough estimation of the barrier height for injection of holes can be made. The Fermi level of SWCNT array electrode is offset by about 1.1 eV with respect to the HOMO level of TiOPc. Along the same line, for Au electrodes the estimated injection barrier is 1.2 eV. Thus, large injection barriers are expected at the interface of SWCNT and Au electrodes with TiOPc. This should result in a rather poor hole injection performance (non linear behavior in the output transistor curves) for both electrodes, SWCNT array and Au.

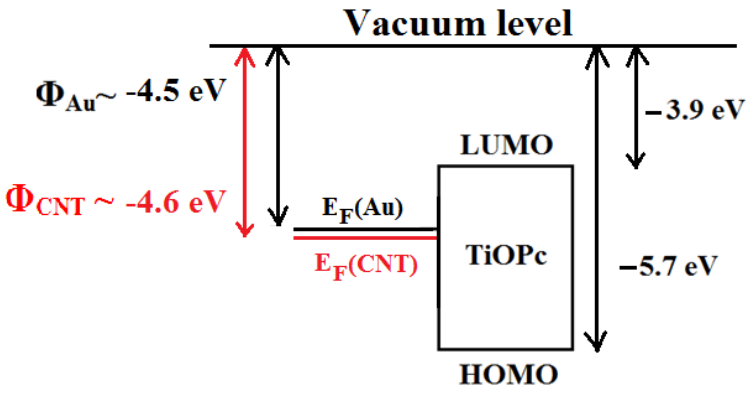

Figure 3.8: Energy band diagram of TiOPc (HOMO and LUMO, relative to the vacuum level) [23] and workfunction of SWCNT (Φ_{CNT}) [119] and Au (Φ_{Au}) [120] electrodes. E_F (Au) and E_F (CNT) are the Fermi levels of Au and SWCNT electrodes, respectively.

In Au RT TiOPc TFTs and Au HT TiOPc TFTs, the nonlinear output characteristics clearly indicate the presence of a Schottky barrier. On the other hand, the quasi linear output characteristics observed in SWCNT RT TiOPc TFTs and SWCNT HT TiOPc TFTs at low V_D voltages and the relative values of I_D obtained at low voltages for SWCNT array vs Au based TFTs indicate the presence of quasi electrically transparent barriers in the case of TFTs based on SWCNT array electrodes.

The injection mechanism from SWCNT array electrodes into TiOPc films cannot be completely understood by our experimental results. Therefore we cannot definitively indicate which properties of SWCNTs are responsible for the improved injection. We make the hypothesis that upon application of an electrical bias, higher electric fields are produced at the SWCNT array/TiOPc interface compared to the Au/TiOPc interface, due to the high aspect ratio of SWCNTs. In turn, these high electric fields should increase the probability of charge injection by tunneling mechanism. We also make the hypothesis that SWCNT array electrodes are able to provide favorable interface with TiOPc due to the π-π bonding between the SWCNTs and TiOPc. This favorable morphology should positively contribute to the efficiency of charge injection.

Apart from the improved charge injection process, a higher mobility was obtained for SWCNT RT TiOPc TFTs and SWCNT HT TiOPc TFTs in comparison with Au RT TiOPc TFTs and Au HT TiOPc TFTs, especially in the linear regime. A maximum μ_h of 0.001 $cm^2/V{\cdot}s$ was extracted

for SWCNT HT TiOPc TFTs while μ_h was 1.4×10^{-4} $cm^2/V\cdot s$ in Au HT TiOPc TFTs. V_{TH} = -14.3 V was obtained in SWCNT HT TiOPc TFTs whereas the V_{TH} was -32.6 V in Au HT TiOPc TFTs.

3.1.2 Charge transport characteristics of P3HT-TFTs

P3HT, belongs to the family of polythiophenes and is a p-type solution-processable polymeric semiconductor that can be easily processed in a number of common organic solvents [26–29], [121].

In this MSc project, the performance of OTFTs making use of P3HT as the organic semiconductor and SWCNT array and Au as the electrodes were investigated. As mentioned in Chapter 2, the preparation of OTFTs based on P3HT was carried out using four distinct procedures. We would like to discuss here the results of the 4th procedure, being this one the procedure that produced by far the most interesting TFTs, in terms of performance. The results of the 1st, 2nd and 3rd procedures are available in the appendices. In the 4th procedure, different SiO_2 surface treatments using HMDS and OTS were carried out.

The output characteristics of P3HT TFTs making use of SWCNT array S/D electrodes (referred to SWCNT P3HT TFTs) and P3HT TFTs making use of Au S/D electrodes (referred to Au P3HT TFTs) are illustrated in Figure 3.9. A quasi linear behavior is observed in SWCNT P3HT TFTs at low voltages ($0\ V \leq V_D \leq -2\ V$) while a sublinear behavior is observed in Au P3HT TFTs, indicating that the current is limited by the contact barriers. Moreover, the values of the transistor current observed at V_D = -1 V and V_G = -40 V ($I_D \sim -1.5\times10^{-7}$ A for SWCNT P3HT TFTs versus $I_D \sim -1.2\times10^{-8}$ A for Au P3HT TFTs) reveal that SWCNT P3HT TFTs have one order of magnitude higher injection efficiency than Au P3HT TFTs.

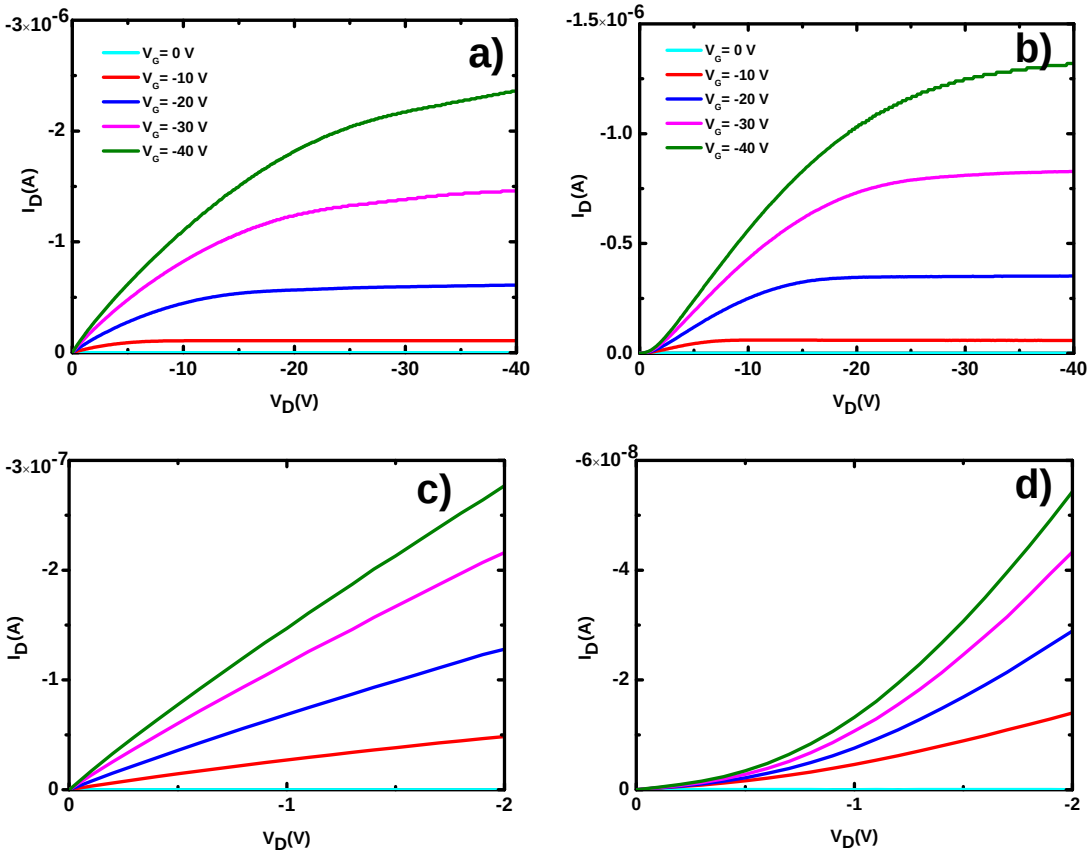

Figure 3.9: Output characteristics of: SWCNT P3HT TFTs a), and Au P3HT TFTs b). Output characteristics of: SWCNT P3HT TFTs c) and Au P3HT TFTs d), for 0 V ≤ V_D ≤ -2 V. V_D changes by 100 mV steps (W/L = 1540 µm/ 10 µm, 100 nm thick SiO_2).

Figure 3.10 shows the transfer curves of SWCNT P3HT TFTs and Au P3HT TFTs. SWCNT P3HT TFTs and Au P3HT TFTs show I_{ON}/I_{OFF} in the range of 10^5-10^6 and 10^4 -10^5, respectively. At V_D = -2 V, V_{ON} of about -6.5 V was obtained in both SWCNT P3HT TFTs and Au P3HT TFTs.

The improvement of the injection process in SWCNT P3HT TFTs over their Au counterparts was also observed when the SiO_2 surface was treated with HMDS and OTS SAMs (the corresponding devices will be from now on referred to SWCNT HMDS P3HT TFTs, SWCNT OTS P3HT TFTs, Au HMDS P3HT TFTs and Au OTS P3HT TFTs).

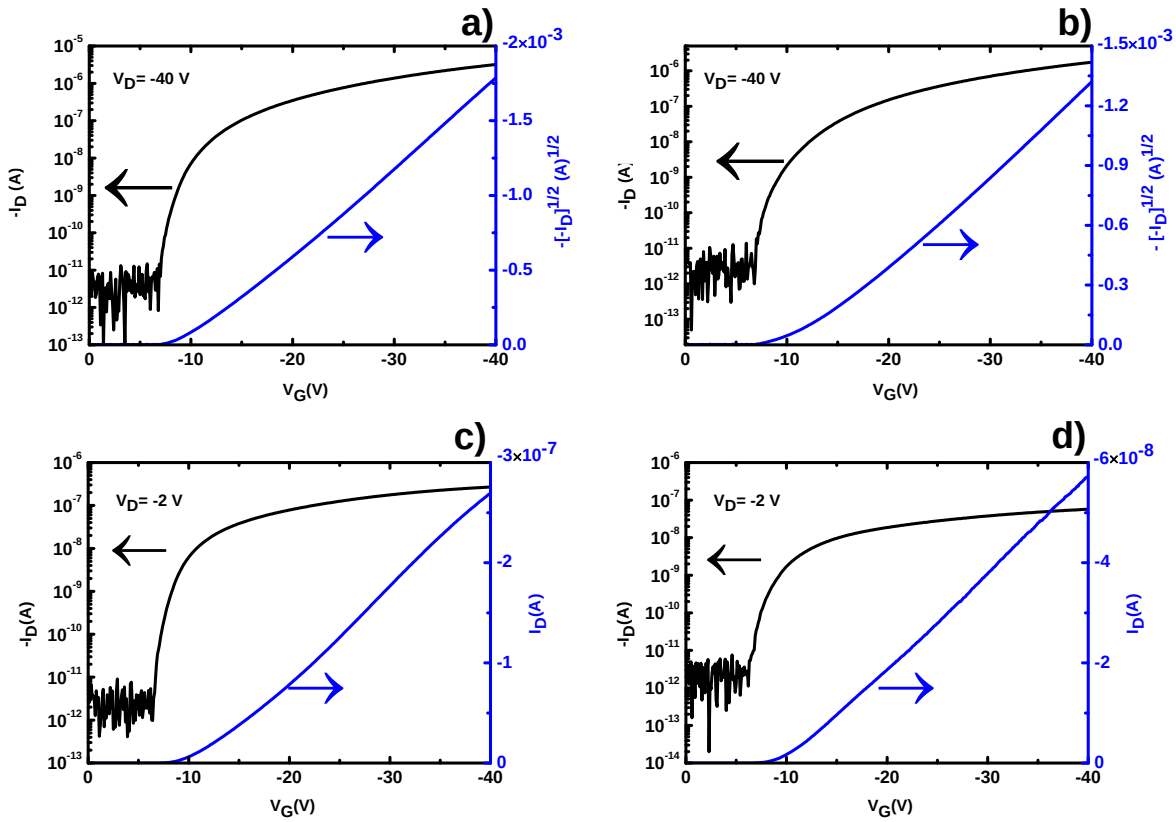

Figure 3.10: Transfer characteristics of: SWCNT P3HT TFTs a) and Au P3HT TFTs b), for V_D = -50 V. Transfer characteristics of: SWCNT P3HT TFTs c) and Au P3HT TFTs d), for V_D = -2 V. V_G changes by 500 mV steps (W/L = 1540 µm/ 10 µm, 100 nm thick SiO_2).

The output and transfer characteristics of SWCNT HMDS P3HT TFTs and Au HMDS P3HT TFTs are illustrated in Figure 3.11. The injection efficiency of SWCNT HMDS P3HT TFTs was 16 times higher than that of Au HMDS P3HT TFTs (obtained considering $I_D \sim -2.2\times10^{-7}$ A versus $I_D \sim -1.3\times10^{-8}$ A at V_D = -1 V, V_G = -40 V for these two types of TFTs). At V_D= -2 V,V_{ON} of -4 V was obtained in SWCNT HMDS P3HT TFTs and V_{ON} was about -6 V for Au HMDS P3HT TFTs.

Figure 3.12 shows the output and transfer characteristics of SWCNT OTS P3HT TFTs and Au OTS P3HT TFTs. The injection efficiency of SWCNT OTS P3HT TFTs was 3 times higher than that of Au OTS P3HT TFTs, as obtained from $I_D \sim -0.75\times10^{-7}$ A and $I_D \sim -2.5\times10^{-8}$ A at V_D = -2 V, V_G = -40 V, for these two types of electrodes.

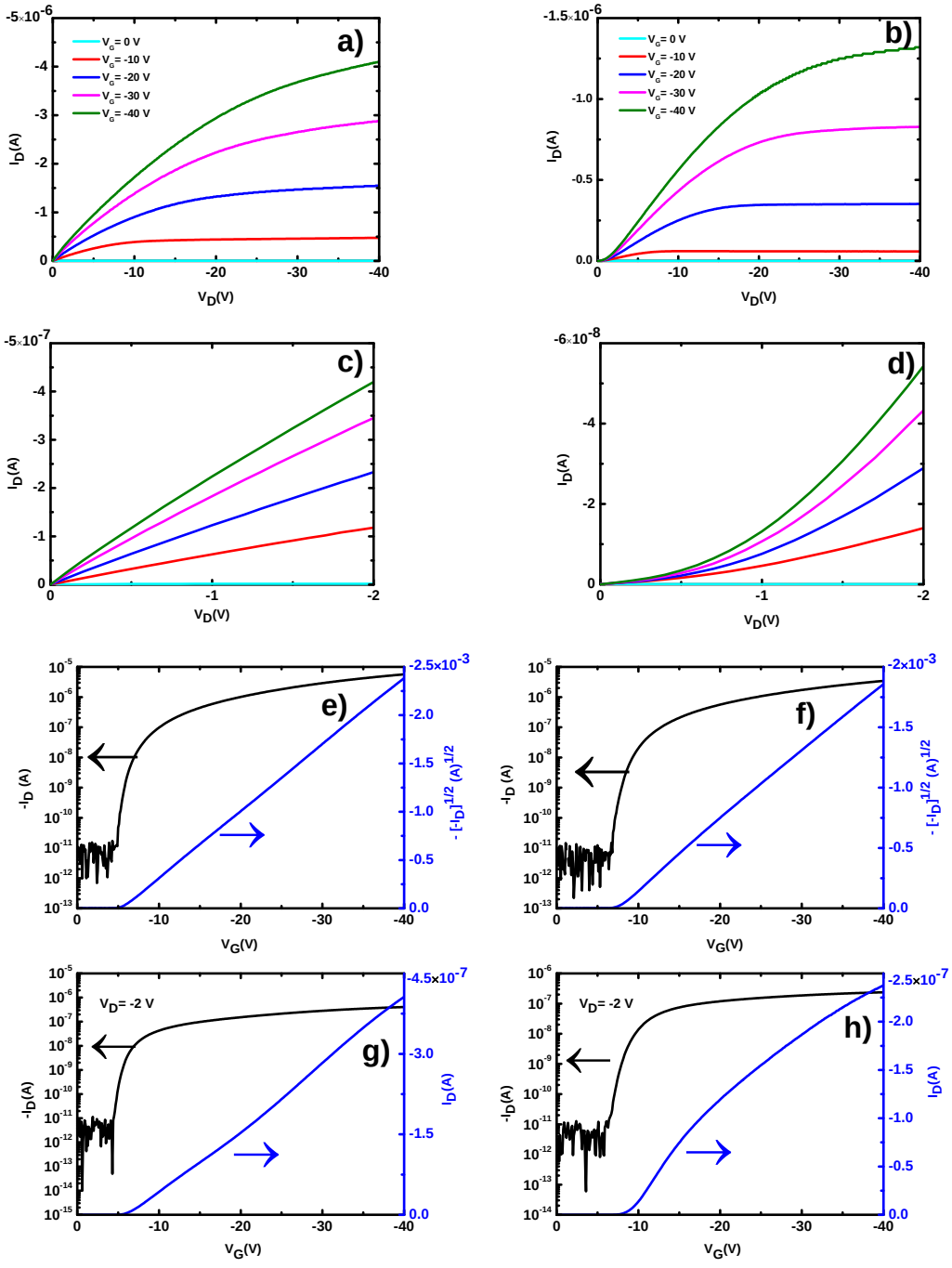

Figure 3.11: Output characteristics of: SWCNT HMDS P3HT TFTs a) and Au HMDS P3HT TFTs b). Output characteristics of: SWCNT HMDS P3HT TFTs c) and Au HMDS P3HT TFTs d), for 0 V $\leq V_D \leq$ -2 V. Transfer characteristics of the same devices for V_D = -50 V with SWCNT e) and Au f) and, for V_D = -2 V, with SWCNT g) and Au h). V_D (V_G) changes by 100 mV steps (W/L = 1540/10 µm, 100 nm thick SiO_2).

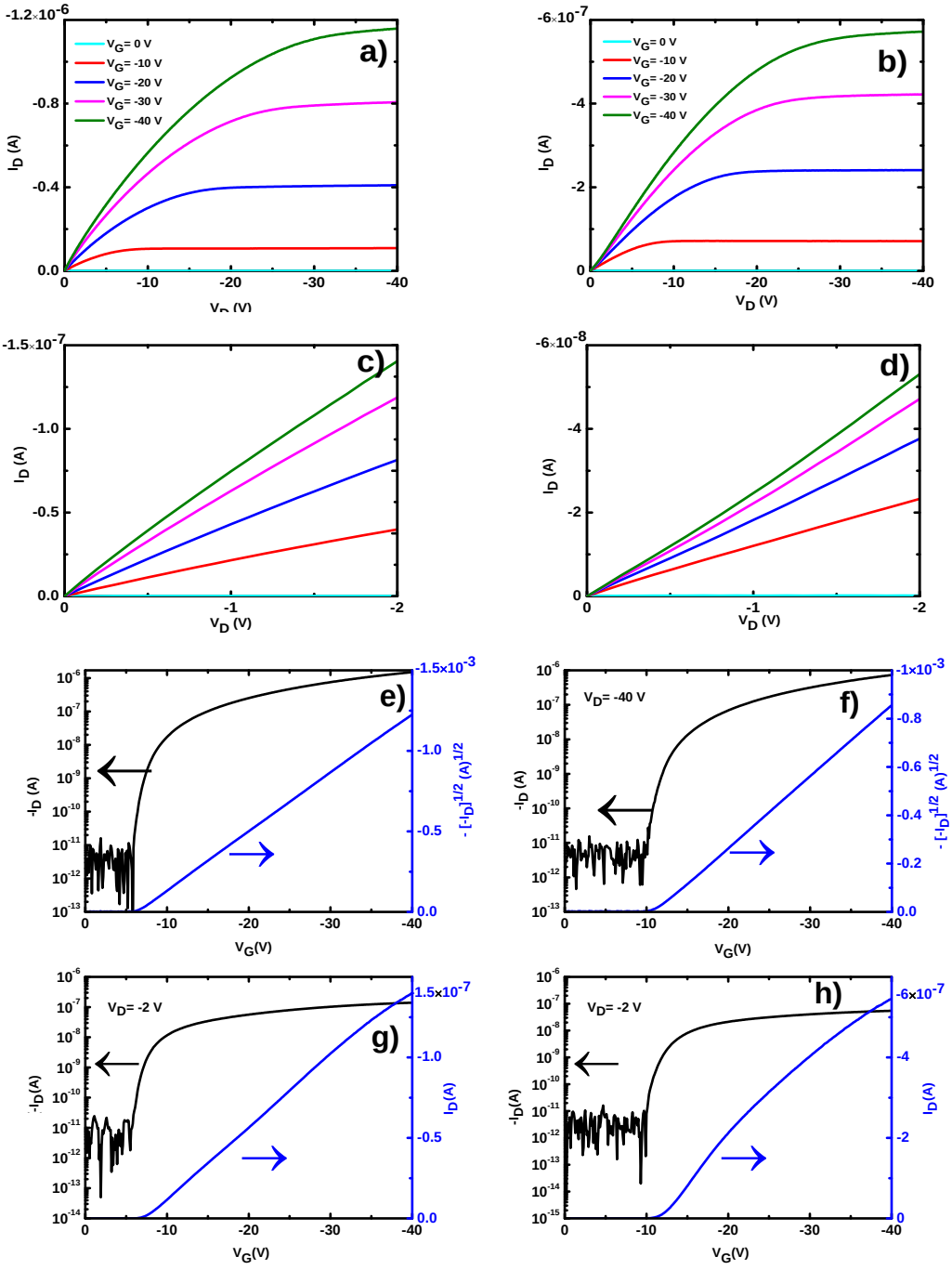

Figure 3.12: Output characteristics of: SWCNT OTS P3HT TFTs a) and Au OTS P3HT TFTs b). Output characteristics of: SWCNT OTS P3HT TFTs c) and Au OTS P3HT TFTs d) for 0 V ≤ V_D ≤ -2 V. Transfer characteristics of the same device for V_D = -50 V, with SWCNT e) and Au f), and, for V_D = -2 V, for SWCNT g) and Au h). V_D (V_G) changes by 500 mV steps (W/L = 1510 µm/ 20 µm, 100 nm thick SiO_2).

At V_D= -2 V, a value for V_{ON} of -5 V was obtained in SWCNT OTS P3HT TFTs. V_{ON} was about -10 V for Au OTS P3HT TFTs.

SWCNT HMDS P3HT TFTs (SWCNT OTS P3HT TFTs) and Au HMDS P3HT TFTs (Au OTS P3HT TFTs) show I_{ON}/I_{OFF} in the range of 10^5- 10^6 and 10^4-10^5, respectively.

Hole mobility extracted in both saturation (V_D = -40 V) and linear (V_D = -5 and -2 V) regimes and threshold voltage of SWCNT P3HT TFTs, Au P3HT TFTs, SWCNT HMDS P3HT TFTs, Au HMDS P3HT TFTs, SWCNT OTS P3HT TFTs, and Au OTS P3HT TFTs are illustrated in Figure 3.13. In the x-axis, CNT-HMDS, CNT-OTS, CNT, Au, Au-HMDS, and Au-OTS correspond to the figures of merit (i.e. μ_h and V_{TH}) calculated for SWCNT HMDS P3HT TFTs, SWCNT OTS P3HT TFTs, SWCNT P3HT TFTs, Au P3HT TFTs, Au HMDS P3HT TFTs, and Au OTS P3HT TFTs, respectively. We included in the figure the calculated values, the average values, and the standard deviation. SWCNT P3HT TFTs present higher average value of μ_h than Au P3HT TFTs in saturation and linear regime. The average value of μ_h at V_D = -40 V was 1×10^{-3} $cm^2/V\cdot s$ and 4.1×10^{-4} $cm^2/V\cdot s$ for SWCNT P3HT TFTs and Au P3HT TFTs, respectively (μ_h = 7.6×10^{-4} $cm^2/V\cdot s$ and μ_h = 2.7×10^{-4} $cm^2/V\cdot s$ were observed at V_D = -5 V and μ_h = 7.3×10^{-4} $cm^2/V\cdot s$ and μ_h = 1.4×10^{-4} $cm^2/V\cdot s$ were observed at V_D = -2 V, for these two types of devices, respectively).

At V_D = -40 V, the μ_h values obtained for SWCNT P3HT TFTs and Au P3HT TFTs (fabricated on SiO_2, SiO_2 treated with HMDS, or SiO_2 treated with OTS surfaces) are similar. On the other hand, at V_D = -2 V, SWCNT P3HT TFTs have higher values of μ_h compared to Au P3HT TFTs. This can indicate that the differences between SWCNT P3HT TFTs and Au P3HT TFTs are more pronounced at low electrical bias, for the three surfaces investigated (SiO_2, SiO_2 treated with HMDS, or SiO_2 treated with OTS).

SWCNT HMDS P3HT TFTs present an average value of μ_h of 1.2×10^{-3} $cm^2/V\cdot s$, 9.2×10^{-4} $cm^2/V\cdot s$, and 9.3×10^{-4} $cm^2/V\cdot s$ at V_D of -40 V, -5 V, and -2 V, respectively. These values are 5.3×10^{-4} $cm^2/V\cdot s$, 4.4×10^{-4} $cm^2/V\cdot s$, and 4.1×10^{-4} $cm^2/V\cdot s$ in Au HMDS P3HT TFTs. These results show that the mobility is enhanced in SWCNT HMDS P3HT TFTs compared to Au HMDS P3HT TFTs.

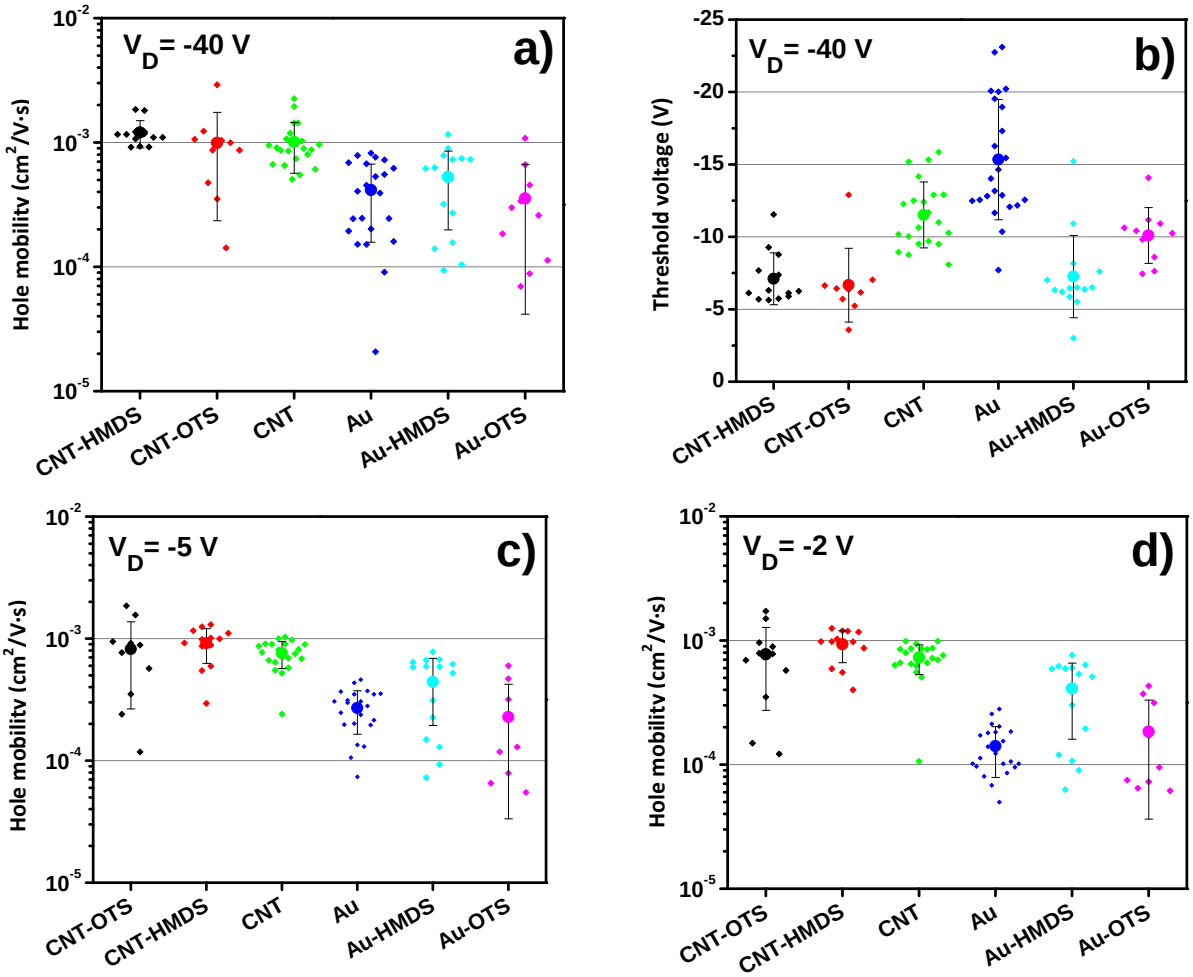

Figure 3.13 : Hole mobility a), threshold voltage b) extracted in saturation regime (V_D = -40) and hole mobility extracted at V_D = -5 V c) and V_D = -2 V d) for SWCNT P3HT TFTs, Au P3HT TFTs, SWCNT HMDS P3HT TFTs, Au HMDS P3HT TFTs, SWCNT OTS P3HT TFTs, Au OTS P3HT TFTs. The error bars denote the standard deviation. L/W= 5/1555 µm/µm, L/W = 10/1540 µm/µm, L/W= 20/1510 µm/µm, L/W= 50/1413 µm/µm.

When the mobility of SWCNT P3HT TFTs (Au P3HT TFTs) and SWCNT HMDS P3HT TFTs (Au HMDS P3HT TFTs) are compared, a slight improvement in the mobility values is observed by HMDS treatment, for both types of electrode (SWCNT array and Au).

The average values of 9.9 $\times 10^{-4}$ cm^2/V·s, 8.2$\times 10^{-4}$ cm^2/V·s, and 7.7$\times 10^{-4}$ cm^2/V·s at V_D of -40 V, -5 V, and -2 V were obtained for the mobility in SWCNT OTS P3HT TFTs, respectively. Values

for Au OTS P3HT TFTs were 3.5×10^{-4} $cm^2/V\cdot s$, 2.3×10^{-4} $cm^2/V\cdot s$, and 1.8×10^{-4} $cm^2/V\cdot s$ at V_D of -40 V, -5 V, and -2 V, respectively.

The average values of threshold voltage for all devices were: -11.5 V for SWCNT P3HT TFTs, -15.3 V for Au P3HT TFTs, -7.1 V for SWCNT HMDS P3HT TFTs, -7.3 V for Au HMDS P3HT TFTs, -6.7 V for SWCNT OTS P3HT TFTs, and -10.1 V for Au OTS P3HT TFTs. SWCNT array electrode-based devices have lower threshold voltage than Au based devices.

A decrease of V_{TH} is obtained for both types of electrodes (SWCNT array and Au) using OTS and HMDS treatment of SiO_2. This effect can be attributed to the improvement of interface between P3HT and the substrates. The influence of the surface treatment of SiO_2 with SAMs of HMDS and OTS on the performance of OTFTs has been investigated by many research groups. It is widely recognized nowadays that the treatment of the SiO_2 surface with SAMs results in a complex interplay of effect such as morphology and structure changes in the organic semiconducting films and decrease in the density of the charge carrier traps at the semiconducting film/gate dielectric interface [107], [109], [122]. The characteristics of the transistors making use of SiO_2 treated surfaces indicate a strong effect of OTS and HMDS SAMs on the value of V_{TH}. The lower V_{TH} values obtained when OTS and HMDS SAMs were used, point to the effectiveness of such treatments in limiting the interfacial density of the charge carrier traps.

To gain insight into the role of the SAM treatment on the TFT performance, we performed the measurement of the water contact angle on the bare SiO2, HMDS-treated SiO_2, and OTS-treated SiO_2 surfaces. The values of the water contact angle measured on SiO_2, HMDS-treated SiO_2, and OTS-treated SiO_2 surfaces are reported in Table 3-1. The values of the angles, higher for HMDS- and OTS-treated SiO_2 surfaces than for bare SiO_2, indicate the more hydrophobic character of the SAM-treated surfaces, as expected.

Table 3-1: Water contact angles for SiO_2, HMDS-treated SiO_2, and OTS-treated SiO_2.

Surface	**SiO_2**	**HMDS-treated SiO_2**	**OTS-treated SiO_2**
Contact angle	25˚	55˚	81˚

Overall, a better injection behavior was observed in SWCNT P3HT TFTs, SWCNT HMDS P3HT TFTs, and SWCNT OTS P3HT TFTs in comparison with the same devices using Au electrodes. SWCNT P3HT TFTs have one order of magnitude higher injection efficiency than Au P3HT TFTs. The injection efficiency of SWCNT HMDS P3HT TFTs was 16 times higher than that of SWCNT HMDS P3HT TFTs. The injection efficiency of SWCNT OTS P3HT TFTs was 3 times higher than that of Au OTS P3HT TFTs.

We can estimate the barrier height for injection of holes from Au to P3HT by knowing the work function of Au and the HOMO level of P3HT. The energy level diagram for P3HT and the workfunction of SWCNT and Au electrodes are illustrated in Figure 3.14.

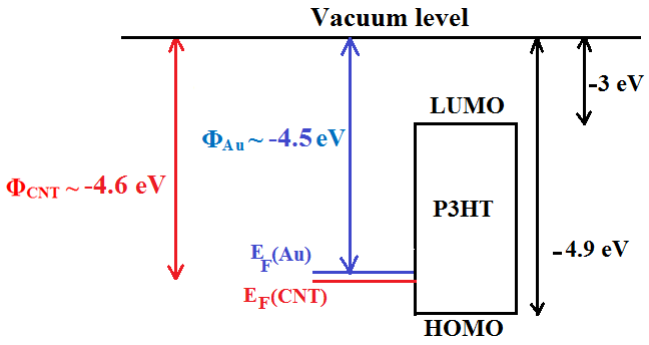

Figure 3.14: Energy levels of P3HT (HOMO and LUMO), relative to the vacuum level [30], [31] and workfunctions of SWCNT (Φ_{CNT}) [119] and Au (Φ_{Au}) [120] electrodes. E_F (Au) and E_F (CNT) are the Fermi levels of Au and SWCNT electrodes, respectively.

Figure 3.14 shows that the values -0.3 eV and -0.4 eV can be a good estimation of the hole injection barriers height from P3HT to SWCNT and Au electrodes. The close values for the barrier heights should lead to comparable injection efficiency for the two types of electrodes (SWCNT array and Au). However, the TFT characteristics show that SWCNT array electrodes provide a better injection efficiency, in comparison with Au electrodes.

The improvement of injection by SWCNT electrodes can be explained by the presence of a favorable interface between SWCNTs and P3HT due to the fact that both the two structures are

chemically conjugated. Moreover, since SWCNTs are 1D nanostructures, they can show enhanced electrostatic effects at the SWCNT/P3HT interface. Thus, the injection barrier at the contacts can be made thin enough to allow tunneling.

3.1.3 Charge transport characteristics of P3HT/PCBM blends TFTs

The effect of SWCNT array electrodes on OTFTs was later extended from unipolar organic semiconductors to ambipolar ones. Indeed OTFTs based on blends of p-type and n-type organic semiconductors, specifically P3HT and the solution-processable fullerene derivative PCBM, were prepared. The aim of this study on ambipolar OTFTs was to provide an answer to the question of whether SWCNT array electrodes are able to simultaneously improve the injection efficiency of both electrons and holes. To achieve ambipolar transistor operation, both electrons and holes have to be injected and transported in the semiconducting layer.

Ambipolarity in OTFTs can be achieved using different approaches. One approach is based on the use of two different electrodes, "two color" electrodes, having different workfunctions, in a way to enable electron injection from one electrode (low workfunction electrode) and hole injection from another electrode (high workfunction electrode). A second approach is based on the use of one electrode material in combination with two different semiconductors. In this case, a good energy level matching has to be achieved between the Fermi level of electrode with the HOMO level of one semiconductor and the LUMO level of the other [35].

In this approach, the two organic semiconductors can be arranged in a bi-layer structure or they can be co-evaporated or, as is the case for this MSc work, blended together from solution. In this last case the advantage is that the ambipolar organic semiconducting films can be easily deposited from solution [123].

Various blends have been investigated to demonstrate ambipolar OTFTs [35], [124], [125], [126], but the most investigated one is constituted of P3HT and PCBM. P3HT/PCBM blends are currently used for application in organic photovoltaics. Bulk heterojunction photovoltaic cells based on P3HT/PCBM blends have yielded about 8% power conversion efficiency [127], [128].

In the previous section, we investigated the performance of TFTs making use of SWCNT array electrodes and P3HT as the single semiconductor. The results indicated that SWCNT array electrodes are able to improve the hole injection efficiency, with respect to Au contacts.

Cicoira *et al*. investigated the performance of SWCNT array electrodes applied to PCBM TFTs on SiO_2. They obtained $\mu_e = 2\times10^{-2}$ $cm^2/V\cdot s$ and superior electron injection efficiency compared to Au contacts. An (unbalanced) ambipolarity was also achieved by vacuum annealing of OTFTs based on PCBM as a single layer semiconductor [93].

Here, we investigated the performance of P3HT/PCBM blends TFTs using SWCNT array electrodes by comparing with their Au counterparts. As previously mentioned in Chapter 2, fabrication of OTFTs based on P3HT/PCBM blend was done using three different procedures. The three procedures differ from the P3HT/PCBM ratio used to prepare the blends.

As far as the the first procedure is concerned (P3HT/PCBM with weight ratio of 1:4), because of the high contact resistance observed, no conclusive observations could not be drawn such that a new series of experiments is ongoing at present.

In the second procedure, blends of P3HT (SolarisChem) and PCBM (KinTec) with weight ratio of 1:1 were prepared using a concentration of 10 mg/mL in chlorobenzene. After spin coating, annealing at 100 ˚C was carried out for 30 mins [116] .

Typical output and transfer characteristics of TFTs using P3HT/PCBM blend with weight ratio 1:1 and Au electrodes (referred to Au P3HT/PCBM (1:1) TFTs) demonstrate both p-type and n-type behaviors (Figure 3.15). The output curve shows diode-like behavior at low V_G and a high V_D because electrons (holes) are injected in a p-type (n-type) channel at high V_D. This is a typical characteristic of ambipolar transistors, which can be observed in neither P3HT nor PCBM unipolar transistors.

The transfer curves of Au P3HT/PCBM (1:1) TFTs show a V-shape typical of ambipolar systems, with one branch indicating electron transport and the other indicating hole transport [36]. For each branch, the mobility and threshold voltage can be extracted from the slope of the linear fit of square root of I_D at saturation regime.

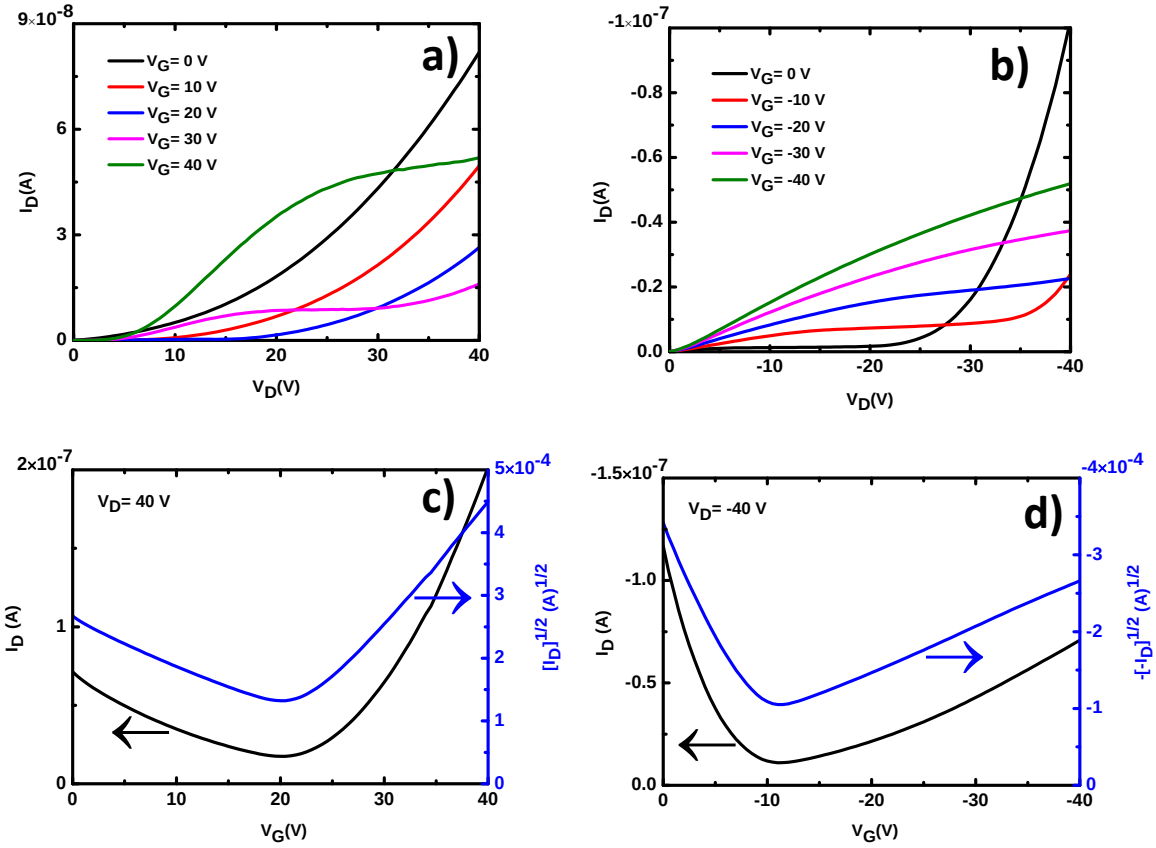

Figure 3.15: Output characteristics of Au P3HT/PCBM (1:1) TFTs for n-type a) and p-type b) behaviors. Transfer characteristics of Au P3HT/PCBM (1:1) TFTs for n-type c) and p-type d) behaviors. V_D (V_G) changes by 100 mV (W/L= 1540 µm /10 µm, 100 nm thick SiO_2).

The output and transfer characteristic of SWCNT P3HT/PCBM (1:1) TFTs (Figure 3.16) indicate an exclusive n-type behavior. Figure 3.16 (panels a and c) indicates that the OTFT is a unipolar (n-type) transistor. Its performance is identical to unipolar transistor based on PCBM as the single semiconductor. At low V_D, we observe a linear current increase, which is a typical behavior of SWCNT OTFTs exclusively based on PCBM[2] [93]. This linearity is not observed in a unipolar PCBM transistor based on Au electrodes, indicating that SWCNT electrodes are able efficiently to inject electrons. However, we do not observe any injection of holes.

[2] The fabrication of this device was not performed in this project.

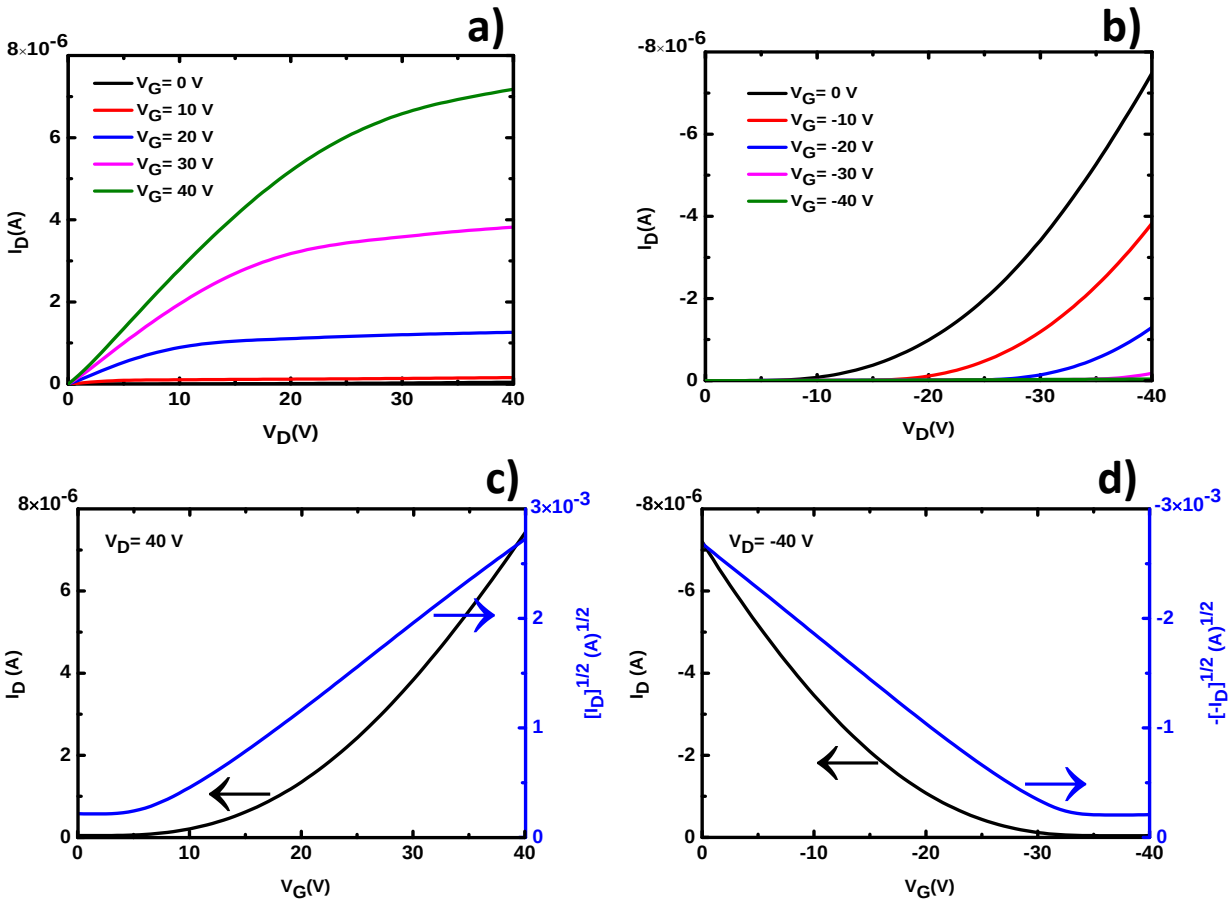

Figure 3.16: Output characteristics of SWCNT P3HT/PCBM (1:1) TFTs for n-type a) and p-type b) behaviors. Transfer characteristics of SWCNT P3HT/PCBM (1:1) TFTs for n-type c) and p-type d) behaviors. V_D (V_G) changes by ± 100 mV (W/L= 1540 µm /10 µm, 100 nm thick SiO_2).

Mobility and threshold voltage of SWCNT P3HT/PCBM (1:1) TFTs and Au P3HT/PCBM (1:1) TFTs are illustrated in Figure 3.17. In the x-axis, Au - n type and SWCNT - n type indicate the μ_e and V_{TH} calculated at V_D = 40 V (saturation regime) for Au P3HT/PCBM (1:1) TFTs, SWCNT P3HT/PCBM (1:1) TFTs, respectively. On the other hand, Au - p type and SWCNT - p type correspond to the μ_h and V_{TH} calculated at V_D = -40 V (saturation regime) for Au P3HT/PCBM (1:1) TFTs, SWCNT P3HT/PCBM (1:1) TFTs, respectively. Figure 3.17 shows the calculated values, the average value, and the standard deviation.

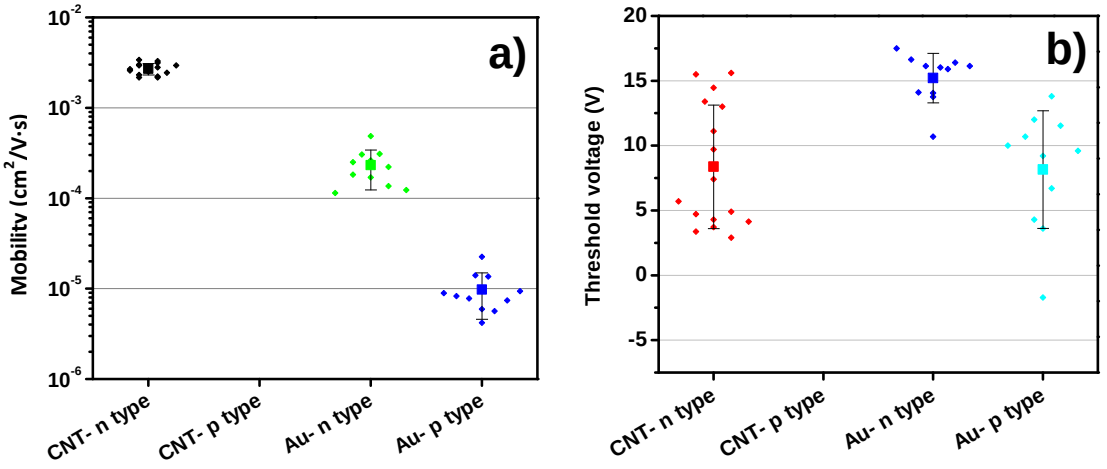

Figure 3.17. Mobility a) and threshold voltage b) of SWCNT P3HT/PCBM (1:1) TFTs and Au P3HT/PCBM (1:1) TFTs obtained at $V_D = \pm 40$ V (saturation regime). The bars denote standard deviation. L/W= 5/1555 µm/µm, L/W = 10/1540 µm/µm, L/W= 20/1510 µm/µm, L/W= 50/1413 µm/µm.

As previously mentioned, SWCNT P3HT/PCBM (1:1) TFTs do not exhibit any ambipolar behavior and μ_e of 2.7×10^{-3} $cm^2/V\cdot s$ and $V_{TH} = 8.4$ V were extracted at $V_D = 40$ V. The average value for μ_e was 2.3×10^{-4} $cm^2/V\cdot s$ and the average value for μ_h was 9.8×10^{-6} $cm^2/V\cdot s$, in Au P3HT/PCBM (1:1) TFTs, at $V_D = \pm40$ V. The average value of V_{TH} was 15.2 V and 8.1 V in Au P3HT/PCBM (1:1) TFTs for n-type and p-type operation, respectively. In Au P3HT/PCBM (1:1) TFTs, threshold voltage for holes transport is positive. This result points to the presence of holes in the transistor channel before the suitable (negative) gate bias is applied to the device. The causes determining an "open channel" in the p-type region, even in absence of negative V_G applied, are not clear and the subject is, at present, under investigation.

We observed that SWCNT P3HT/PCBM (1:1) TFTs demonstrate an exclusive n-type behavior. Therefore, to try to achieve ambipolarity in OTFTs making use of SWCNT electrodes, we changed the concentration of P3HT in the two-component solution and we fabricated OTFTs using P3HT/PCBM blends with weight ratio of 4:1, respectively. In this manner, we intended to improve p-type injection and transport in the P3HT/PCBM OTFTs.

Figure 3.18 shows the output characteristics of SWCNT P3HT/PCBM (4:1) TFTs for both p-type and n-type operation.

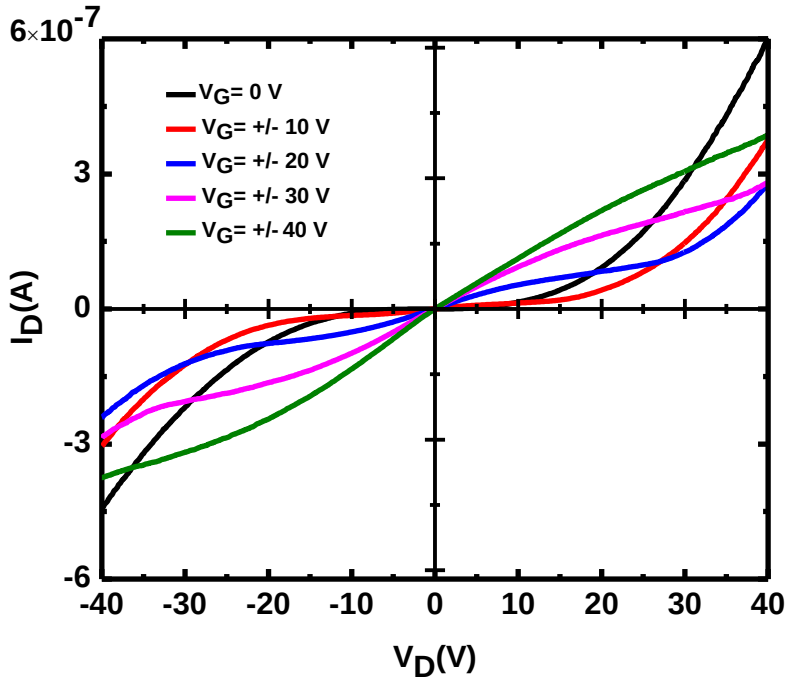

Figure 3.18: Output characteristics of SWCNT P3HT/PCBM (4:1) TFTs for p-type and n-type operations. V_D changes by ±100 mV (W/L= 1540 µm/10 µm, 200 nm thick SiO_2).

For low V_G values, diode-like curves typical of ambipolar transistors, are observed. These features occur due to the presence of both holes and electrons in the transistor channel. At high V_G, the typical behaviors of p- or n-type semiconductor appear. Furthermore, Figure 3.18 displays an excellent symmetry between p-type operation (V_D < 0 V, V_G < 0 V) and n-type operation (V_D > 0 V, V_G > 0 V). This points to the balanced transport of p- and n-type in the transistor channel. The transfer characteristics of SWCNT P3HT/PCBM (4:1) TFTs are illustrated in Figure 3.19. These curves also reveal an ambipolar behavior.

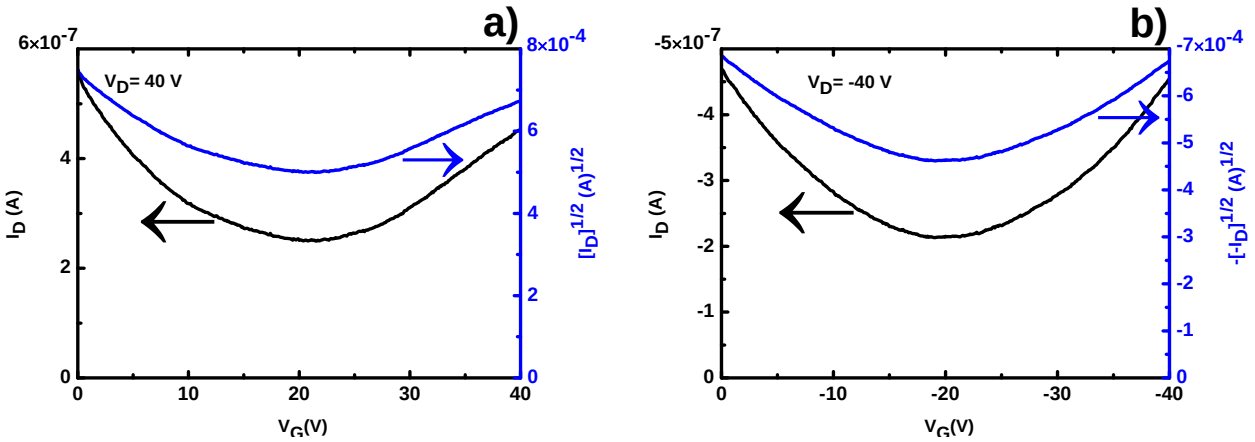

Figure 3.19: Transfer characteristics of SWCNT P3HT/PCBM (4:1) TFTs for n-type a) and p-type b) behavior. V_G changes by ±100 mV (W/L= 1540 µm/10 µm, 200 nm thick SiO_2).

The output characteristics of Au P3HT/PCBM (4:1) TFTs are illustrated in Figure 3.20. For low V_D, the performance of Au P3HT/PCBM (4:1) TFTs in the p-type region is similar to that of a unipolar transistor based on P3HT as single semiconductor. On the other hand, for high values of V_D and V_G = 0, we have an increase of I_D with increasingly negative V_D. This result indicates that this TFT shows an unbalanced ambipolar behavior.

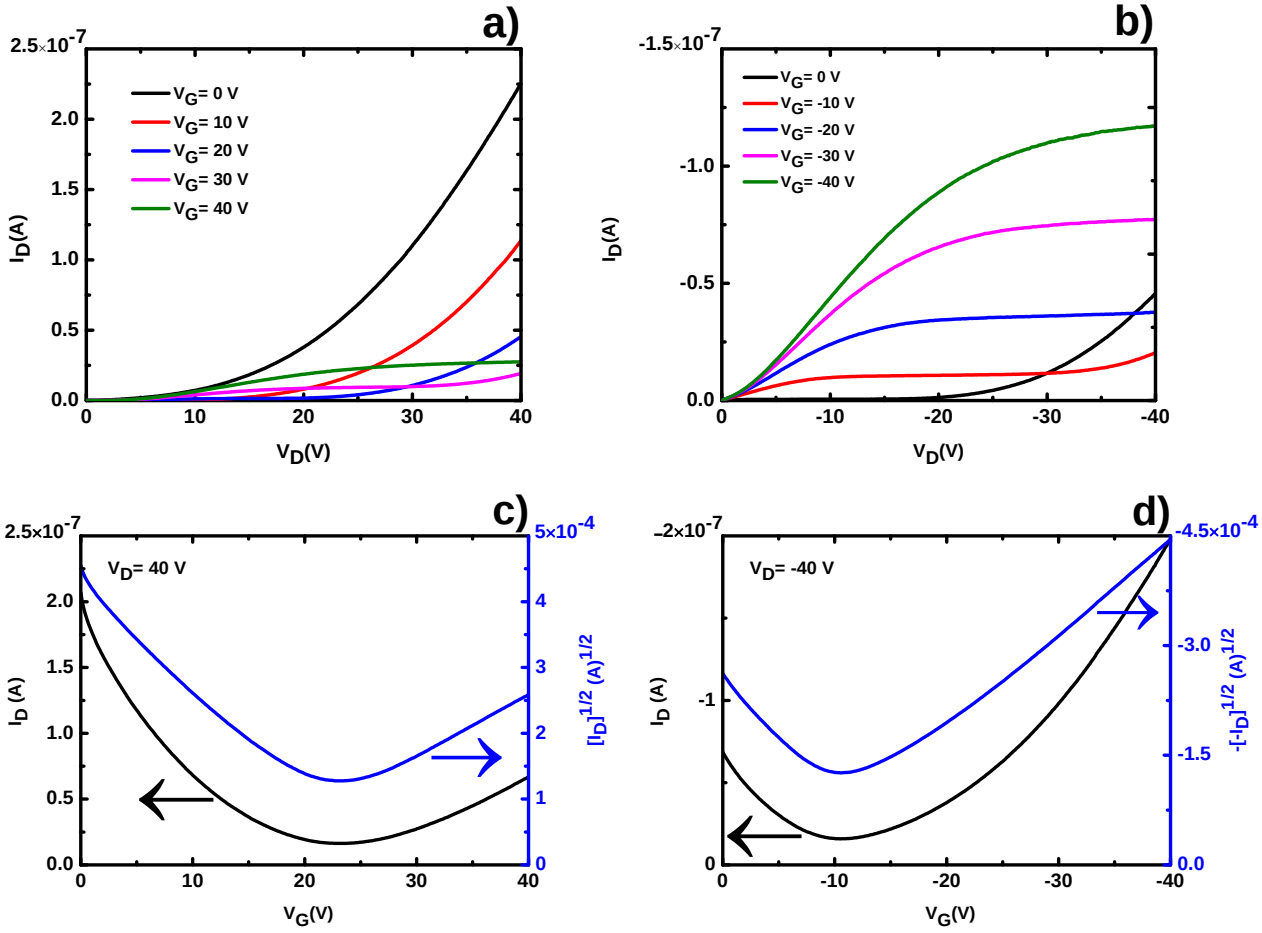

Figure 3.20 : Output characteristics of Au P3HT/PCBM (4:1) TFTs for n-type a) and p-type b) behaviors. Transfer characteristics of Au P3HT/PCBM (4:1) TFTs for n-type c) and p-type d) behaviors. V_D (V_G) changes by ± 100 mV (W/L= 1540 µm /10 µm, 100 nm thick SiO_2).

Since the square root of I_D versus V_G in Au P3HT/PCBM (4:1) TFTs and SWCNT P3HT/PCBM (4:1) TFTs for each branch of the transfer curves showed a linear behavior, it was possible to extract the mobility and threshold voltage based on Equation 2-2. Mobility and threshold voltage of SWCNT P3HT/PCBM (4:1) TFTs and Au P3HT/PCBM (4:1) TFTs are illustrated in Figure 3.21.

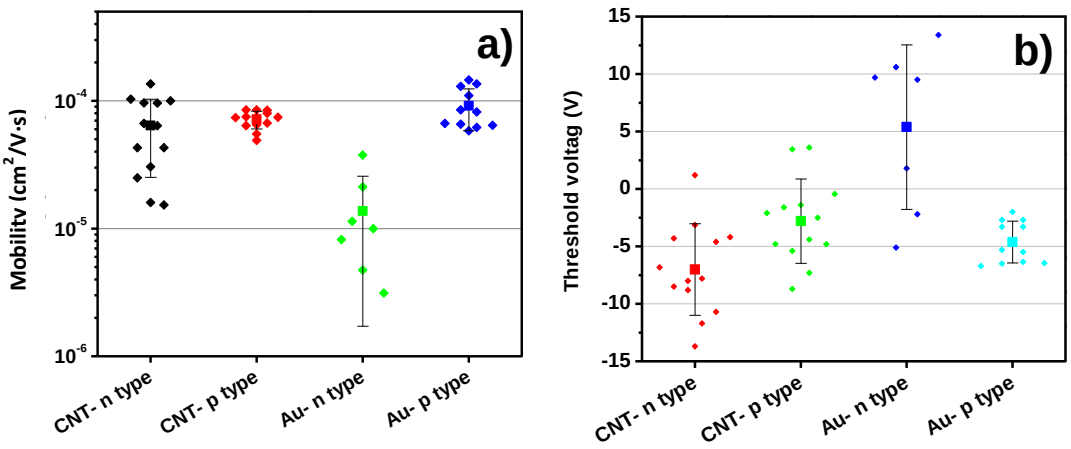

Figure 3.21: Mobility a) and threshold voltage b) of SWCNT P3HT/PCBM (4:1) TFTs and Au P3HT/PCBM (4:1) TFTs at V_D = ± 40 V. The error bars denote the standard deviation. L/W= 5/1555 µm/µm, L/W = 10/1540 µm/µm, L/W= 20/1510 µm/µm, L/W= 50/1413 µm/µm.

The average values μ_e= 6.4×10^{-5} $cm^2/V\cdot s$ and μ_h= 7.2×10^{-5} $cm^2/V\cdot s$ were found for SWCNT P3HT/PCBM (4:1) TFTs. For Au P3HT/PCBM (4:1) TFTs, μ_e of 1.4×10^{-5} $cm^2/V\cdot s$ and μ_h of about 9.1×10^{-5} $cm^2/V\cdot s$ were calculated.

For n-type operation, the average value of V_{TH} was 5.4 V and -7 in Au P3HT/PCBM (4:1) TFTs and SWCNT P3HT/PCBM (4:1) TFTs, respectively. For n-type operation, the threshold voltage in SWCNT P3HT/PCBM (4:1) TFTs is negative. This result points to the presence of electrons in the transistor channel before the suitable (positive) gate bias is applied to the device. The causes determining an "open channel" in the n-type region, even in absence of positive V_G applied, are not clear and the subject is, at present, under investigation. For p-type operation, the average values of V_{TH} were found to be -4.6 V and -2.8 V in Au P3HT/PCBM (4:1) TFTs and SWCNT P3HT/PCBM (4:1) TFTs, respectively.

To study the injection performance, the low voltage characteristics are needed. Figure 3.22 shows the output characteristics of Au P3HT/PCBM (4:1) TFTs and SWCNT P3HT/PCBM (4:1) TFTs for both n-type and p-type operation in the range 0 V ≤ V_D ≤ ± 5 V. The output curves show a quasi linear behavior in SWCNT P3HT/PCBM (4:1) TFTs for both types of operation whereas a sublinear behavior is shown by Au P3HT/PCBM (4:1) TFTs.

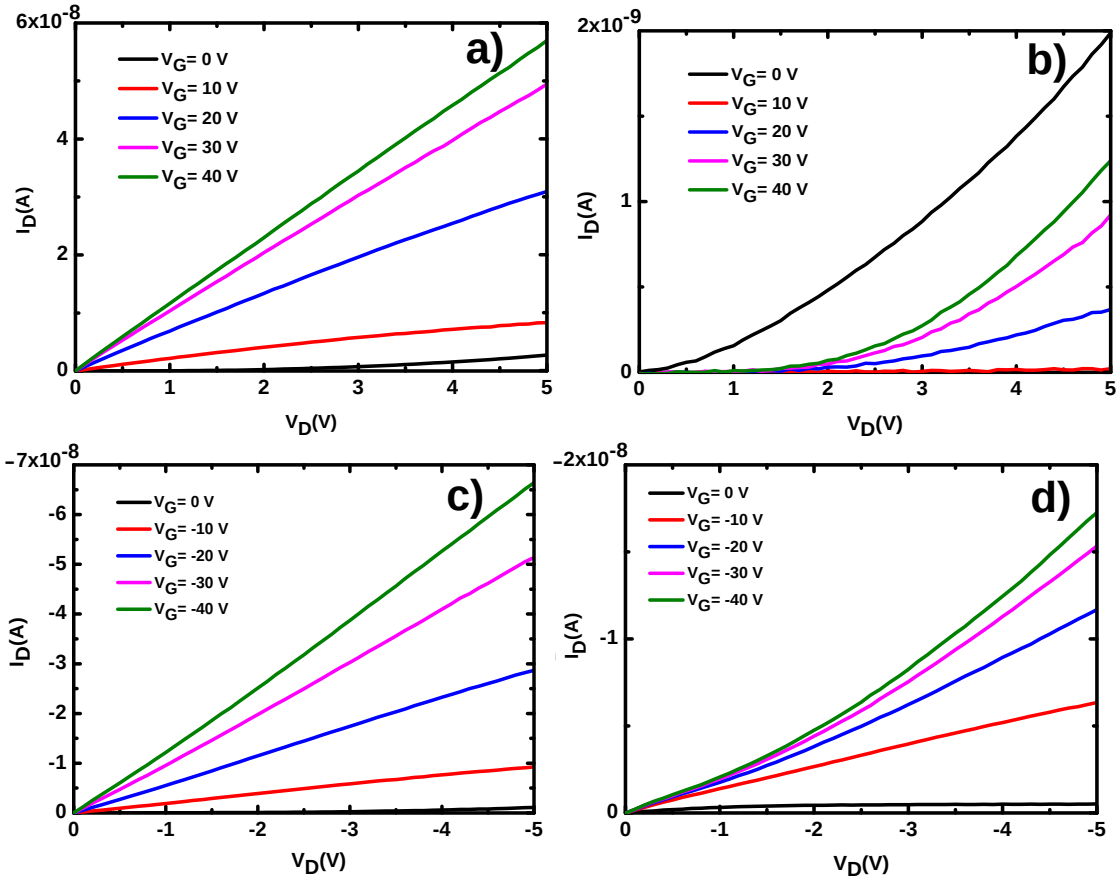

Figure 3.22: Output characteristics (n-type operation) for $0 \leq V_D \leq 5$ of SWCNT P3HT/PCBM (4:1) TFTs a) and Au P3HT/PCBM (4:1) TFTs b). Output characteristics (p-type operation) for $0 \leq V_D \leq -5$ of SWCNT P3HT/PCBM (4:1) TFTs c) and Au P3HT/PCBM (4:1) TFTs d). V_D changes by ±100 mV (W/L= 1540 µm/10 µm, 100 nm thick SiO_2).

At V_D = 1 V, and V_G = 40 V, $I_D \sim 1\times10^{-8}$ A in SWCNT P3HT/PCBM (4:1) TFTs and $I_D \sim 1\times10^{-11}$ A in Au P3HT/PCBM (4:1) TFTs. As a consequence we can say that the electron injection efficiency of SWCNT P3HT/PCBM (4:1) TFTs is three orders of magnitude higher than that of Au P3HT/PCBM (4:1) TFTs. On the other hand, SWCNT P3HT/PCBM (4:1) TFTs present 4 times higher hole injection efficiency than Au P3HT/PCBM (4:1) TFTs, considering that at V_D= -1 V, and V_G= -40 V, $I_D \sim -1\times10^{-8}$ A and $I_D \sim -0.25\times10^{-8}$ A were measured for SWCNT P3HT/PCBM (4:1) TFTs and Au P3HT/PCBM (4:1) TFTs.

It is worth noting that the values for I_D in SWCNT P3HT/PCBM (4:1) TFTs for both n-type and p-type regions are similar whereas for Au P3HT/PCBM (4:1) TFTs, there is an order of magnitude difference between I_D in the n- and in the p-type regions.

The quasi linear behavior in both n-type and p-type characteristics of SWCNT P3HT/PCBM (4:1) TFTs reveal good injection efficiency. At the same time, the sublinear behavior in Au P3HT/PCBM (4:1) TFTs indicates that the electron and hole injections are limited by the presence of injection barriers.

Using an energy diagram where the HOMO/LUMO levels of PCBM, the HOMO/LUMO levels of P3HT are represented together with the workfunction of Au and SWCNT array electrodes, we can estimate the electron and hole injection barriers (Figure 3.23).

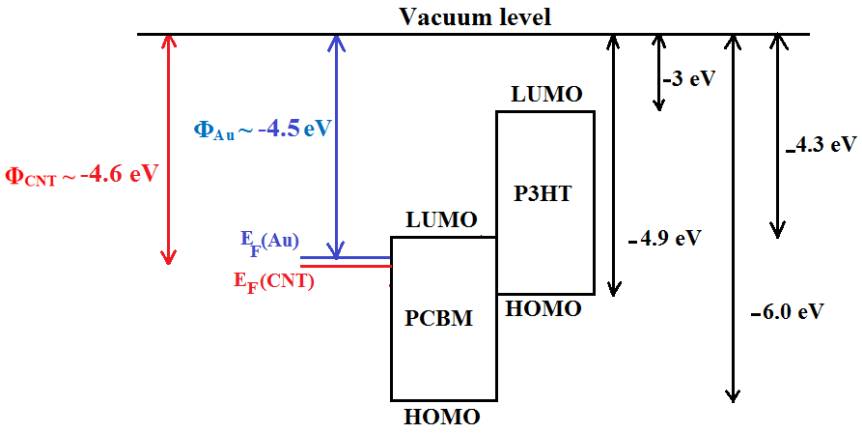

Figure 3.23: Energy levels of P3HT (HOMO and LUMO) [30], [31] and PCBM (HOMO and LUMO) [34][35], relative to the vacuum level and workfunctions of SWCNT (Φ_{CNT}) [119] and Au (Φ_{Au}) [120] electrodes. E_F (Au) and E_F (CNT) are the Fermi levels of Au and SWCNT electrodes, respectively.

As shown in Figure 3.23, the PCBM LUMO level is located at about -4.3 eV [34]. As a consequence, - 0.3 eV and - 0.2 eV can be a good estimation for the electron injection barriers from SWCNT array and Au electrodes, respectively. Despite the closely similar electron injection

barriers, the electron injection efficiency of SWCNT P3HT/PCBM (4:1) TFTs is three orders of magnitude higher than that of Au P3HT/PCBM (4:1) TFTs.

In the other hand, the differences between the Fermi levels of the electrodes and P3HT HOMO level estimate -0.3 eV and -0.4 eV for the hole injection barriers heights from SWCNT array and Au electrodes, respectively.

It is worth to note that the estimation about injection barriers is in consistent with the observation in Figure 3.22. In Au P3HT/PCBM (4:1) TFTs, the electron current is about an order of magnitude larger than the hole currents which is in agreement with the estimations about the holes and electrons barriers. Both the electron and holes currents of SWCNT P3HT/PCBM (4:1) TFTs are the same values at V_G= ±40 V, thus supporting the same injection barrier height for both electrons and holes.

The origin of the improved injection performance of SWCNT electrodes remains unclear and the results do not indicate the underlying injection mechanisms.

The large electrons and holes injection barriers expected at the interface of SWCNT and Au electrodes with P3HT/PCBM blends should lead to poor (non linear) output characteristics for both electrons and holes injection. However, SWCNT electrodes provided a quasi linear behavior for both electrons and holes injection that can indicate the presence of electrically transparent barriers. This observation provides further evidence that the charge carriers can tunnel through the barriers at the SWCNT/P3HT/PCBM (4:1) blends interface.

In other words, the enhancement of the applied electric field at the interface of SWCNT electrodes and P3HT/PCBM (4:1) can creates the sharp bending of the energy levels (i.e. reduction of barrier width) at the contacts and in turn can increase the probability of tunneling injection. Because the probability of tunneling injection depends on the width of the injection barriers.

Regarding the results obtained in SWCNT P3HT/PCBM (1:1) TFTs and Au P3HT/PCBM (1:1) TFTs, we were not able to compare the electron and hole injection mechanism of both devices since the ambipolarity behavior was not obtained in SWCNT P3HT/PCBM (1:1) TFTs. At present we do not have a definitive explanation for this observation and it needs more studying

and experiments. But this can indicate that the relative concentration (phase separation) of the components in blends plays a key role in transistor behavior.

CHAPTER 4 CONCLUSIONS AND PERSPECTIVES

Organic thin film transistors (OTFTs) are among the most interesting organic electronics devices for application in flexible plastic electronics. One of the present limitations of OTFTs is low charge injection efficiency, due to the presence of Schottky barrier at the electrode/organic semiconductor interface. To overcome this limitation several research groups are proposing the use of carbon nanotubes (CNTs) as electrode materials in organic electronic devices.

Along this line in this MSc work, we investigated the performance of single-walled carbon nanotube (SWCNT) array electrodes in OTFTs using three different organic semiconductors, namely: the small molecule titanyl-phthalocyanine (TiOPc), deposited by supersonic molecular beam epitaxy (SuMBE), the polymer poly-3 (hexylthiophene) (P3HT) and P3HT/ phenyl-C61-butyric acid methyl ester (PCBM) blends, deposited by spin coating. We systematically compared OTFTs using SWCNT array electrodes with analogues OTFTs based on conventional Au electrodes. Au has been chosen as benchmark material since it is used as electrode material in most OTFTs. This *comparative* approach is meant to ensure the "disentanglement" of the effect of SWCNT array electrodes on the OTFT characteristics from other effects related to e.g. organic semiconductor chemical quality and processing.

We have shown that SWCNT array electrodes, compared to Au electrodes, lead to improved injection characteristics in OTFTs based on TiOPc thin films (both deposited at room temperature (RT) and high temperature) in comparison with analogues devices made with Au electrodes. For OTFTs using SWCNT array electrodes the source/drain current in the linear regime was typically 50-100 times higher than that of OTFTs using Au electrodes. We observed nonlinear output characteristics for TiOPc OTFTs using Au electrodes at low voltage (both for films deposited at RT and high T), which clearly indicates the presence of a Schottky barrier. On the other hand, the quasi linear output characteristics observed in SWCNT RT TiOPc TFTs and SWCNT HT TiOPc TFTs at low drain voltages and the relative values of I_D obtained at low voltages for SWCNT array vs. Au based TFTs indicate the presence of quasi transparent injection barriers in the case of TFTs based on SWCNT array electrodes.

These results demonstrated that using SWCNT array electrodes would improve injection efficiency in TiOPc TFTs. We propose that field enhancement may be taking place at SWCNT/TiOPc interface enabling better injection. We also make the hypothesis that SWCNT

array electrodes are able to provide favorable interface with TiOPc due to the π-π bonding between the SWCNTs and TiOPc. In addition to improvement of charge carrier injection in SWCNT HT TiOPc TFTs (SWCNT RT TiOPc TFTs), the SWCNT array electrodes led to high charge carrier mobility. The highest hole mobility of 1.2×10^{-3} $cm^2/V\cdot s$ were observed in SWCNT HT TiOPc TFTs.

By comparing the results of SWCNT HT TiOPc TFTs (Au HT TiOPc TFTs) and SWCNT RT TiOPc TFTs (Au RT TiOPc TFTs), we can conclude that the effect of temperature during deposition of TiOPc is more pronounced in TFTs making use of SWCNT array electrodes vs. Au electrodes, although the temperature effect is not dramatic. This can be attributed to the stronger π-π bonding between the SWCNTs and TiOPc in high temperature in comparison with that in room temperature.

We have subsequently shown the improvement of injection efficiency in P3HT TFTs using SWCNT array electrodes. We also performed a few preliminary experiments in P3HT TFTs where SiO_2 was pre-treated with self assembled monolayers (SAMs) of hexamethyldisilazane (HMDS) and octadecylthrichlorosilane (OTS) improving the wettability of the substrate surface. In all cases, SWCNT array electrodes provided higher injection efficiency and hole mobility in comparison with benchmark Au P3HT TFTs. We showed that even with the presence of HMDS and OTS on SWCNT array electrodes, an improvement of injection was observed with respect to Au electrodes. The improvement of injection by SWCNT electrodes can be explained by the presence of a favorable interface between SWCNTs and P3HT due to the fact that both the two structures are chemically conjugated. Moreover, since SWCNTs are one dimensional (1D) nanostructures, they can show enhanced electrostatic effects at the SWCNT/P3HT interface. Thus, the injection barrier at the contacts can be made thin enough to allow tunneling.

The effect of SWCNT array electrodes on OTFTs was later extended from unipolar organic semiconductors to ambipolar ones, P3HT/PCBM blends. P3HT/PCBM blends are an important example of bulk-heterojunction systems where two (p- and n-type) organic semiconductors are mixed at the molecular/nanometric level. The aim of this study on ambipolar OTFTs was to provide an answer to the question of whether SWCNT array electrodes are able to simultaneously improve the injection efficiency of both electrons and holes.

We showed that with the presence of the large electrons and holes injection barriers expected at the interface of SWCNT with P3HT/PCBM blends, SWCNT array electrodes provided a quasi linear behavior for both electrons and holes injection indicating the electrically transparent barriers. This observation provides further evidence that the charge carriers can tunnel through the barriers at the SWCNT/P3HT/PCBM (4:1) blends interface. Thus, indeed SWCNT array electrodes are able to improve hole and electron injection in ambipolar devices. Our study paves the way for use of SWCNT array electrodes in devices such as organic light emitting transistors (OLETs), where ambipolar injection is highly desired.

However, during performing this project some unexpected results was observed using different weight ratio of P3HT/PCBM blends. We showed that SWCNT P3HT/PCBM (1:1) TFTs acted as unipolar (n-type) TFT while Au P3HT/PCBM (1:1) TFTs acted as ambipolar TFTs. The explanation of this behavior is complicated and needs further investigation since we mixed two complex systems together: P3HT/PCBM blends and SWCNT array electrodes. However our work indicates that the relative concentration (phase separation) of the components in blends plays a key role in determining transistor behavior.

In summary SWCNT array electrodes, compared to Au electrodes, led to an improvement of the charge carrier injection efficiency in OTFTs based on different organic semiconductors, belonging to different classes of materials (e.g., polymers and small molecules) and differently processed (e.g. solution processed and vacuum processed).

The results suggest the general validity of the approach based on SWCNT array electrodes for the improvement of injection efficiency in OTFTs. The underlying hypotheses for this approach were that 1D structure of CNTs facilitates charge carrier injection by field emission and the conjugated structure that CNTs and organic semiconductors have in common provides a favorable electrode/organic semiconductor interface, with low density of charge carrier traps. We explained our results based on these two hypotheses. However, the injection mechanism for SWCNT array electrodes has not been definitively identified by our results and it is at present under investigation.

There are a number of possible developments for this MSc work. We name a few in what follows:

1) To understand the injection mechanism from SWCNT array electrodes to organic semiconductors in OTFTs, it can be helpful to measure the transistor current as a function of the temperature. In this way, we can distinguish different mechanisms i.e. thermionic emission and tunneling mechanism since they have a different dependence on temperature and applied electrical bias.

2) Fabrication of OTFTs using graphene (single layer of graphite) electrodes: graphene, a honeycomb lattice made of carbon atoms, is a two dimensional material. This experiment should provide a conclusive answer to the question whether the 1D structure of SWCNT electrodes is the main explanation for the charge carrier injection efficiency improvement in SWCNT array electrode-based OTFTs compared to their Au analogues.

3) Since different TFT performances were obtained for the SWCNT array and Au cases, in OTFTs based on SWCNT array and Au as the electrodes and P3HT/PCBM blends, at different weight ratios, as the semiconductor, it could be interesting to carry out a systematic study on the effect of the weight ratio on the performance of TFTs using SWCNT array electrodes, to investigate the specificity of the π-π interactions between organic semiconductors and SWCNTs.

4) Fabrication of organic light emitting transistors based on SWCNT array electrodes. In such devices, the injection of both electrons and holes is required in order to form excitons whose radiative recombination leads to light emission. SWCNT array electrodes, improving the injection of both holes and electrons, could lead to an improvement in the performance of such devices in terms of light intensity and light emission efficiency. For the fabrication of these devices, an interdigitated pattern is required in order to maximize the intensity of the emitted light (to achieve easier light detection).

The removal of SWCNTs from the channel in interdigitated patterns can be done using photolithography alignment of photoresist (that would be the mask for the subsequent step) followed by oxygen plasma exposure. In this manner, we could achieve an improved control over the amount of SWCNTs in the channel. Indeed the procedure based on the removal of SWCNTs by sonication used to obtain single channel devices suffers from a limited control on the degree of SWCNT removal.

REFERENCES

[1] C. Wöll, *Organic electronics: structural and electronic properties of OFETs*. Wiley-VCH Verlag, 2009.

[2] A. Tsumura, H. Koezuka, and T. Ando, "Polythiophene field-effect transistor: Its characteristics and operation mechanism," *Synthetic Metals*, vol. 25, no. 1, pp. 11–23, 1988.

[3] C. W. Tang and S. A. VanSlyke, "Organic electroluminescent diodes," *Applied Physics Letters*, vol. 51, no. 12, p. 913, 1987.

[4] J. H. Burroughes, D. D. C. Bradley, A. R. Brown, R. N. Marks, K. Mackay, R. H. Friend, P. L. Burns, and A. B. Holmes, "Light-emitting diodes based on conjugated polymers," *Nature*, vol. 347, no. 6293, pp. 539–541, 1990.

[5] "Kodak and Heraeus co-developed a cost-effective ITO alternative." [Online]. Available: http://www.oled-info.com/tags/companies/kodak. [Accessed: 27-Jan-2012].

[6] "Lumiblade OLED more than just another light source." [Online]. Available: http://www.lighting.philips.com/main/lightcommunity/trends/oled/index.wpd. [Accessed: 27-Jan-2012].

[7] C. W. Tang, "Two-layer organic photovoltaic cell," *Applied Physics Letters*, vol. 48, no. 2, pp. 183–185, 1986.

[8] G. Dennler, M. C. Scharber, and C. J. Brabec, "Polymer-Fullerene Bulk-Heterojunction Solar Cells," *Advanced Materials*, vol. 21, no. 13, pp. 1323–1338, 2009.

[9] K. P. Goetz, Z. Li, J. W. Ward, C. Bougher, J. Rivnay, J. Smith, B. R. Conrad, S. R. Parkin, T. D. Anthopoulos, A. Salleo, J. E. Anthony, and O. D. Jurchescu, "Effect of Acene Length on Electronic Properties in 5-, 6-, and 7-Ringed Heteroacenes," *Advanced Materials*, vol. 23, no. 32, pp. 3698–3703, 2011.

[10] S. R. Forrest, "The path to ubiquitous and low-cost organic electronic appliances on plastic," *Nature*, vol. 428, no. 6986, pp. 911–918, 2004.

[11] T. Sekitani, U. Zschieschang, H. Klauk, and T. Someya, "Flexible organic transistors and circuits with extreme bending stability," *Nature Materials*, vol. 9, no. 12, pp. 1015–1022, 2010.

[12] D. J. Gundlach, "Organic electronics: Low power, high impact," *Nature Materials*, vol. 6, no. 3, pp. 173–174, 2007.

[13] H. Klauk, "Organic thin-film transistors," *Chemical Society Reviews*, vol. 39, no. 7, pp. 2643–2666, 2010.

[14] X. Zhang, *Device engineering of organic field-effect transistors toward complementary circuits*. Georgia Institute of Technology, 2009.

[15] E. A. Silinish and V. Capek, *Organic molecular crystals: interaction, localization, and transport phenomena*. American Institute of Physics, 1994.

[16] I. Kymissis, *Organic Field Effect Transistors: Theory, Fabrication and Characterization*. Springer, 2009.

[17] F. Li, A. Nathan, Y. Wu, and B. S. Ong, *Organic Thin Film Transistor Integration: A Hybrid Approach*. John Wiley & Sons, 2011.

[18] W. Bruetting, *Physics of Organic Semiconductors*. John Wiley & Sons, 2006.

[19] A. A. Virkar, S. Mannsfeld, Z. Bao, and N. Stingelin, "Organic Semiconductor Growth and Morphology Considerations for Organic Thin-Film Transistors," *Advanced Materials*, vol. 22, no. 34, pp. 3857–3875, 2010.

[20] F. Cicoira, C. Santato, F. Dinelli, M. Murgia, M. A. Loi, F. Biscarini, R. Zamboni, P. Heremans, and M. Muccini, "Morphology and Field-Effect-Transistor Mobility in Tetracene Thin Films," *Advanced Functional Materials*, vol. 15, no. 3, pp. 375–380, 2005.

[21] G. Horowitz, "Organic Field-Effect Transistors," *Advanced Materials*, vol. 10, no. 5, pp. 365–377, 1998.

[22] I. G. Korodi, D. Lehmann, T. Tippo, M. Hietschold, and D. R. T. Zahn, "Characterisation of organic field-effect transistors using metal phthalocyanines as active layers," *physica status solidi (c)*, vol. 7, no. 2, pp. 456–459, 2010.

[23] J.-F. Li, S.-H. Su, K.-S. Hwang, and M. Yokoyama, "Enhancing the contrast and power efficiency of organic light-emitting diodes using CuPc/TiOPc as an anti-reflection layer," *Journal of Physics D: Applied Physics*, vol. 40, no. 8, pp. 2435–2439, 2007.

[24] H. Tada, H. Touda, M. Takada, and K. Matsushige, "Quasi-intrinsic semiconducting state of titanyl-phthalocyanine films obtained under ultrahigh vacuum conditions," *Applied Physics Letters*, vol. 76, no. 7, pp. 873–875, 2000.

[25] Q. Tang, H. Li, X. Yang, W. Hu, Y. Song, Z. Shuai, W. Xu, Y. Liu, and D. Zhu, "An Ultra Closely π-Stacked Organic Semiconductor for High Performance Field-Effect Transistors," *Advanced Materials*, vol. 19, no. 18, pp. 2613–2617, 2007.

[26] Z. Bao, A. Dodabalapur, and A. J. Lovinger, "Soluble and processable regioregular poly(3-hexylthiophene) for thin film field-effect transistor applications with high mobility," *Applied Physics Letters*, vol. 69, no. 26, pp. 4108–4110, 1996.

[27] R. J. Kline, M. D. McGehee, E. N. Kadnikova, J. Liu, J. M. J. Fréchet, and M. F. Toney, "Dependence of Regioregular Poly(3-hexylthiophene) Film Morphology and Field-Effect Mobility on Molecular Weight," *Macromolecules*, vol. 38, no. 8, pp. 3312–3319, 2005.

[28] H. Yan, Z. Chen, Y. Zheng, C. Newman, J. R. Quinn, F. Dotz, M. Kastler, and A. Facchetti, "A high-mobility electron-transporting polymer for printed transistors," *Nature*, vol. 457, no. 7230, pp. 679–686, 2009.

[29] A. Assadi, C. Svensson, M. Willander, and O. Inganas, "Field-effect mobility of poly(3-hexylthiophene)," *Applied Physics Letters*, vol. 53, no. 3, pp. 195–197, 1988.

[30] J. Hou, Z. Tan, Y. Yan, Y. He, C. Yang, and Y. Li, "Synthesis and Photovoltaic Properties of Two-Dimensional Conjugated Polythiophenes with Bi(thienylenevinylene) Side Chains," *Journal of the American Chemical Society*, vol. 128, no. 14, pp. 4911–4916, 2006.

[31] M. Onoda, K. Tada, A. A. Zakhidov, and K. Yoshino, "Photoinduced charge separation in photovoltaic cell with heterojunction of p- and n-type conjugated polymers," *Thin Solid Films*, vol. 331, no. 1–2, pp. 76–81, 1998.

[32] H. Sirringhaus, P. J. Brown, R. H. Friend, M. M. Nielsen, K. Bechgaard, B. M. W. Langeveld-Voss, A. J. H. Spiering, R. A. J. Janssen, E. W. Meijer, P. Herwig, and D. M. de Leeuw, "Two-dimensional charge transport in self-organized, high-mobility conjugated polymers," *Nature*, vol. 401, no. 6754, pp. 685–688, 1999.

[33] M. Chikamatsu, A. Itakura, Y. Yoshida, R. Azumi, and K. Yase, "High-Performance n-Type Organic Thin-Film Transistors Based on Solution-Processable Perfluoroalkyl-Substituted C60 Derivatives," *Chemistry of Materials*, vol. 20, no. 24, pp. 7365–7367, 2008.

[34] R. Kroon, M. Lenes, J. C. Hummelen, P. W. M. Blom, and B. de Boer, "Small Bandgap Polymers for Organic Solar Cells (Polymer Material Development in the Last 5 Years)," *Polymer Reviews*, vol. 48, no. 3, pp. 531–582, 2008.

[35] E. J. Meijer, D. M. de Leeuw, S. Setayesh, E. van Veenendaal, B.-H. Huisman, P. W. M. Blom, J. C. Hummelen, U. Scherf, and T. M. Klapwijk, "Solution-processed ambipolar organic field-effect transistors and inverters," *Nature Materials*, vol. 2, no. 10, pp. 678–682, 2003.

[36] J. Zaumseil and H. Sirringhaus, "Electron and Ambipolar Transport in Organic Field-Effect Transistors," *Chemical Reviews.*, vol. 107, no. 4, pp. 1296–1323, 2007.

[37] C. R. Newman, R. J. Chesterfield, M. J. Panzer, and C. D. Frisbie, "High mobility top-gated pentacene thin-film transistors," *Journal of Applied Physics*, vol. 98, no. 8, p. 084506, 2005.

[38] C. H. Lei, A. Das, M. Elliott, J. E. Macdonald, and M. L. Turner, "Au-poly(3-hexylthiophene) contact behaviour at high resolution," *Synthetic Metals*, vol. 145, no. 2–3, pp. 217–220, 2004.

[39] Y. Roichman and N. Tessler, "Structures of polymer field-effect transistor: Experimental and numerical analyses," *Applied Physics Letters*, vol. 80, no. 1, pp. 151–153, 2002.

[40] C. D. Dimitrakopoulos and P. R. L. Malenfant, "Organic Thin Film Transistors for Large Area Electronics," *Advanced Materials*, vol. 14, no. 2, pp. 99–117, 2002.

[41] Y. Shen, A. R. Hosseini, M. H. Wong, and G. G. Malliaras, "How To Make Ohmic Contacts to Organic Semiconductors," *ChemPhysChem*, vol. 5, no. 1, pp. 16–25, 2004.

[42] M. J. Panzer and C. D. Frisbie, "Contact Effects in Organic Field-Effect Transistors," in *Organic field-effect transistors*, CRC Press, 2007.

[43] S. M. Sze and K. K. Ng, *Physics of semiconductor devices*. Wiley-Interscience, 2007.

[44] A. Kahn, N. Koch, and W. Gao, "Electronic structure and electrical properties of interfaces between metals and π-conjugated molecular films," *Journal of Polymer Science Part B: Polymer Physics*, vol. 41, no. 21, pp. 2529–2548, 2003.

[45] J. Hölzl, F. K. Schulte, and H. Wagner, *Solid surface physics*. Springer-Verlag, 1979.

[46] I. G. Hill, A. Rajagopal, A. Kahn, and Y. Hu, "Molecular level alignment at organic semiconductor-metal interfaces," *Applied Physics Letters*, vol. 73, no. 5, pp. 662–664, 1998.

[47] E. H. Rhoderick and R. H. Williams, *Metal-semiconductor contacts*. Clarendon Press, 1988.

[48] P. P. Stallinga, *Electrical Characterization of Organic Electronic Materials and Devices*, 1st ed. Wiley, 2009.

[49] J. C. Scott, "Metal–organic interface and charge injection in organic electronic devices," *Journal of Vacuum Science & Technology A: Vacuum, Surfaces, and Films*, vol. 21, no. 3, p. 521, 2003.

[50] R. Schroeder, L. A. Majewski, and M. Grell, "Improving organic transistor performance with Schottky contacts," *Applied Physics Letters*, vol. 84, no. 6, pp. 1004–1006, 2004.

[51] Y. Tsuruma, A. Al-Mahboob, S. Ikeda, J. T. Sadowski, G. Yoshikawa, Y. Fujikawa, T. Sakurai, and K. Saiki, "Real-Time Observation and Control of Pentacene Film Growth on an Artificially Structured Substrate," *Advanced Materials*, vol. 21, no. 48, pp. 4996–5000, 2009.

[52] S. D. Wang, T. Minari, T. Miyadera, K. Tsukagoshi, and Y. Aoyagi, "Contact-metal dependent current injection in pentacene thin-film transistors," *Applied Physics Letters*, vol. 91, no. 20, p. 203508, 2007.

[53] I. G. Hill and A. Kahn, "Interface electronic properties of organic molecular semiconductors," *Proceedings of SPIE*, vol. 3476, no. 1, pp. 168–177, 1998.

[54] K. Walzer, B. Maennig, M. Pfeiffer, and K. Leo, "Highly Efficient Organic Devices Based on Electrically Doped Transport Layers," *Chemical Reviews*, vol. 107, no. 4, pp. 1233–1271, 2007.

[55] I. H. Campbell, J. D. Kress, R. L. Martin, D. L. Smith, N. N. Barashkov, and J. P. Ferraris, "Controlling charge injection in organic electronic devices using self-assembled monolayers," *Applied Physics Letters*, vol. 71, no. 24, pp. 3528–3530, 1997.

[56] X. Zhou, M. Pfeiffer, J. Blochwitz, A. Werner, A. Nollau, T. Fritz, and K. Leo, "Very-low-operating-voltage organic light-emitting diodes using a p-doped amorphous hole injection layer," *Applied Physics Letters*, vol. 78, no. 4, pp. 410–412, 2001.

[57] P. Stoliar, R. Kshirsagar, M. Massi, P. Annibale, C. Albonetti, D. M. de Leeuw, and F. Biscarini, "Charge Injection Across Self-Assembly Monolayers in Organic Field-Effect Transistors: Odd−Even Effects," *Journal of the American Chemical Society*, vol. 129, no. 20, pp. 6477–6484, 2007.

[58] P. Marmont, N. Battaglini, P. Lang, G. Horowitz, J. Hwang, A. Kahn, C. Amato, and P. Calas, "Improving charge injection in organic thin-film transistors with thiol-based self-assembled monolayers," *Organic Electronics*, vol. 9, no. 4, pp. 419–424, 2008.

[59] Q. J. Cai, M. B. Chan-Park, Q. Zhou, Z. S. Lu, C. M. Li, and B. S. Ong, "Self-assembled monolayers mediated charge injection for high performance bottom-contact poly(3,3‴-didodecylquaterthiophene) thin-film transistors," *Organic Electronics*, vol. 9, no. 6, pp. 936–943, 2008.

[60] K. Asadi, Y. Wu, F. Gholamrezaie, P. Rudolf, and P. W. M. Blom, "Single-Layer Pentacene Field-Effect Transistors Using Electrodes Modified With Self-assembled Monolayers," *Advanced Materials*, vol. 21, no. 41, pp. 4109–4114, 2009.

[61] D. Boudinet, M. Benwadih, Y. Qi, S. Altazin, J.-M. Verilhac, M. Kroger, C. Serbutoviez, R. Gwoziecki, R. Coppard, G. Le Blevennec, A. Kahn, and G. Horowitz, "Modification of

gold source and drain electrodes by self-assembled monolayer in staggered n- and p-channel organic thin film transistors," *Organic Electronics*, vol. 11, no. 2, pp. 227–237, 2010.

[62] Q. Cao and J. A. Rogers, "Ultrathin Films of Single-Walled Carbon Nanotubes for Electronics and Sensors: A Review of Fundamental and Applied Aspects," *Advanced Materials*, vol. 21, no. 1, pp. 29–53, 2009.

[63] R. H. Baughman, A. A. Zakhidov, and W. A. de Heer, "Carbon Nanotubes--the Route Toward Applications," *Science*, vol. 297, no. 5582, pp. 787–792, 2002.

[64] S. Hwang, J. Moon, S. Lee, D.-H. Kim, D. Lee, W. Choi, and M. Jeon, "Carbon nanotubes as counter electrode for dye-sensitised solar cells," *Electronics Letters*, vol. 43, no. 25, pp. 1455–1456, 2007.

[65] S. Kim, J. Yim, X. Wang, D. D. C. Bradley, S. Lee, and J. C. deMello, "Spin- and Spray-Deposited Single-Walled Carbon-Nanotube Electrodes for Organic Solar Cells," *Advanced Functional Materials*, vol. 20, no. 14, pp. 2310–2316, 2010.

[66] J. G. Nam, Y. J. Park, B. S. Kim, and J. S. Lee, "Enhancement of the efficiency of dye-sensitized solar cell by utilizing carbon nanotube counter electrode," *Scripta Materialia*, vol. 62, no. 3, pp. 148–150, 2010.

[67] M. W. Rowell, M. A. Topinka, M. D. McGehee, H.-J. Prall, G. Dennler, N. S. Sariciftci, L. Hu, and G. Gruner, "Organic solar cells with carbon nanotube network electrodes," *Applied Physics Letters*, vol. 88, no. 23, p. 233506, 2006.

[68] M. Bansal, R. Srivastava, C. Lal, M. N. Kamalasanan, and L. S. Tanwar, "Carbon nanotube-based organic light emitting diodes.," *Nanoscale*, vol. 1, no. 3, pp. 317–330, 2009.

[69] L. Hu, J. Li, J. Liu, G. Grüner, and T. Marks, "Flexible organic light-emitting diodes with transparent carbon nanotube electrodes: problems and solutions.," *Nanotechnology*, vol. 21, no. 15, p. 155202, 2010.

[70] C. M. Aguirre, C. Ternon, M. Paillet, P. Desjardins, and R. Martel, "Carbon Nanotubes as Injection Electrodes for Organic Thin Film Transistors," *Nano Letters*, vol. 9, no. 4, pp. 1457–1461, 2009.

[71] S. Liu, Z. Wei, Y. Cao, L. Gan, Z. Wang, W. Xu, X. Guo, and D. Zhu, "Ultrasensitive water-processed monolayer photodetectors," *Chemical Science*, vol. 2, no. 4, pp. 796–802, 2011.

[72] P. Avouris, Z. Chen, and V. Perebeinos, "Carbon-based electronics," *Nature Nanotechnology*, vol. 2, no. 10, pp. 605–615, 2007.

[73] H. Dai, "Carbon Nanotubes: Synthesis, Integration, and Properties," *Account of Chemical Research*, vol. 35, no. 12, pp. 1035–1044, 2002.

[74] P. Avouris, J. Appenzeller, R. Martel, and S. J. Wind, "Carbon nanotube electronics," *Proceedings of the IEEE*, vol. 91, no. 11, pp. 1772– 1784, 2003.

[75] M. Miao, "Electrical conductivity of pure carbon nanotube yarns," *Carbon*, vol. 49, no. 12, pp. 3755–3761, 2011.

[76] E. Pop, D. Mann, Q. Wang, K. Goodson, and H. Dai, "Thermal Conductance of an Individual Single-Wall Carbon Nanotube above Room Temperature," *Nano Letters*, vol. 6, no. 1, pp. 96–100, 2006.

[77] R. Stephan, "Carbon nanotubes: Exceptional mechanical and electronic properties," *Annales de Chimie Science des Matériaux*, vol. 25, no. 7, pp. 529–532, 2000.

[78] A. J. Miller, R. A. Hatton, and S. R. P. Silva, "Interpenetrating multiwall carbon nanotube electrodes for organic solar cells," *Applied Physics Letters*, vol. 89, no. 13, p. 133117, 2006.

[79] C. M. Aguirre, S. Auvray, S. Pigeon, R. Izquierdo, P. Desjardins, and R. Martel, "Carbon nanotube sheets as electrodes in organic light-emitting diodes," *Applied Physics Letters*, vol. 88, no. 18, p. 183104, 2006.

[80] X. Guo, J. P. Small, J. E. Klare, Y. Wang, M. S. Purewal, I. W. Tam, B. H. Hong, R. Caldwell, L. Huang, S. O'Brien, J. Yan, R. Breslow, S. J. Wind, J. Hone, P. Kim, and C. Nuckolls, "Covalently Bridging Gaps in Single-Walled Carbon Nanotubes with Conducting Molecules," *Science*, vol. 311, no. 5759, pp. 356 –359, 2006.

[81] K. Tsukagoshi, I. Yagi, and Y. Aoyagi, "Pentacene nanotransistor with carbon nanotube electrodes," *Applied Physics Letters*, vol. 85, no. 6, p. 1021, 2004.

[82] P. G. Collins, M. Hersam, M. Arnold, R. Martel, and P. Avouris, "Current saturation and electrical breakdown in multiwalled carbon nanotubes," *Physical Review Letters*, vol. 86, no. 14, pp. 3128–3131, 2001.

[83] P. Qi, A. Javey, M. Rolandi, Q. Wang, E. Yenilmez, and H. Dai, "Miniature Organic Transistors with Carbon Nanotubes as Quasi-One-Dimensional Electrodes," *Journal of the American Chemical Society*, vol. 126, no. 38, pp. 11774–11775, 2004.

[84] Q. Cao, Z.-T. Zhu, M. G. Lemaitre, M.-G. Xia, M. Shim, and J. A. Rogers, "Transparent flexible organic thin-film transistors that use printed single-walled carbon nanotube electrodes," *Applied Physics Letters*, vol. 88, no. 11, p. 113511, 2006.

[85] C.-H. Chang, C.-H. Chien, and J.-Y. Yang, "Pentacene-based thin-film transistors with multiwalled carbon nanotube source and drain electrodes," *Applied Physics Letters*, vol. 91, no. 8, p. 083502, 2007.

[86] B. Liu, M. A. McCarthy, Y. Yoon, D. Y. Kim, Z. Wu, F. So, P. H. Holloway, J. R. Reynolds, J. Guo, and A. G. Rinzler, "Carbon-Nanotube-Enabled Vertical Field Effect and Light-Emitting Transistors," *Advanced Materials*, vol. 20, no. 19, pp. 3605–3609, 2008.

[87] A. Southard, V. Sangwan, J. Cheng, E. D. Williams, and M. S. Fuhrer, "Solution-processed single walled carbon nanotube electrodes for organic thin-film transistors," *Organic Electronics*, vol. 10, no. 8, pp. 1556–1561, 2009.

[88] M. A. McCarthy, B. Liu, and A. G. Rinzler, "High Current, Low Voltage Carbon Nanotube Enabled Vertical Organic Field Effect Transistors," *Nano Letters*, vol. 10, no. 9, pp. 3467–3472, 2010.

[89] M. A. McCarthy, B. Liu, R. Jayaraman, S. M. Gilbert, D. Y. Kim, F. So, and A. G. Rinzler, "Reorientation of the High Mobility Plane in Pentacene-Based Carbon Nanotube Enabled Vertical Field Effect Transistors," *ACS Nano*, vol. 5, no. 1, pp. 291–298, 2010.

[90] B. Liu, M. A. McCarthy, and A. G. Rinzler, “Non-Volatile Organic Memory Elements Based on Carbon-Nanotube-Enabled Vertical Field-Effect Transistors,” *Advanced Functional Materials*, vol. 20, no. 20, pp. 3440–3445, 2010.

[91] M. A. McCarthy, B. Liu, E. P. Donoghue, I. Kravchenko, D. Y. Kim, F. So, and A. G. Rinzler, “Low-Voltage, Low-Power, Organic Light-Emitting Transistors for Active Matrix Displays,” *Science*, vol. 332, no. 6029, pp. 570 –573, 2011.

[92] M. C. Gwinner, F. Jakubka, F. Gannott, H. Sirringhaus, and J. Zaumseil, “Enhanced Ambipolar Charge Injection with Semiconducting Polymer/Carbon Nanotube Thin Films for Light-Emitting Transistors,” *ACS Nano*, vol. 6, no. 1, pp. 539–548, 2011.

[93] F. Cicoira, C. M. Aguirre, and R. Martel, “Making Contacts to n-Type Organic Transistors Using Carbon Nanotube Arrays,” *ACS Nano*, vol. 5, no. 1, pp. 283–290, 2011.

[94] F. Cicoira, N. Coppede, S. Iannotta, and R. Martel, “Ambipolar copper phthalocyanine transistors with carbon nanotube array electrodes,” *Applied Physics Letters*, vol. 98, no. 18, p. 183303, 2011.

[95] C. M. Aguirre, P. L. Levesque, M. Paillet, F. Lapointe, B. C. St-Antoine, P. Desjardins, and R. Martel, “The Role of the Oxygen/Water Redox Couple in Suppressing Electron Conduction in Field-Effect Transistors,” *Advanced Materials*, vol. 21, no. 30, pp. 3087–3091, 2009.

[96] B. K. Sarker and S. I. Khondaker, “High-performance short channel organic transistors using densely aligned carbon nanotube array electrodes,” *Applied Physics Letters*, vol. 100, no. 2, p. 023301–4, 2012.

[97] P. Avouris and R. Martel, “Progress in Carbon Nanotube Electronics and Photonics,” *MRS Bulletin*, vol. 35, no. 4, pp. 306–313, 2010.

[98] S. Heinze, J. Tersoff, R. Martel, V. Derycke, J. Appenzeller, and P. Avouris, “Carbon Nanotubes as Schottky Barrier Transistors,” *Physical Review Letters*, vol. 89, no. 10, p. 106801, 2002.

[99] A. W. Tsen, F. Cicoira, G. G. Malliaras, and J. Park, “Photoelectrical imaging and characterization of point contacts in pentacene thin-film transistors,” *Applied Physics Letters*, vol. 97, no. 2, p. 023308, 2010.

[100] Z. Liu, M. Kobayashi, B. C. Paul, Z. Bao, and Y. Nishi, “Contact engineering for organic semiconductor devices via Fermi level depinning at the metal-organic interface,” *Physical Review B*, vol. 82, no. 3, p. 035311, 2010.

[101] S. Günes, H. Neugebauer, and N. S. Sariciftci, “Conjugated Polymer-Based Organic Solar Cells,” *Chemical Reviews*, vol. 107, no. 4, pp. 1324–1338, 2007.

[102] E. J. Meijer, C. Detcheverry, P. J. Baesjou, E. van Veenendaal, D. M. de Leeuw, and T. M. Klapwijk, “Dopant density determination in disordered organic field-effect transistors,” *Journal of Applied Physics*, vol. 93, no. 8, p. 4831, 2003.

[103] Z. Wu, Z. Chen, X. Du, J. M. Logan, J. Sippel, M. Nikolou, K. Kamaras, J. R. Reynolds, D. B. Tanner, A. F. Hebard, and A. G. Rinzler, “Transparent, Conductive Carbon Nanotube Films,” *Science*, vol. 305, no. 5688, pp. 1273–1276, 2004.

[104] Y. Homma, “Mechanism of bright selective imaging of single-walled carbon nanotubes on insulators by scanning electron microscopy,” *Applied Physics Letters*, vol. 84, no. 10, p. 1750, 2004.

[105] Lee J-O., Park C., Kim J-J., Kim J., Park J.W., and Yoo K-H., “Formation of low-resistance ohmic contacts between carbon nanotube and metal electrodes by a rapid thermal annealing method,” *Journal of Physics D: Applied Physics*, vol. 33, no. 16, pp. 1953–1956, 2000.

[106] J.-T. Luo, W.-F. Wu, H.-C. Wen, B.-Z. Wan, Y.-M. Chang, C.-P. Chou, J.-M. Chen, and W.-N. Chen, “The roles of hydrophobic group on the surface of ultra low dielectric constant porous silica film during thermal treatment,” *Thin Solid Films*, vol. 515, no. 18, pp. 7275–7280, 2007.

[107] A. Salleo, M. L. Chabinyc, M. S. Yang, and R. A. Street, “Polymer thin-film transistors with chemically modified dielectric interfaces,” *Applied Physics Letters*, vol. 81, no. 23, pp. 4383–4385, 2002.

[108] M. McDowell, I. G. Hill, J. E. McDermott, S. L. Bernasek, and J. Schwartz, “Improved organic thin-film transistor performance using novel self-assembled monolayers,” *Applied Physics Letters*, vol. 88, no. 7, p. 073505, 2006.

[109] S. Kobayashi, T. Nishikawa, T. Takenobu, S. Mori, T. Shimoda, T. Mitani, H. Shimotani, N. Yoshimoto, S. Ogawa, and Y. Iwasa, “Control of carrier density by self-assembled monolayers in organic field-effect transistors,” *Nature Materials*, vol. 3, no. 5, pp. 317–322, 2004.

[110] H. Tavana and A. W. Neumann, “Recent progress in the determination of solid surface tensions from contact angles,” *Advances in Colloid and Interface Science*, vol. 132, no. 1, pp. 1–32, 2007.

[111] P. Milani and S. Iannotta, *Cluster beam synthesis of nanostructured materials*. Springer, 1999.

[112] N. Coppedè, M. Castriota, E. Cazzanelli, S. Forti, G. Tarabella, T. Toccoli, K. Walzer, and S. Iannotta, “Controlled Polymorphism in Titanyl Phthalocyanine on Mica by Hyperthermal Beams: A Micro-Raman Analysis,” *Journal of Physical Chemistry C*, vol. 114, no. 15, pp. 7038–7044, 2010.

[113] S. Iannotta and T. Toccoli, “Supersonic molecular beam growth of thin films of organic materials: A novel approach to controlling the structure, morphology, and functional properties,” *Journal of Polymer Science Part B: Polymer Physics*, vol. 41, no. 21, pp. 2501–2521, 2003.

[114] K. Walzer, T. Toccoli, A. Pallaoro, S. Iannotta, C. Wagner, T. Fritz, and K. Leo, “Comparison of organic thin films deposited by supersonic molecular-beam epitaxy and organic molecular-beam epitaxy: The case of titanyl phthalocyanine,” *Surface Science*, vol. 600, no. 10, pp. 2064–2069, 2006.

[115] J. Rivnay, R. Steyrleuthner, L. H. Jimison, A. Casadei, Z. Chen, M. F. Toney, A. Facchetti, D. Neher, and A. Salleo, “Drastic Control of Texture in a High Performance n-Type Polymeric Semiconductor and Implications for Charge Transport,” *Macromolecules*, vol. 44, no. 13, pp. 5246–5255, 2011.

[116] J. G. Labram, E. B. Domingo, N. Stingelin, D. D. C. Bradley, and T. D. Anthopoulos, "In-Situ Monitoring of the Solid-State Microstructure Evolution of Polymer:Fullerene Blend Films Using Field-Effect Transistors," *Advanced Functional Materials*, vol. 21, no. 2, pp. 356–363, 2011.

[117] Z. Bao, A. J. Lovinger, and A. Dodabalapur, "Organic field-effect transistors with high mobility based on copper phthalocyanine," *Applied Physics Letters*, vol. 69, no. 20, p. 3066, 1996.

[118] R. Zeis, T. Siegrist, and C. Kloc, "Single-crystal field-effect transistors based on copper phthalocyanine," *Applied Physics Letters*, vol. 86, no. 2, p. 022103, 2005.

[119] S. Suzuki, Y. Watanabe, Y. Homma, S. Fukuba, S. Heun, and A. Locatelli, "Work functions of individual single-walled carbon nanotubes," *Applied Physics Letters*, vol. 85, no. 1, pp. 127–129, 2004.

[120] W. Osikowicz, M. P. de Jong, S. Braun, C. Tengstedt, M. Fahlman, and W. R. Salaneck, "Energetics at Au top and bottom contacts on conjugated polymers," *Applied Physics Letters*, vol. 88, no. 19, p. 193504–3, 2006.

[121] A. Salleo, "Charge transport in polymeric transistors," *Materials Today*, vol. 10, no. 3, pp. 38–45, 2007.

[122] M. Shtein, J. Mapel, J. B. Benziger, and S. R. Forrest, "Effects of film morphology and gate dielectric surface preparation on the electrical characteristics of organic-vapor-phase-deposited pentacene thin-film transistors," *Applied Physics Letters*, vol. 81, no. 2, pp. 268–270, 2002.

[123] S. Cho, J. Yuen, J. Y. Kim, K. Lee, and A. J. Heeger, "Ambipolar organic field-effect transistors fabricated using a composite of semiconducting polymer and soluble fullerene," *Applied Physics Letters*, vol. 89, no. 15, p. 153505, 2006.

[124] A. Babel, J. D. Wind, and S. A. Jenekhe, "Ambipolar charge transport in air-stable polymer blend thin-film transistors," *Advanced Functional Materials*, vol. 14, no. 9, pp. 891–898, 2004.

[125] S. H. Yang, M. Y. Cho, S. G. Jo, J. S. Jung, K. H. Jung, S. Y. Bae, D. H. Choi, S. Kim, and J. Joo, "Photoresponsive ambipolar transport characteristics of organic thin film transistors using soluble HB-ant-THT and PCBM composites," *Synthetic Metals*, vol. 162, no. 3–4, pp. 332–336, 2012.

[126] Y. Hayashi, H. Kanamori, I. Yamada, A. Takasu, S. Takagi, and K. Kaneko, "Facile fabrication method for p/n-type and ambipolar transport polyphenylenevinylene-based thin-film field-effect transistors by blending C60 fullerene," *Applied Physics Letters*, vol. 86, no. 5, p. 052104, 2005.

[127] M. Reyes-Reyes, K. Kim, and D. L. Carroll, "High-efficiency photovoltaic devices based on annealed poly(3-hexylthiophene) and 1-(3-methoxycarbonyl)-propyl-1- phenyl-(6,6)C[sub 61] blends," *Applied Physics Letters*, vol. 87, no. 8, pp. 083506–3, 2005.

[128] L. Chen, Z. Hong, G. Li, and Y. Yang, "Recent Progress in Polymer Solar Cells: Manipulation of Polymer:Fullerene Morphology and the Formation of Efficient Inverted Polymer Solar Cells," *Advanced Materials*, vol. 21, no. 14-15, pp. 1434–1449, 2009.

APPENDICES

APPENDIX 1 CHARACTERIZATION of P3HT-TFTs (1st PROCEDURE)

In the 1st procedure, chlorobenzene (Sigma Aldrich) was the solvent and no annealing was carried out after film deposition (5 mg/mL). P3HT from Rieke metals company, with M_w of about 50 kg/mol was used. P3HT Films were deposited on 100 nm-thick SiO_2 doped Si substrate The output characteristics of SWCNT P3HT TFTs and Au P3HT TFTs (Figure_A 1.1) showed a typical p-type semiconducting behavior. At V_D= -1 V, and V_G= -40 V, I_D was ~ -0.35×10^{-7} A in SWCNT P3HT TFTs and I_D was ~ -0.28×10^{-7} A in Au P3HT TFTs consequently we can say that the injection efficiency of SWCNT P3HT TFTs is almost the same as that of Au P3HT TFTs.

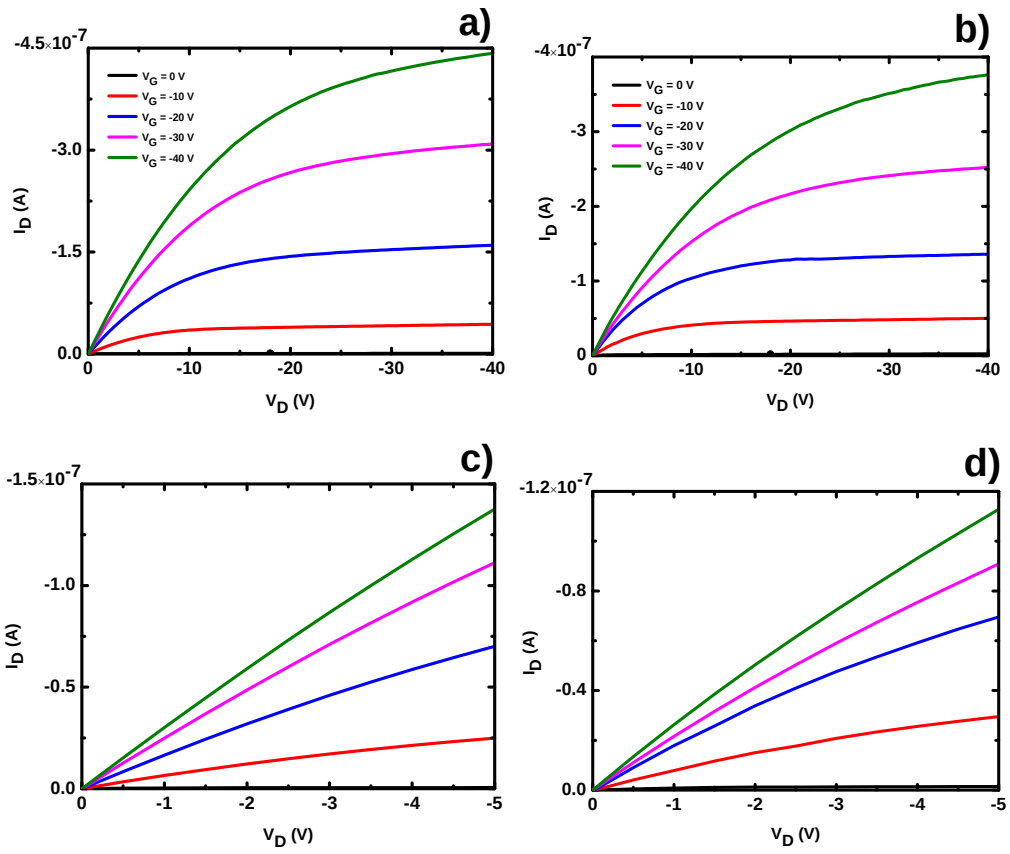

Figure_A 1.1: Output characteristics of: SWCNT P3HT TFTs a) and Au P3HT TFTs b). Output characteristics of: SWCNT P3HT TFTs c) and Au P3HT TFTs d) for 0 V ≤ V_D ≤ -5 V. V_D changes by 500 mV steps (W/L = 2000 µm/10 µm, 100 nm thick SiO_2).

I_{ON}/I_{OFF} values of about 10^4 and 10^5 were found for Au P3HT TFTs and SWCNT P3HT TFTs, respectively using transfer curves at saturation regime (Figure_A 1.2).

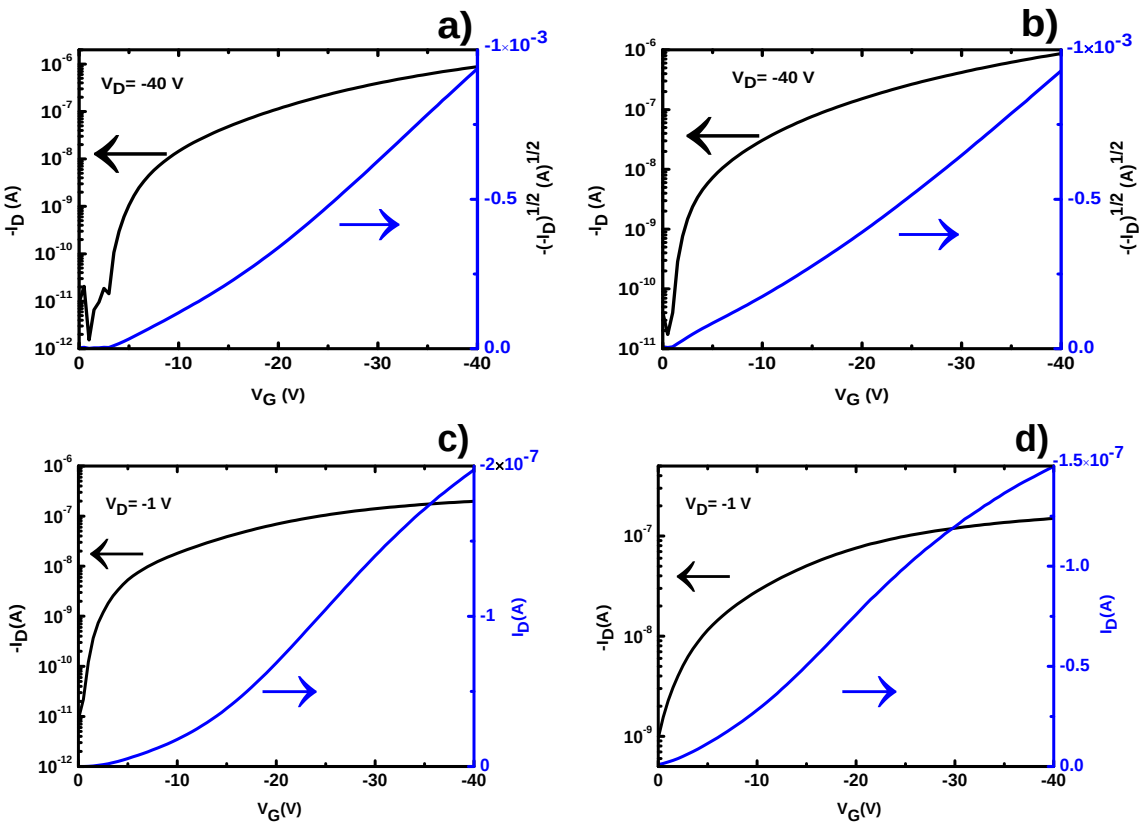

Figure_A 1.2: Transfer characteristics of: SWCNT P3HT TFTs a) and Au P3HT TFTs b) at V_D = -40 V. Transfer characteristics of: SWCNT P3HT TFTs c) and Au P3HT TFTs d) at V_D = -1 V. V_G changes by 500 mV steps (W/L = 2000 µm/10 µm, 100 nm thick SiO_2).

The hole mobility in saturation (V_D = -40 V) and linear (V_D = -1 V) regimes and threshold voltage were calculated from the transfer curves. The average value of μ_h in saturation regime was calculated 3.4×10^{-4} $cm^2/V\cdot s$ and V_{TH} was calculated -11.5 V for SWCNT P3HT TFTs and μ_h in saturation regime was 2.4×10^{-4} $cm^2/V\cdot s$ and V_{TH} was -8 V for Au P3HT TFTs.

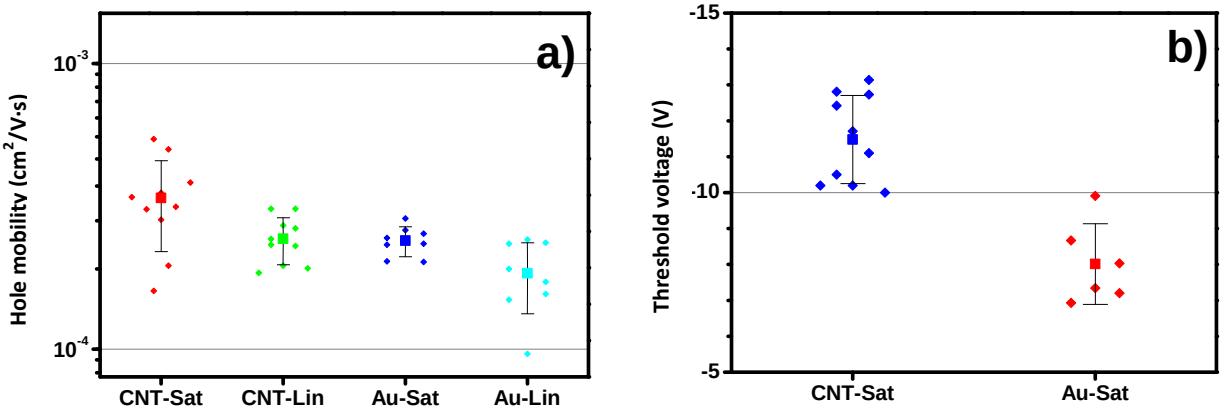

Figure_A 1.3: Hole mobility a) extracted in the saturation (V_D = -40 V) and linear (V_D = -1 V) regimes, and threshold voltage b) extracted in the saturation regime (V_D = -40 V) of SWCNT P3HT TFTs and Au P3HT TFTs. Error bars denote the standard deviation. W= 1000 µm, 2000 µm, L = 40, 20, 30, 15, and 10 µm.

The average SS of 0.8 V/decade for Au P3HT TFTs and 1.08 V/decade for SWCNT P3HT TFTs were calculated.

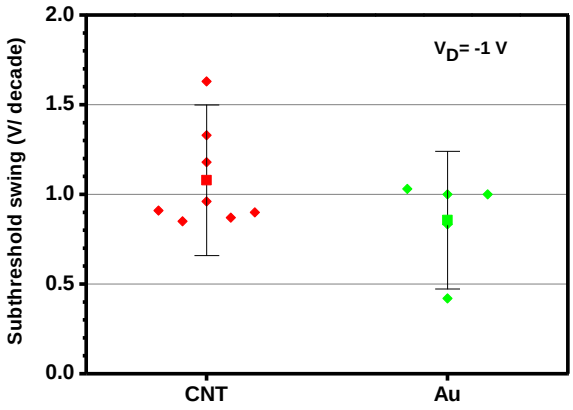

Figure_A 1.4: Subthreshold swing at V_D= -1 V for SWCNT P3HT TFTs and Au P3HT TFTs. The bars correspond to the standard deviation. W= 1000 µm, 2000 µm, L = 40, 20, 30, 15, 10 µm.

APPENDIX 2 CHARACTERIZATION of P3HT-TFTs (2nd PROCEDURE)

In 2nd procedure, P3HT (Rieke Metals company, M_w ~ 50 kg/ mol) solutions (3 mg/mL) in chloroform (Sigma Aldrich) were spin coated onto the cleaned Au and SWCNT electrodes samples at 1000 rpm, followed by annealing at 100 °C in glove box for 1 hour [27]. Films were deposited on 200 nm-thick SiO_2 doped Si substrate. Four samples were fabricated. Two out of these four samples (one with Au and another one with SWCNT electrodes) were treated with hexamethyldisilazane (HMDS), followed by annealing at 100 ˚C in the glove box.

Among 16 measured devices for each sample, 11, 13, 10, and 8 devices exhibited transistor behavior in SWCNT P3HT TFTs, Au P3HT TFTs, Au HMDS P3HT TFTs, and SWCNT HMDS P3HT TFTs, respectively.

At low V_D, SWCNT P3HT TFTs showed quasi linear I_D-V_D characteristics. However, a sublinear behavior was observed for Au P3HT TFTs (Figure_A 2.1). This indicates the presence of a barrier for hole injection from Au electrodes to P3HT. Moreover, the injection efficiency of SWCNT P3HT TFTs at V_D= -1 V and V_G= -60 V is about six times higher than that of Au P3HT TFTs.

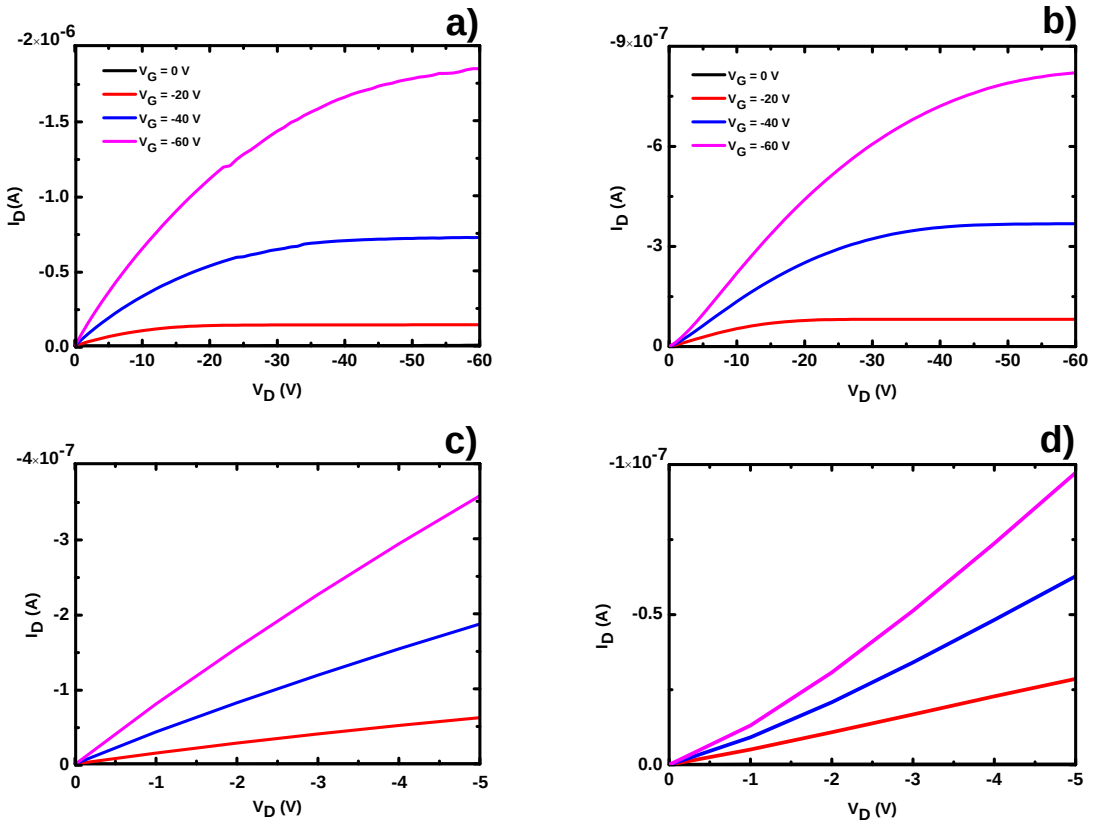

Figure_A 2.1: Output characteristics of: SWCNT P3HT TFTs a) and Au P3HT TFTs b). Output characteristics of: SWCNT P3HT TFTs c) and Au P3HT TFTs d) for 0 V ≤ V_D ≤ -5 V. V_D changes by 500 mV steps (W/L = 1510 µm/20 µm, 200 nm thick SiO_2).

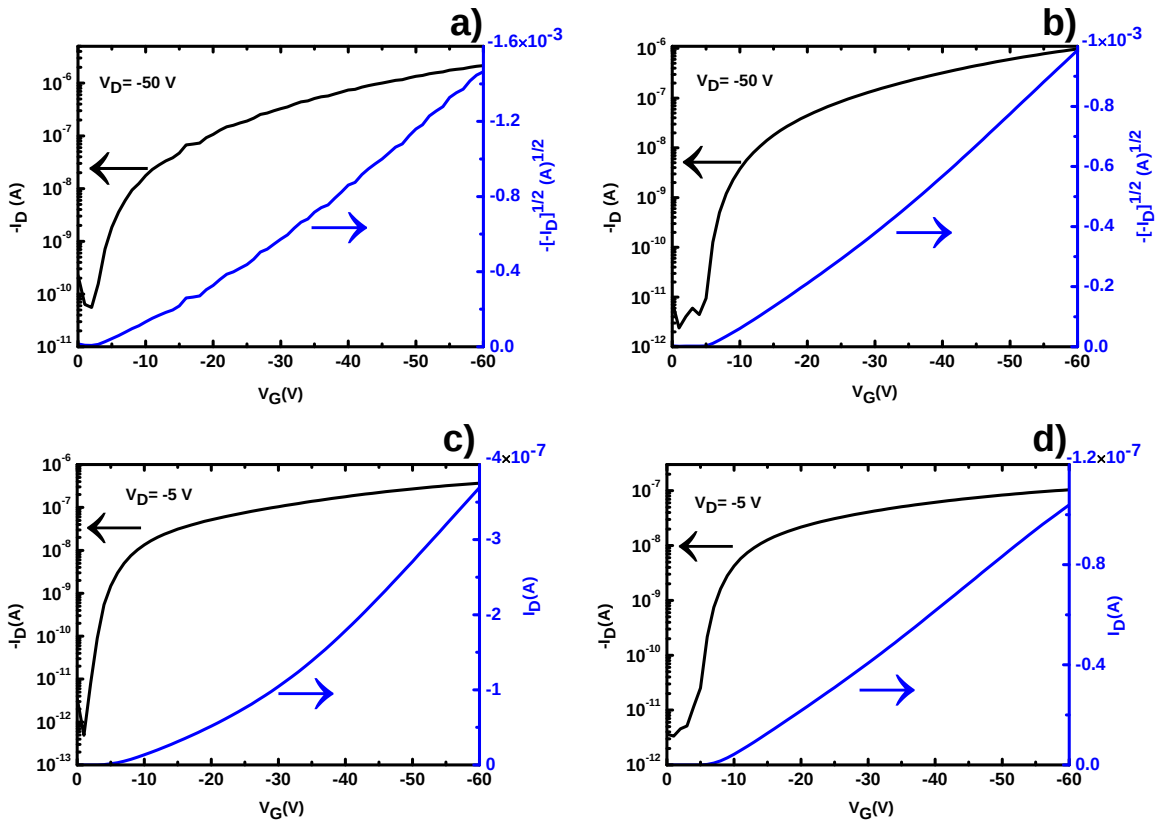

Figure_A 2.2: Transfer characteristics of: SWCNT P3HT TFTs a) and Au P3HT TFTs b) at V_D = -50 V. Transfer characteristics of: SWCNT P3HT TFTs c) and Au P3HT TFTs d) at V_D = -5. V_G changes by 500 mV steps (W/L = 1510 µm/20 µm, 200 nm thick SiO_2).

A quasi linear output characteristic is also observed with SWCNT HMDS P3HT TFTs (Figure_A 2.3). The better injection performance of the SWCNT electrodes is emphasized by the low-voltage characteristics. The injection efficiency of SWCNT HMDS P3HT TFTs at V_D= -1 V and V_G= -60 V is one order of magnitude higher than that of Au HMDS P3HT TFTs.

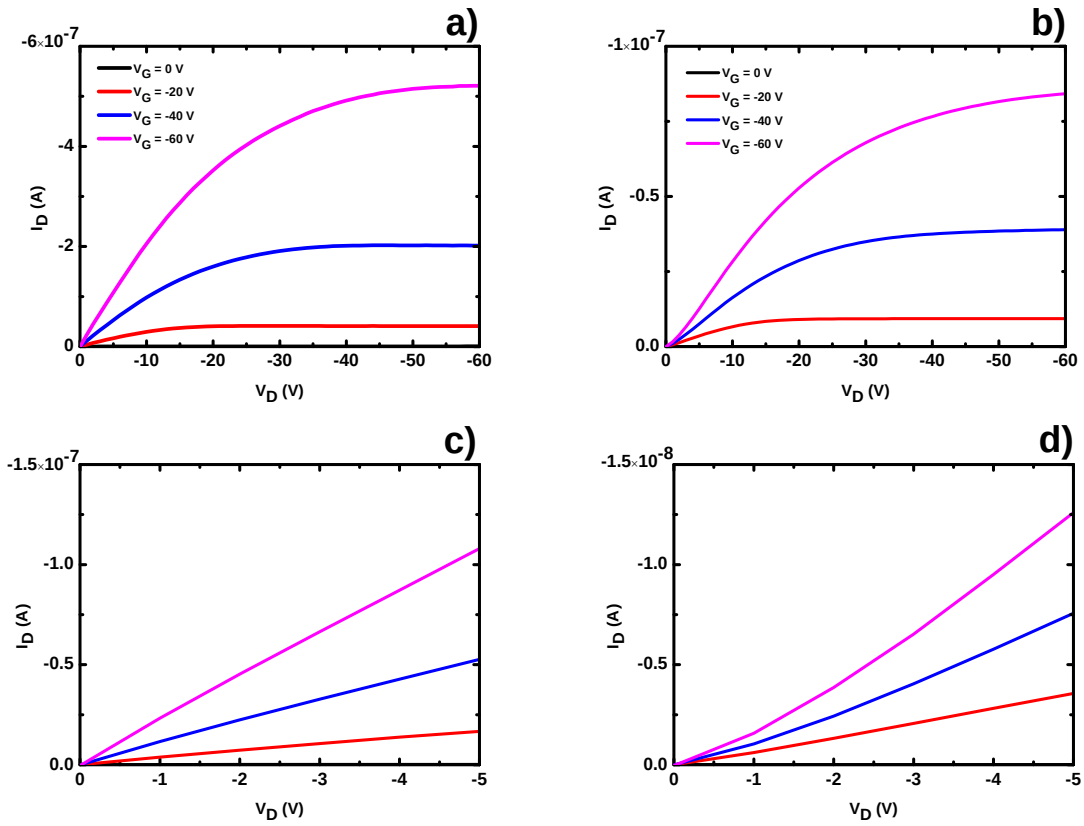

Figure_A 2.3: Output characteristics of: SWCNT HMDS P3HT TFTs a) and Au HMDS P3HT TFTs b). Output characteristics of: SWCNT HMDS P3HT TFTs c) and Au HMDS P3HT TFTs d) for 0 V ≤ V_D ≤ -5 V. V_D changes by 500 mV steps (W/L = 1510 µm/20 µm, 200 nm thick SiO_2).

The transfer curves of SWCNT HMDS P3HT TFTs and Au HMDS P3HT TFTs are illustrated in Figure_A 2.4. I_{ON}/I_{OFF} in the range of 10^4- 10^5 was observed for all devices.

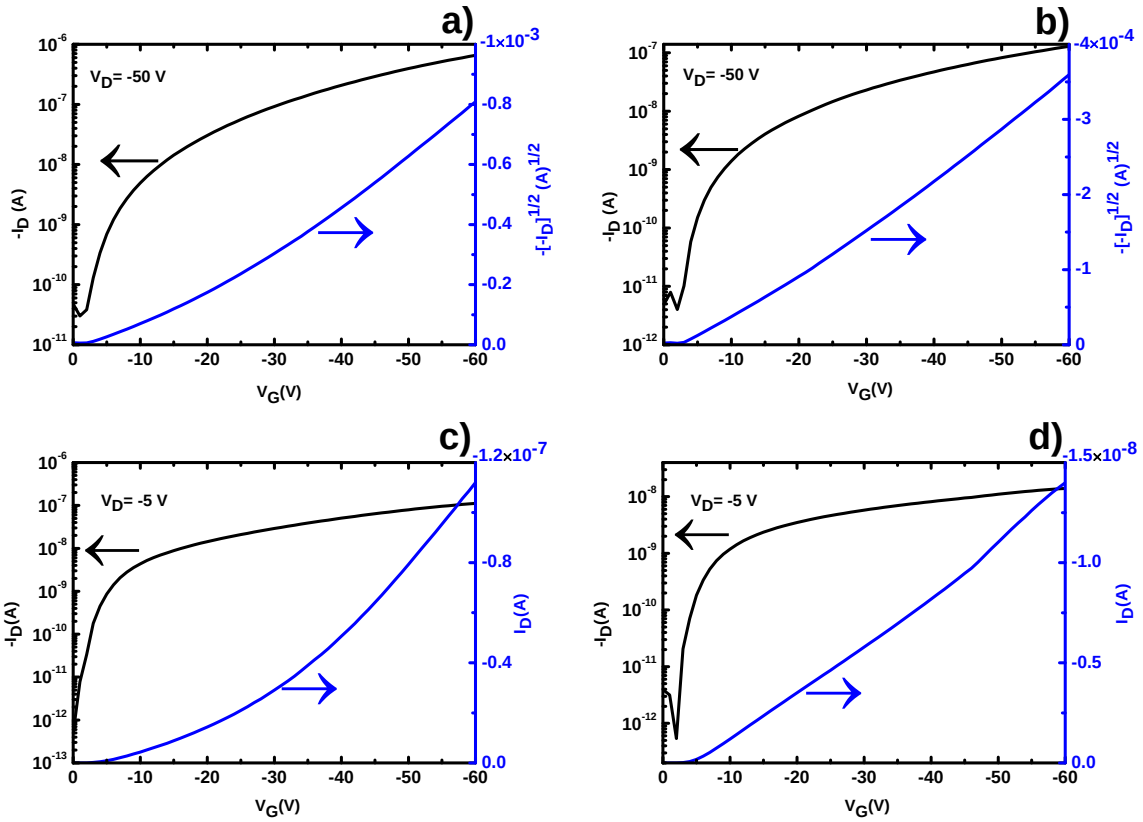

Figure_A 2.4: Transfer characteristics of: SWCNT HMDS P3HT TFTs a) and Au HMDS P3HT TFTs b) at V_D = -50 V. Transfer characteristics of: SWCNT HMDS P3HT TFTs c) and Au HMDS P3HT TFTs d) at V_D = -5 V. V_G changes by 500 mV steps (W/L = 1510 µm/20 µm, 200 nm thick SiO_2).

As shown in Figure_A 2.5, higher average value of μ_h was observed for SWCNT P3HT TFTs (SWCNT HMDS P3HT TFTs) in comparison with Au P3HT TFTs (Au HMDS P3HT TFTs) in saturation and linear regime. It should be noted that the differences in mobility are more pronounced in linear regime than in saturation regime (V_D= -50 V: μ_h= 1.3×10^{-3} $cm^2/V\cdot s$ for SWCNT P3HT TFTs and μ_h= 7.3×10^{-4} $cm^2/V\cdot s$ for Au P3HT TFTs; V_D= -5 V: μ_h= 1.1×10^{-3} $cm^2/V\cdot s$ for SWCNT P3HT TFTs and μ_h= 2.3×10^{-4} $cm^2/V\cdot s$ for Au P3HT TFTs).

V_{TH} for Au HMDS P3HT TFTs (V_{TH}= -10 V) is lower compared to Au P3HT TFTs (V_{TH}= -15 V). However this effect is not observed with SWCNT electrodes i.e. V_{TH} for SWCNT HMDS P3HT (V_{TH}= -16 V) TFTs is higher than that in SWCNT P3HT TFTs (V_{TH}= -14.6 V).

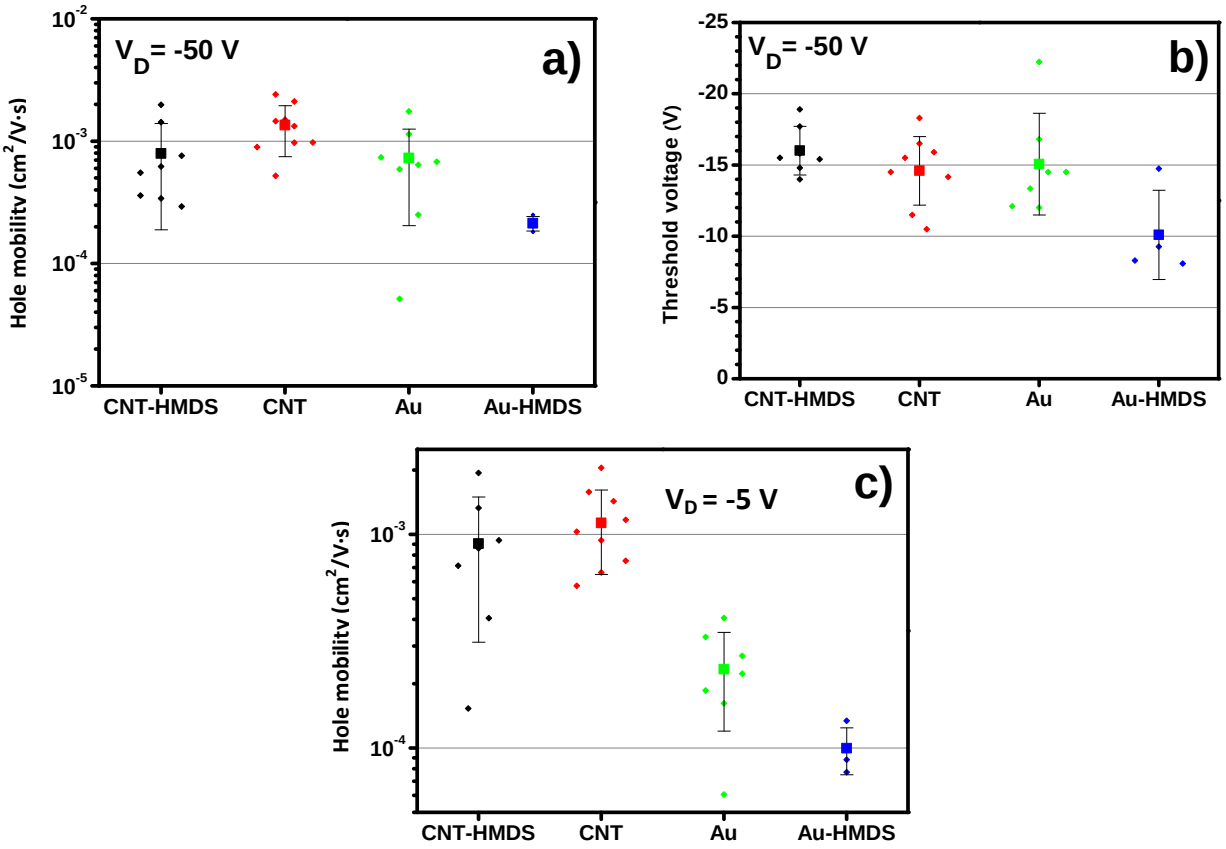

Figure_A 2.5: Hole mobility a), threshold voltage b) extracted in the saturation regime (V_D = -50 V) and hole mobility (c) extracted in the linear regime (V_D = -5 V) of SWCNT P3HT TFTs, Au P3HT TFTs, SWCNT HMDS P3HT TFTs, Au HMDS P3HT TFTs. Error bars denote the standard deviation. L/W= 5/1555 µm/µm, L/W = 10/1540 µm/µm, L/W= 20/1510 µm/µm, L/W= 50/1413 µm/µm.

Average SS of about 1 V/decade for SWCNT P3HT TFTs and 1.8 V/decade for Au P3HT TFTs were calculated (Figure_A 2.6).

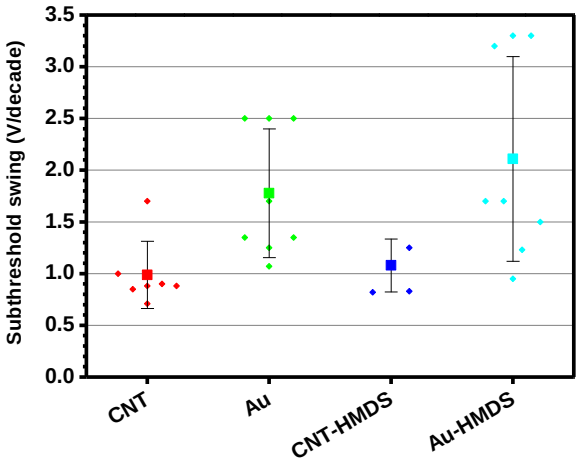

Figure_A 2.6: Subthreshold swing at V_D= -1 V for SWCNT P3HT TFTs, SWCNT HMDS TFTs, Au P3HT TFTs, and Au HMDS P3HT TFTs. The bars denote standard deviation. L/W= 5/1555 µm/µm, L/W = 10/1540 µm/µm, L/W= 20/1510 µm/µm, L/W= 50/1413 µm/µm.

We would like to mention that in this procedure, we observed, just once, ambipolarity in SWCNT P3HT TFTs (Figure_A 2.7). At present, we do not have a definitive explanation for this observation, probably related to the presence of SWCNTs within the transistor channel. The topic is under investigation.

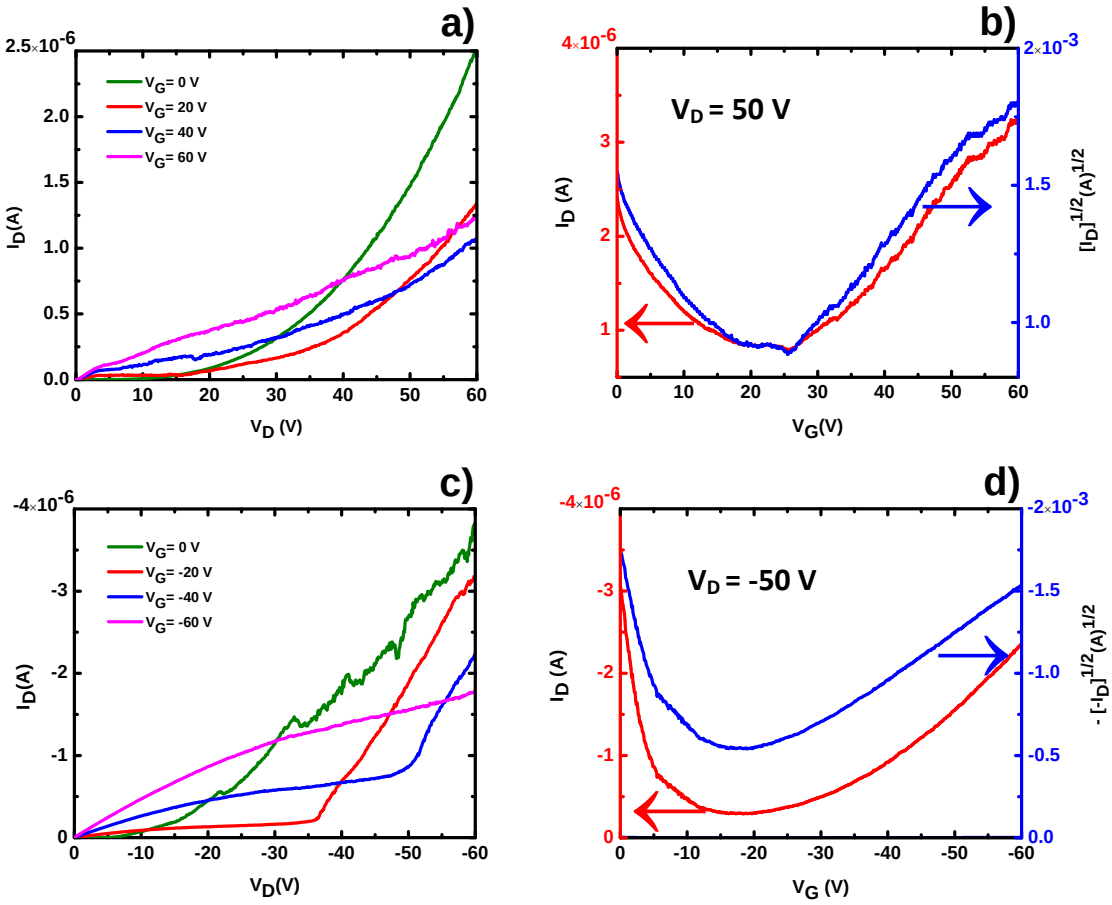

Figure_A 2.7: Output a) and transfer b) curves of SWCNT P3HT TFT for n-type behavior. Output (c) and transfer (d) curves of SWCNT P3HT TFT for p-type behavior. (W/L = 1413 µm/50 µm, 200 nm thick SiO_2).

APPENDIX 3 CHARACTERIZATION of P3HT-TFTs (3rd PROCEDURE)

In 3rd procedure, P3HT (Rieke Metals, M_w ~ 50 kg/ mol) solutions (3 mg/mL) in DCB (Sigma Aldrich) were spin coated onto the cleaned Au and SWCNT electrodes samples at 1000 rpm, followed by annealing at 100 °C for 1 hour [27]. Films were deposited on 100 nm-thick SiO_2 doped Si substrate. Figure_A 3.1 and Figure_A 3.2 show the output and transfer characteristics of SWCNT P3HT TFTs and Au P3HT TFTs, respectively.

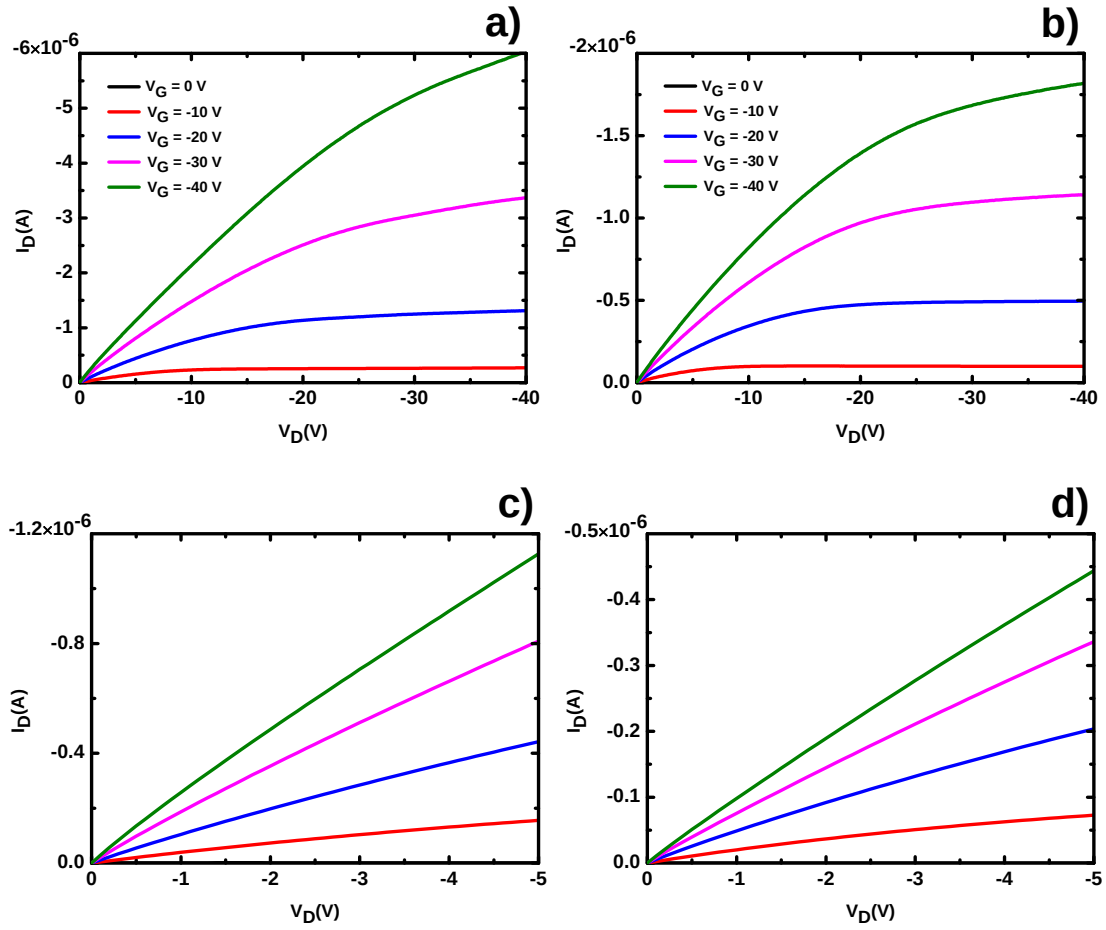

Figure_A 3.1: Output characteristics of: SWCNT P3HT TFTs a) and Au P3HT TFTs b). Output characteristics of: SWCNT P3HT TFTs c) and Au P3HT TFTs d) for 0 V ≤ V_D ≤ -5 V. V_D changes by 100 mV steps (W/L = 1555 µm/5 µm, 100 nm thick SiO_2).

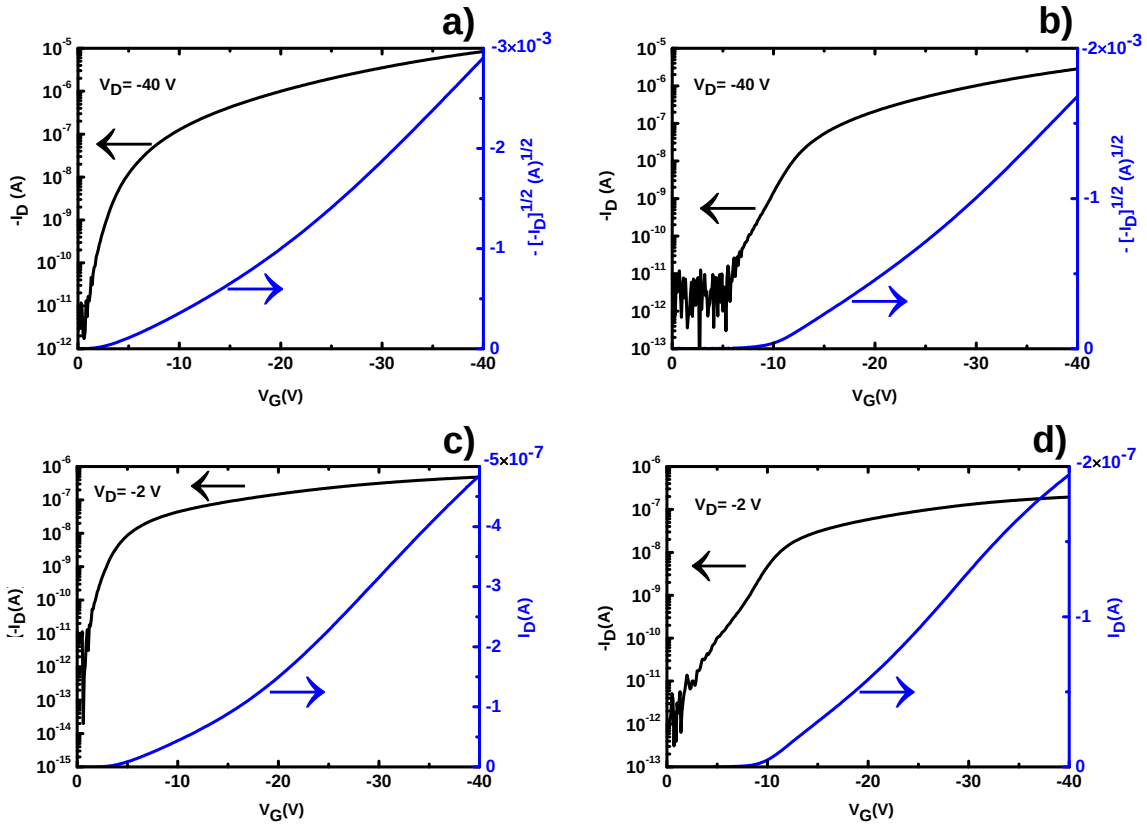

Figure_A 3.2: Transfer characteristics of: SWCNT P3HT TFTs a) and Au P3HT TFTs b) at V_D = -40 V. Transfer characteristics of: SWCNT P3HT TFTs c) and Au P3HT TFTs d) at V_D = -2 V. V_G changes by 100 mV steps (W/L = 1555 µm/ 5 µm, 100 nm thick SiO_2).

As shown in Figure_A 3.3, the average values of μ_h for SWCNT P3HT TFTs and Au P3HT TFTs in saturation and linear regimes are almost the same. The average value of V_{TH} of -11 V and -14 V were calculated in SWCNT P3HT TFTs and Au P3HT TFTs, respectively.

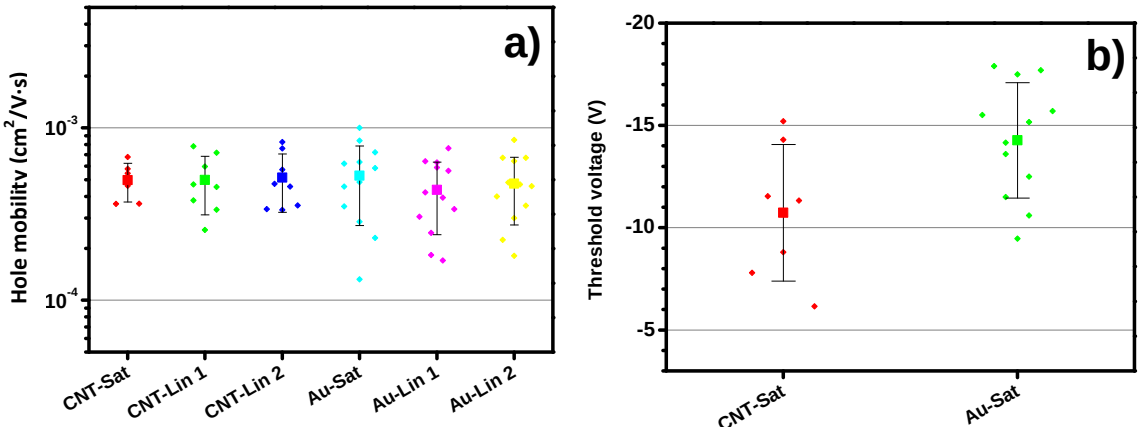

Figure_A 3.3: Hole mobility a) extracted in saturation regime (V_D= -40 V), linear regime 1 (V_D= -2 V), linear regime 2 (V_D= -5 V) and threshold voltage b) extracted in saturation regime for SWCNT P3HT TFTs and Au P3HT TFTs. The error bars denote the standard deviation. L/W= 5/1555 µm/µm, L/W = 10/1540 µm/µm, L/W= 20/1510 µm/µm, L/W= 50/1413 µm/µm.

In this procedure, we observed, just once, ambipolarity in SWCNT P3HT TFTs (Figure_A 3.4). At present we do not have a definitive explanation for this observation, probably related to the presence of SWCNTs within the transistor channel. The topic is under investigation.

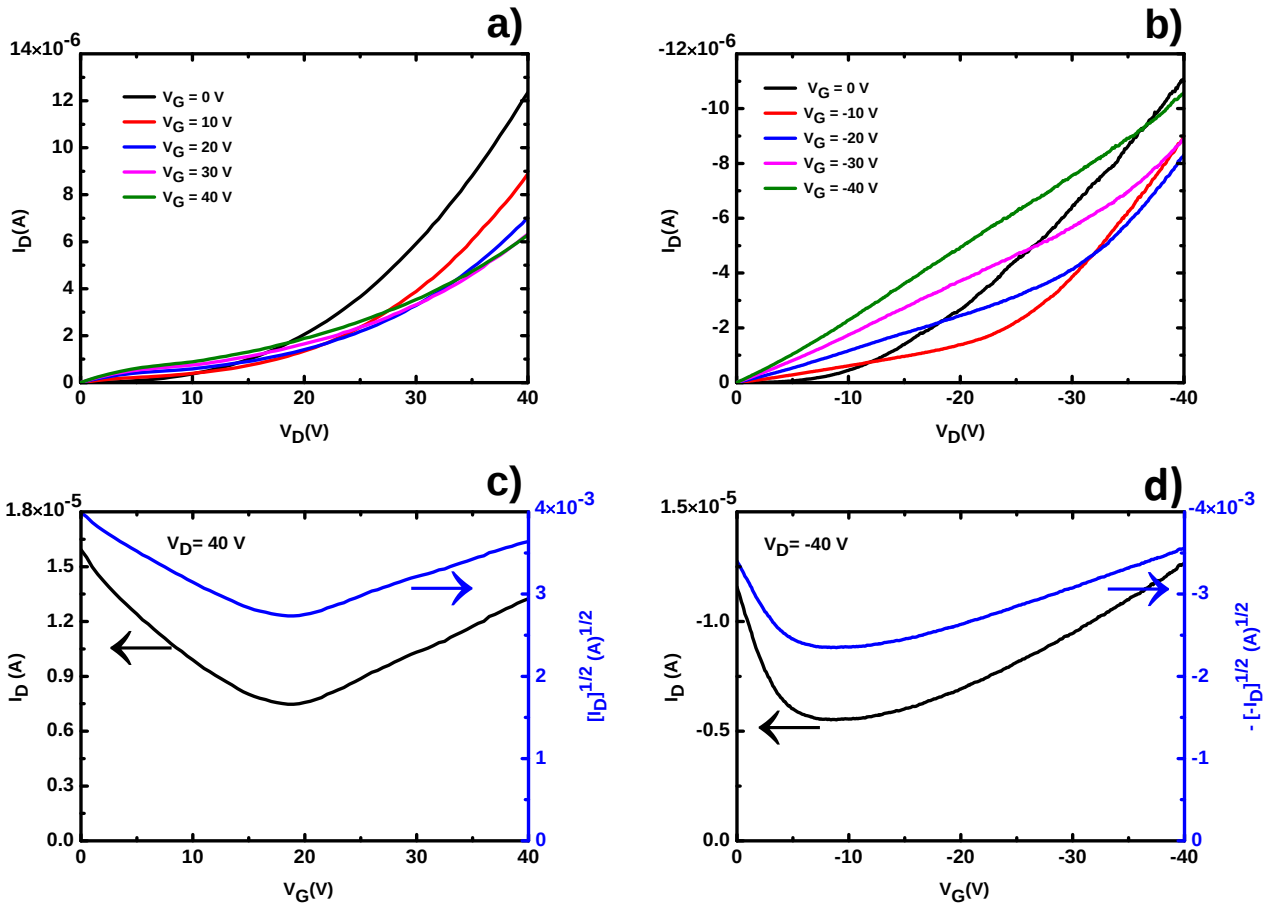

Figure_A 3.4: Output curves of SWCNT P3HT TFT for n-type a) and p-type b) behavior. Transfer curves of SWCNT P3HT TFT for n-type c) and p-type d) behavior. (W/L = 1510 µm/20 µm, 100 nm thick SiO_2).